Studies on Quarkonia Suppression and the Applicability of Hydrodynamics in Heavy-Ion Collisions

THESIS

Submitted in partial fulfilment of

the requirements for the degree of

DOCTOR OF PHILOSOPHY

by

Hatwar Nikhil Duryodhan

2017PHXF0038P

Under the supervision of

Prof. Madhukar Mishra

BITS Pilani

Pilani | Dubai | Goa | Hyderabad

BIRLA INSTITUTE OF TECHNOLOGY & SCIENCE, PILANI
2023

BIRLA INSTITUTE OF TECHNOLOGY & SCIENCE PILANI - 333 031 (RAJASTHAN) INDIA

CERTIFICATE

This is to certify that the work reported in the Ph.D. thesis entitled **"Studies on Quarkonia Suppression and the Applicability of Hydrodynamics in Heavy-Ion Collisions"**, submitted by **Hatwar Nikhil Duryodhan**, ID No. **2017PHXF0038P** at Physics Department, BITS-Pilani, Pilani Campus for the award of the degree of Doctor of Philosophy (Ph.D.), is a bonafide record of his original work carried out under my supervision. This work has not been submitted elsewhere for any other degree or diploma.

Signature: ....

Prof. Madhukar Mishra

Associate Professor,
Department of Physics,
BITS-Pilani, Pilani Campus

Date: ....

Dedicated to
Aai, Pappa and Tai

Acknowledgements

First and foremost, I am thankful to my advisor, Dr. Madhukar Mishra. He introduced me to this intriguing field of high-energy physics and also allowed me to explore a new direction on my own. I am extremely grateful to him for supporting me and patiently guiding me through problems that I encountered. I am grateful to Dr. Gabriele Inghirami of Goethe University Frankfurt for clearing my doubts and helping me run and use the relativistic viscous hydrodynamics code ECHO-QGP not once but numerous times. I would like to thank Prof. Rajeev Bhalerao of IISER Pune for taking out time and patiently answering my questions by email as well in-person during ICPAQGP 2023. I would equally like to thank Prof. Paul Romatschke of Colorado University for solving my queries about collectivity. I am also thankful to my seniors and wonderful collaborators, Dr. S. Ganesh and Dr. Captain R. Singh, for their crucial help at various times.

I thank my Doctoral Advisory Committee members, Dr. Navin Singh and Dr. Tapomoy Guha Sarkar, for their time reviewing my work. Navin Sir has diligently helped me a lot during my Ph.D. admission and qualifying exam and has also helped in various administrative matters. I immensely enjoyed learning new subjects with Tapomoy Sir. His teaching methods are brilliant, and his classes were none less than an adventure. I am grateful to him for the insightful discussions on various topics. He is one of the best teachers under whom I have ever studied. I would also like to extend my special gratitude to Dr. Jayandra Nath Bandopadhyay. He has been a constant go-to person for support or advice for other scholars of the department and me. I will miss his joyous and magnanimous company. I would also like to thank other department faculties with whom I got a chance to interact once in a while.

I am grateful to my lab members Neha, Mohit, Renu, Ranjan, Charul, and Shubham, later two of whom are also my juniors. I especially want to thank my previous lab members, Arghya Maity and Jagrity Chaudhary, with whom I had a wonderful time. I would like to thank my present and previous colleagues Aruna, Shivaraja, Rambabu, Ishanji,

Dinachandra, Roul, Deepthi, and other scholars of the physics department. I would like to mention my friends from other departments, Aishwarya Ramesh and Abheek Gupta, for always being there for me. I am indebted to Prof. Anil Rai of Humanities Department for giving me the opportunity to be a part of his team in various performances and for his music lessons.

I am sincerely thankful to the DRC convener Dr. Manjuladevi, the Head of Department, Dr. Rakesh Choubisa, and previous conveners and HODs during my time here for their help in various matters. I would also like to thank Rajeevji, and Shrikantji, for their help in various administrative matters and also while instructing the physics laboratory course. And finally, I am grateful to the Birla Institute of Technology & Science, Pilani, for providing the opportunity to pursue my doctoral studies and to the Department of Science and Technology, Government of India, for providing financial support.

Nikhil Hatwar

Abstract

Very little is known about different phases of strongly interacting matter governed by *quantum chromodynamics* (QCD). The known nuclei of elements in the periodic table at normal conditions occupy merely a point in QCD phase space. The quest now is to find what form the quark-gluon matter takes in different density and temperature conditions. Can we probe such a matter in experiments? Can we characterize a bulk, colored medium from first principles and find its properties? At large temperatures and densities, we expect first the nucleons, viz. protons and neutrons, to get free and then further ahead quarks being deconfined from nucleons. A free quark state is believed to have existed in the early universe before the formation of stable nucleons. We also expect a dense quark-gluon medium to exist inside the neutron star. Both of these systems are inaccessible to probe. However, a *quark-gluon plasma* (QGP) state could also form briefly after heavy-ion collision experiments. And this could be confirmed by systematically analyzing the difference in observed particles and their distributions in collider experiments and those from scaled-up *proton-proton* collisions where we do not expect QGP formation. Such comparison provides us with experimental signatures of such a state forming. However, this is just half the proof. What we also need is to reproduce these experimental signatures independently from the first principles, which is challenging. An overview of quark-gluon plasma and its signatures is provided in **chapter 1**.

The **first problem** presented in this thesis is bottomonium suppression in Pb-Pb collisions at CERN LHC energies whose background is covered in **chapter 2**. Suppressed Quarkonia production is a prominent signature of hot quark medium formation. A bound state of heavy quark and heavy anti-quark matter is called *quarkonia*. The idea is that while traversing the deconfined state of the quark-gluon medium, the quarkonia will dissociate and will be produced lesser in number. Experiments do observe such suppression. We first introduce the potential non-relativistic QCD (pNRQCD), which is the effective field theory for quarkonia in QGP, along with quark anti-quark bound state

potential as well as the origin of various effects which affect this bound state. We then go on to calculate these effects for the system at 2.76 TeV and 5.02 TeV energies. The background quark-gluon plasma is modeled as a (3+1)-dimensional hydrodynamic medium with Lattice QCD EoS. The effects considered are the dissociation of color singlet state on the absorption of an *ultrasoft* medium gluon into a color doublet state. The formation of the bound state will be affected by the screening of color charges in the medium and also by collisions with medium partons. Both of these effects are also considered. We also take into account the suppression effects in mediums where no QGP is expected. These are called *cold nuclear matter* effects of which nuclear shadowing is considered here. We produce a quantity equivalent to experimentally measured suppression factor called *nuclear modification factor* as a function of transverse momentum, centrality, and rapidity. The theoretical results qualitatively explain the experimentally measured suppression results. One way of characterizing QGP would be the reproduction of multiple signatures simultaneously from a single coherent formalism. This first study presented in **chapter 3** is an important step in this direction.

The **second problem**, addressed in **chapter 5** of this thesis, is about finding the smallest size of QGP in peripheral symmetric heavy-ion collision. We have convincing signatures of QGP formation in nucleus-nucleus collisions. However, over the years, with increasing energy of collisions, QGP formation in small systems viz. in *nucleus-proton* and high multiplicity *proton-proton* is also speculated. But these systems are also the systems in which cold nuclear matter plays a significant role in producing QGP-like signatures that are not due to QGP. This could be a serious problem because in *quarkonia suppression* one uses *proton-proton* collisions as reference. Hence it is important to find the smallest system size of heavy-ion collision that could be characterized as QGP. The prerequisites of this study are covered in **chapter 4**. Viscous hydrodynamics has been unreasonably effective in explaining the QGP stage in heavy-ion collision. Neither the system achieves local equilibrium nor pressure isotropization. Hence one calls it *hydrodynamization* rather than hydrodynamics, which essentially means that the second-order hydrodynamics theory is adequate to model the

QGP stage. The analytical structure of relativistic viscous hydrodynamics has a pole that does not vanish in the limit of a small wave number called the *non-hydrodynamic mode.* It turns out that this non-hydrodynamic mode is controlled by a second-order transport coefficient called *shear relaxation time.* We exploit this fact and produce the elliptic flow of the Pb-Pb and Au-Au system to find the smallest size that could hydrodynamize.

Contents

Acknowledgement **viii**

Abstract **xi**

Contents **xii**

List of Figures **xvi**

List of Tables **xxii**

List of Symbols and Acronyms **xxiv**

1 Introduction to quark-gluon plasma **2**

1.1 Quantum chromodynamics 3

1.1.1 Running coupling constant, asymptotic freedom, and quark confinement 6

1.1.2 Quark-Gluon plasma 9

1.2 Stages of high energy collision 11

1.3 Signatures of quark-gluon plasma in high energy collision 13

1.3.1 Jet quenching 13

1.3.2 Collective flow 14

1.3.3 Quarkonia suppression 15

1.3.4 Direct photons 16

1.3.5 Strangeness enhancement 17

2 Theoretical framework of quarkonia suppression **20**

2.1 Quarkonia effective theory: potential non-relativistic QCD (pNRQCD) 20

2.2 Quarkonium potential 22

2.3 Hot matter effects 23

2.3.1 Gluonic dissociation 23
2.3.2 Collisional damping 27
2.3.3 Color screening 28
2.4 Cold nuclear matter effects 30
2.4.1 Nuclear shadowing 30

3 Bottomonium suppression in Pb-Pb collisions at CERN LHC energies 34
3.1 Introduction and literature review 34
3.2 Formalism 36
3.2.1 (3+1)-dimensional hydrodynamical expansion of the medium 36
3.2.2 Suppression mechanisms 41
3.2.3 Recombination mechanisms 45
3.2.4 Final number of bottomonium 46
3.3 Results and discussions 47
3.4 Summary 51

4 Relativistic viscous hydrodynamics 52
4.1 Zeroth order hydrodynamics : Ideal fluid 52
4.2 Problem with ideal fluid dynamics 54
4.3 First order hydrodynamics : Navier-Stokes theory 55
4.4 Causality violation in Navier-Stokes equation 57
4.5 Second order hydrodynamics : Müller Israel Stewart theory 59
4.6 Hydrodynamics as a microscopic theory in the limit 60
4.6.1 Hydrodynamic and non-hydrodynamic modes 61
4.6.2 Non-hydrodynamic mode in MIS theory 63

5 Finding the onset of hydrodynamization using the non-hydrodynamic mode 68
5.1 Introduction and literature review 68
5.2 Formalism 72
5.2.1 Input parameters 78
5.2.2 Fixing centrality parameters 79
5.3 Flow results and discussion 81
5.3.1 Elliptic flow results for Au-Au and Pb-Pb collision systems . 81
5.3.2 Elliptic flow results for varying shear relaxation time 85
5.3.3 Transverse plane system evolution results 87

5.4 Summary 91

6 Concluding discussion and outlook **93**
6.1 Study on bottomonium suppression 93
6.2 Outlook 94
6.3 Study on hydrodynamic applicablity 94
6.4 Outlook 95

Appendix A - Open heavy flavor suppression in Pb-Pb collision at $\sqrt{s_{NN}}$ =2.76 TeV **97**
A.1 (Precursor) Suppression formalism 98
A.2 Recombination mechanism 101
A.3 Survival probability 101
A.4 Summary 103

References **105**

List of Publications and Presentations **B-2**

Brief Biography of the Supervisor **B-4**

Brief Biography of the Candidate **B-6**

List of Figures

1.1 Particles in Standard Model with the blue line indicating a particle's or a group of particle's interaction with other particles or itself/themselves. All gauge bosons except photon (below Schwinger limit) interacts among themselves. Neutrinos interact in the Standard Model only through weak interactions and are massless. Image source [5]. 3

1.2 Measurements of the Running coupling constant of QCD as a function of scale Q obtained by using the CT10 next-to-leading order PDF set [7]. The solid line and the uncertainty band are obtained by evolving the calculated coupling with reference as Z-boson mass, $\alpha_s(m_Z)$. The values are calculated for 2-loop 5-flavor RGEs. Image source [7]. 7

1.3 (Left) A sketch of QCD phases in the space of net-baryon chemical potential (μ_B), temperature (T), and light quark masses ($m_{u,d}$). Image source [12]. Hypothesized QCD phase diagram as the temperature of the bulk QCD matter plotted as a function of net chemical potential. Image source [13]. See text for details. 9

1.4 Overview of various stages of relativistic heavy-ion collision with typical time scales. Image source [23]. 11

1.5 Spacetime diagram of a collision event marked with various stages and temperatures. Image source [27]. See text for details. 12

1.6 Origin of collectivity. (Left) The overlap region of the two nuclei in the non-central collision produces spatial anisotropy in the fireball. (Right) The resulting anisotropy in the momentum space. The dotted lines represent surfaces of constant pressure. These lines are closer along the reaction plane, indicating larger pressure. Image source [40]. 14

1.7 Various terminologies used for real photons produced in heavy-ion collision depending upon different mechanisms in which they are generated. Image source [51]. 16

1.8 Transverse momentum integrated yields of Kaon (black), Lambda (blue), Xi (green) and Omega (red) particles scaled to pion yields as a function of $\langle dN_{ch}/d\eta \rangle$ at midrapidity [52]. For each particle species, the data points seem to lie on the respective particle species curve irrespective of the collision system or energy of collision. Image source [53]. 18

2.1 Self-energy diagram of a heavy quarkonium. The single and double lines are the representatives of the color singlet and doublet propagators. The singlet state on the right emits an ultrasoft gluon (curly lines) and transitions into a color doublet state at the chromoelectric dipole vertex (dot), which then transitions back after reabsorbing the same soft gluon. In the case of the quarkonium in QGP, the soft gluon is facilitated by the plasma medium. Image source [66]. . 24

2.2 (Left) Comparison of Coulomb and Yukawa potentials. Image source [70]. (Right) The plot of free energy of quark anti-quark pair, $F_{q\bar{q}} - T\ ln\ 9$ in the continuum limit, which is a quantity analogous to the potential between quark and anti-quark pair with appropriate normalization convention. Image source [71]. 29

2.3 The ratio of nuclear parton distribution function to free parton distribution function ($R_i^A = F_i^{p \in A}(x, Q^2)/F_i^p(x, Q^2)$) is plotted on the y-axis, as a function of the Bjorken x variable on the x-axis. Bjorken x represents the fraction of hadron momentum that parton caries. The smaller than unity feature of R_i^A is called small-x shadowing, responsible for nuclear shadowing effect. Image source [74]. . 31

3.1 Pion(π^+) rapidity spectra for the two mentioned LHC energies from ALICE (symbols), normalized to their respective maxima for the most central collision (with impact parameter, b) compared with those obtained from ECHO-QGP (line). 38

3.2 Pion(π^+) p_T spectra from experiments (symbols) compared with those obtained from ECHO-QGP (lines) for the mentioned LHC energies and centralities. 39

3.3 Pion(π^+) elliptic flow from experiments (symbols) compared with those obtained from ECHO-QGP (lines) for the mentioned LHC energies and centralities. 40

3.4 The transverse temperature profile for 2.76 TeV collisional energy in ECHO-QGP at $N_{part} = 130$, rapidity $= 1.44$ at $\tau = 3.1$ fm/c which is taken as the formation time of $\Upsilon(3S)$. The region inside the contour of $T_D = 236$ MeV for $\Upsilon(3S)$ state depicts the screening region. As it is not for the most central collision, the fireball cross section is oval-shaped. 45

3.5 Centrality dependence of suppression for Υ compared with measured R_{AA} at $\sqrt{s_{NN}} = 2.76$ TeV. 48

3.6 Transverse momentum dependence of suppression for Υ compared with measured R_{AA} at $\sqrt{s_{NN}} = 2.76$ TeV 48

3.7 Rapidity dependence of suppression for Υ compared with R_{AA} at $\sqrt{s_{NN}} = 2.76$ TeV. 49

3.8 Centrality dependence of suppression for Υ compared with R_{AA} at $\sqrt{s_{NN}} = 5.02$ TeV. 49

3.9 Transverse momentum dependence of suppression for Υ compared with R_{AA} at $\sqrt{s_{NN}} = 5.02$ TeV. 50

3.10 Rapidity dependence of suppression for Υ compared with R_{AA} at $\sqrt{s_{NN}} = 5.02$ TeV. 50

4.1 Stationary ideal fluid flow with a velocity gradient along y-direction is represented by thick yellow arrows. The thin blue arrows depict the flow of microscopic fluid constituents, which can transfer momentum from x to y direction, which will disrupt the stationary flow. Image source [141]. 55

4.2 The plot depicts a typical contour considered for solving the complex frequency integral in Eq. (4.36) for a given value of $\mathbf{k}$. The retarded correlator is analytic in the upper quadrants of complex plane [141]. The singularities for different microscopic theories could take the form of single poles or branch cuts of the two point retarded correlator, $G_R^{\mu\nu,\alpha\beta}(\omega, \mathbf{k})$, in the lower half of the complex plane. Such singular contributions could be called a mode. There could be finite or infinite modes of a microscopic model. The modes nearest to the real axis are dominant, and they are the least damped ones. Image source [149]. 62

4.3 Analytic structure appearing in different microscopic models of fluids. All self-interacting systems with Lorentz symmetry have hydrodynamic poles (blue cross) in the long wavelength limit. The non-hydrodynamic sector varies among theories and closely depicts the degrees of freedom of the underlying microscopic theory. The goal is to determine the underlying QGP dynamics in high energy collisions and their analytic structure. Image source [154] 64

4.4 The thick arrows correspond to the shear mode of the inhomogeneous velocity profile $v_x(y)$ of the flow of the medium. When the medium is in local thermal equilibrium, the sound and shear modes generate fluctuations represented by wiggly arrows. The propagation of these modes and the interaction between them contribute to the generation of shear viscosity. Image source [141]. 67

5.1 The four domains of hadron production are separated by two thresholds. Out of which the onset of deconfinement at low mass nuclei interactions is questionable. Finding the presence of these thresholds and their location is the aim. The present study deals with the onset at high $\sqrt{s_N}$ regime. Image source [27] 71

5.2 Energy density distribution as a function of transverse coordinate at $\tau = 0.6$ fm, midrapidity for 14 centrality classes of Au-Au IP-Glasma runs at 200 GeV. The distribution for each centrality class has been superimposed for 400 IPGlasma events with different nucleon positions to account for event-by-event fluctuations. 72

5.3 Pion(π^+) p_T-spectra generated (lines) for Au-Au at 200 GeV (left) and Pb-Pb at 2.76 TeV (right) for mentioned centrality classes compared with the corresponding PHENIX [195] and ALICE experimental results [196] (symbols). 73

5.4 Charged particle multiplicity rapidity spectra generated (lines) for Au-Au 200 GeV (above) and Pb-Pb 2.76 TeV (below) as a function of the number of participants compared with corresponding PHENIX[195] and ALICE[197, 198] experimental data (error bars). The generated data points are labeled with the midpoint of the centrality range in blue color. 74

5.5 Spatial eccentricity (red) and momentum space eccentricity (blue) for the viscous case for Au-Au 200 GeV system (left) and Pb-Pb 2.76 TeV system (right) for the two mentioned relaxation times at $50-60\%$ centrality. 76

5.6 Pion mean p_T as a function of centrality for Au-Au at 200 GeV and Pb-Pb at 2.76 TeV. The corresponding experimental data for Pb-Pb from ALICE[197] and for Au-Au from STAR[207] have systematic errorbars. 77

5.7 Pion(π^+) elliptic flow coefficient(v_2) as a function of transverse momentum(p_T) for 14 centrality classes for Au-Au 200 GeV system obtained with (IPGlasma+2Dhydro) set up along with experimentally measured elliptic flow (blue) from PHENIX [228] for the relaxation/non-hydrodynamic mode decay time, $\tau_\pi = 3\eta/sT$ (green) and $12\eta/sT$(red). The shaded area (yellow) highlights the difference in flow due to variations in relaxation time. 83

5.8 Experimental values of flow coefficients as a function of transverse momentum. Plot taken from [178]. Phenomenological studies that make use of viscous hydrodynamics have been able to explain flow experimental data only in the low p_T range. Beyond $p_T \approx 4$ GeV, the presence of a non-hydrodynamic mode has been suggested. . . . 83

5.9 Pion(π^+) elliptic flow coefficient as a function of transverse momentum(p_T) for 14 centrality classes for Pb-Pb 2.76 TeV collision system obtained with (IPGlasma+2Dhydro) setup along withe elliptic flow measured at ALICE[229] (blue) for relaxation time $\tau_\pi = 3\eta/sT$(green) and $8\eta/sT$(red). The shaded area (violet) highlights the difference in flow due to variations in relaxation time. See the text for an explanation. 85

5.10 Un-normalized p_T integrated elliptic flow of charged particles as a function of N_{ch} rapidity density for Au-Au 200 GeV (left) and Pb-Pb 2.76 TeV (right) plotted for the two mentioned relaxation times. Data points are labeled by the centrality values. The separation between the two curves is better seen for the un-normalized elliptic flow than for the normalized one shown below. 86

5.11 p_T integrated elliptic flow in *proton-proton* collision at 7 TeV produced using SONIC model, as a function of multiplicity pseudorapidity spectra for the mentioned values of η/s and ζ/s. For $\eta/s = 0.08$ and $\zeta/s = 0$ (blue), the elliptic flow has an errorbar due to variation in shear relaxation or non-hydro mode decay time, which increases in size for decreasing $dN/d\eta$. Plot taken from [178]. 87

5.12 p_T integrated elliptic flow of charged particles as a function of N_{ch} rapidity density for Au-Au 200 GeV (left) and Pb-Pb 2.76 TeV (right) plotted for the two mentioned relaxation times. Data points are labeled by the centrality values. See the text for an explanation. 88

5.13 Temperature contours as a function of coordinate x and proper time *tau* for Au-Au collisions at 200 GeV energy for decreasing impact parameter of collision. The temperature contour which roughly marks the pseudo-critical temperature is highlighted. We can notice the decreasing system size and corresponding lifetimes. From Figs. (5.12) and (5.10), the abrupt separation between the two flow curves begins roughly at the centrality bin 80-85%. One can qualitatively associate the actual spacial extension of a system at this centrality bin with the temperature contour of this centrality, and hence the smallest system size that can hydrodynamize. 90

1 The survival probability (S_P) of D^0 meson is plotted and compared with R_{AA} as a function of centrality at mid-rapidity at $T_D = 1.5T_c$. 102

2 The survival probability (S_P) of D^0 meson is plotted and compared with R_{AA} as a function of centrality at mid-rapidity at $T_D = 2T_c$. . 103

3 The survival probability (S_P) of D^0 meson R_{AA} as a function of traverse momentum at mid-rapidity at $T_D = 1.5T_c$. 103

4 The survival probability (S_P) of D^0 meson R_{AA} as a function of traverse momentum at mid-rapidity at $T_D = 2T_c$. 104

List of Tables

2.1 Energy scales relevant for the dynamics quarkonium in QGP medium. 21

3.1 The Key parameters used as input in ECHO-QGP. 40

List of Symbols and Acronyms

Λ_{QCD}	QCD scale
T_{pc}	Pseudocritical temperature
$T^{\mu\nu}$	Energy Momentum Tensor
$\Pi^{\mu\nu}$	Viscous Stress Tensor
$\pi^{\mu\nu}$	Shear stress tensor, traceless part of Viscous Stress Tensor
m_{D}	Debye mass
N_{c}	Number of color charges
N_{f}	Number of flavors
η	Shear viscosity
ζ	Bulk viscosity
τ_{π}	Shear relaxation time
$\sqrt{s_{\mathrm{NN}}}$	Total collision energy per nucleon-nucleon pair in the center-of-mass frame
N_{PART}	Number of participating nucleons in the collision
p_T	Transverse momentum
R_{AA}	Nuclear modification factor for nucleus-nucleus collisions
S_p	Survival Probability
v_2	Elliptic Flow
ω_h	Hydrodynamic mode frequency
ω_{nh}	Non-hydrodynamic mode frequency or transient mode frequency

EFT	Effective Field Theory
PDF	Parton Distribution Function
nPDF	nuclear Parton Distribution Function

DGLAP	Dokshitzer–Gribov–Lipatov–Altarelli–Parisi (equation)
CNM	Cold Nuclear Matter Effect
DIS	Deep Inelastic Scattering
NLO	next to leading order
QGP	Quark-Gluon Plasma
RGE	Renormalization Group Equation
LHC	Large Hadron Collider
HIC	Heavy Ion Collision
SLAC	Stanford Linear Accelerator Center
BNL	Brookhaven National Laboratory
CERN	European Organization for Nuclear Research (*translated*)
ALICE	A Large Ion Collider Experiment
CMS	Compact Muon Solenoid
PHENIX	Pioneering High Energy Nuclear Interaction Experiment
EOS	Equation of State
HRG	Hadron Resonance Gas
WB	Wuppertal-Budapest Collaboration
RHIC	Relativistic Heavy-ion Collider
pQCD	perturbative QCD
pNRQCD	potential Non-Relativistic QCD
RM	Relative Motion coordinate frame
CM	Center of mass coordinate frame
QFT	Quantum Field Theory
AdS/CFT	Anti-de Sitter/Conformal Field Theory
CGC	Colour Glass Condensate
MIS	Müller-Israel-Stewart
BRSSS	Baier-Romatschke-Son-Starinets-Stephanov formalism

Chapter 1

Introduction to quark-gluon plasma

Any physical interaction in nature in any phenomena at any scale or energy manifests as just one of the four fundamental forces. Electromagnetism first took a coherent classical form in classical Maxwell's equations (1862) and then later as quantum electrodynamics (QED) (1950s). The nuclear decay process alluded to the discovery of weak interaction (1933). The strong interaction governing the bound state of quarks was explained by quantum chromodynamics (QCD) (1970s). The framework of all the above three fundamental interactions is quantum field theory. In which each type of particle is an excitation of the underlying quantum field. For energies higher than roughly 246 GeV, electromagnetism and weak interaction combine into a single force [1–3]. This unification, whose idea first came up in (1967) [4], has been formulated into *electroweak theory*. These electroweak and strong interactions are put together in *the Standard Model* of particle physics, which has been one of the most remarkable achievements of the last century. However, general relativity's gravitation has stayed aloof from this picture. Moreover, the standard model is inadequate to explain neutrinos with masses and baryonic asymmetry among many other phenomena. Hence certainly, the standard model is lacking, and there is a need to branch out of it to a more comprehensive framework. But before that, there is a need to get a good hold of

QCD itself, which has been elusive due to difficulties involved in probing quark matter experimentally. On the theoretical front, QCD poses a challenge in the non-perturbative regime, even with Lattice QCD. Recently some progress has been made in figuring out a few of the approximate features of the QCD phase diagram, but there is a lot to be done.

1.1 Quantum chromodynamics

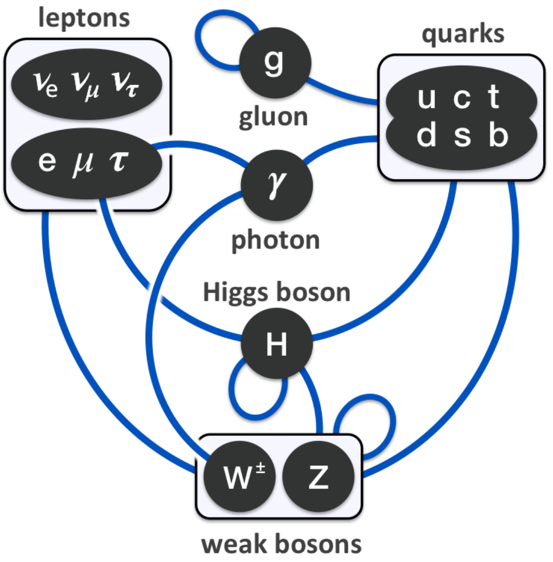

Figure 1.1: Particles in Standard Model with the blue line indicating a particle's or a group of particle's interaction with other particles or itself/themselves. All gauge bosons except photon (below Schwinger limit) interacts among themselves. Neutrinos interact in the Standard Model only through weak interactions and are massless. Image source [5].

Fermions are half-odd-integer spin particles. Quarks are fermions with fractional electric charge as well as possessing color charge of strong interaction. There are three kinds of color charges, which are named *red*, *green*, and *blue*. Anti quarks carry the polar opposites of these, which are *anti-red*, *anti-green*, and *anti-blue*. So far, we know that quarks come in 6 flavors, *up*, *down*, *strange*, *charm*, *bottom*, and *top*. The historical account of the quark's discovery is quite interesting. In 1964 quarks were hypothesized to be the constituents of hadrons, independently by Murray Gell-Mann and George Zweig. Until then, hadrons were considered to be the fundamental particles with no internal structure. Nevertheless, after just four years, the existence of quarks was confirmed in a deep inelastic scattering experiment at the Stanford Linear Accelerator Center (SLAC). But quarks have not been seen in an isolated state. This is because the strong force between two quarks stays constant with an increase in separation between them. This is contrary to the electromagnetic force, which has an inverse relation with the separation of charges. This phenomenon is called color confinement and is peculiar to QCD. If one attempts to separate two quarks by applying energy, the process results in pair production of a new set of quark anti-quark pairs, forming color singlet states with original quarks. The color singlet states are hadrons(mesons or baryons), also called color-neutral states. However, above certain temperature/pressure, the kinetic energy of constituent quarks should overcome confinement.

In quantum field theory, the motion of a free fermion of rest mass, m is given by the Dirac equation,

$$(i\gamma^{\mu}\partial_{\mu} - m)\,\psi(x) = 0 \tag{1.1}$$

Here, $\psi(x)$ is the Dirac field, also called Dirac spinor and $\gamma^{\mu} = \{\gamma^0, \gamma^1, \gamma^2, \gamma^3\}$ are the gamma or Dirac matrices. This equation is obtained by solving the Euler-Lagrange equation with the Lagrangian density:

$$\mathcal{L}_D = \overline{\psi}(x)\, i\gamma^{\mu}\partial_{\mu}\psi(x) - m\,\overline{\psi}(x)\psi(x), \tag{1.2}$$

where, $\overline{\psi}(x) \equiv \psi^{\dagger}\gamma^0$ is the adjoint Dirac field.

In electromagnetism, we found that the electric charge is always conserved. From Noether's theorem we know that for every global symmetry in the system, there is a conserved quantity. The QED Lagrangian is unaffected by phase transformation in a fermionic field of the kind, $\psi(x) \to e^{i\alpha}\psi(x)$ and $\overline{\psi}(x) \to e^{-i\alpha}\,\overline{\psi}(x)$. If α is chosen as a real number, then this symmetry of Lagrangian is global. And this results in conserved electromagnetic current and charge. But if we allow the α parameter to be coordinate-dependant, then the symmetry is localized. And then we additionally need to introduce a gauge covariant derivative in the Lagrangian, $\partial_{\mu} \to D_{\mu} \equiv \partial_{\mu} + ie\mathcal{A}_{\mu}$, in order to keep the Lagrangian invariant. Here $\mathcal{A}_{\mu}$ is called a gauge field, which in this case is the photon field. The gauge boson is the photon here, the excitation of the photon field. The parameter α could be considered the single element matrix of the unitary, U(1) group, governing the gauge symmetry in QED. Theories which have such local symmetries are called *gauge theories.*

QCD is a non-abelian gauge theory or often called Yang-Mills theory, after the names of its discoverers [6] coupled minimally to the quarks. The non-Abelian gauge group associated with QCD is SU(N_c), and the corresponding charge is called 'color'. The quark flavors belong to the fundamental representation of this gauge group, SU(N_c), and have dimension $N_c = 3$, which is the number of colors any given quark can possess. The color interaction mediating gauge boson here are the massless gluons, which transform like connections in the adjoint representation of dimension $N_c^2 - 1 = 8$. Hence QCD has eight kinds of gluons. Their lie algebra is given as:

$$\left[\lambda^a, \lambda^b\right] = 2i \sum_{c=1}^{8} f^{abc}\, \lambda^c, \tag{1.3}$$

where λ^c are 3×3 traceless Hermitian matrices called "Gell-Mann matrices" which are closed under multiplication and are given as:

$$\lambda^8 = \frac{1}{\sqrt{3}}\begin{pmatrix}1 & 0 & 0\\ 0 & 1 & 0\\ 0 & 0 & -2\end{pmatrix}; \quad \lambda^7 = \begin{pmatrix}0 & 0 & 0\\ 0 & 0 & -i\\ 0 & i & 0\end{pmatrix}; \quad \lambda^6 = \begin{pmatrix}0 & 0 & 0\\ 0 & 0 & 1\\ 0 & 1 & 0\end{pmatrix};$$

$$\lambda^5 = \begin{pmatrix}0 & 0 & -i\\ 0 & 0 & 0\\ i & 0 & 0\end{pmatrix}; \quad \lambda^4 = \begin{pmatrix}0 & 0 & 1\\ 0 & 0 & 0\\ 1 & 0 & 0\end{pmatrix}; \quad \lambda^3 = \begin{pmatrix}1 & 0 & 0\\ 0 & -1 & 0\\ 0 & 0 & 0\end{pmatrix};$$

$$\lambda^2 = \begin{pmatrix}0 & -i & 0\\ i & 0 & 0\\ 0 & 0 & 0\end{pmatrix}; \quad \lambda^1 = \begin{pmatrix}0 & 1 & 0\\ 1 & 0 & 0\\ 0 & 0 & 0\end{pmatrix} \tag{1.4}$$

In the commutation relation of Eq. (1.3) above, f^{abc} are called the structure constants, which are anti-symmetric in all three indices, given as

$$\begin{aligned} f^{458} &= f^{678} = \frac{\sqrt{3}}{2} \quad ; \quad f^{123} = 1 \\ f^{257} &= f^{147} = f^{165} = f^{246} = f^{376} = f^{345} = \frac{1}{2} \\ f^{abc} &= 0 \quad \text{for all other combination of indices.} \end{aligned} \tag{1.5}$$

There are two kinds of SU(3) gauge symmetries in QCD. The first SU(3) symmetry is of color charge between quarks. What it means is that the color charges do not distinguish between quark flavors. The second approximate SU(3) symmetry is among the 3 lightest quark flavors, viz. *up*, *down* and *strange*. Due to this symmetry, these three quarks could be interchanged in a process as there is a small relative difference in their rest masses. The QCD Lagrangian density is given as,

$$\mathcal{L}_{\mathrm{QCD}} = -\frac{1}{4} G_a^{\mu\nu} G^a_{\mu\nu} + \sum_f \overline{\psi}_f (i\gamma^\mu D_\mu - m_f)\psi_f, \tag{1.6}$$

where f is the quark flavour index ($f = u$, d, c, s, t, b) and $G^a_{\mu\nu}$ is the Yang-Mills field strength tensor given as:

$$G^a_{\mu\nu} = \partial_\mu A^a_\nu - \partial_\nu A^a_\mu - g f^{abc} A^b_\mu A^c_\nu. \tag{1.7}$$

D_μ in Eq. (1.6), is the gauge-covariant derivative which couples the quark field (ψ_f) to the gluon fields (A^a_μ) with a coupling strength g through the infinitesimal SU(3) generators $T^a = \frac{1}{2}\lambda^a$ in the fundamental representation as,

$$D_\mu = \partial_\mu + igA^a_\mu T^a \tag{1.8}$$

where a = 1 . . . 8 and the repeated color index is implicitly summed.

1.1.1 Running coupling constant, asymptotic freedom, and quark confinement

In classical field theory, like electrodynamics, the force between charges is of the form $F = k_e \frac{q_1 q_2}{r^2}$, where k_e is the coupling constant deciding the strength of the interaction. In quantum field theory, the coupling arises in the Lagrangian as the coefficient of the gauge field in the gauge covariant derivative. The QCD coupling constant depends on the energy scale (μ) at which we are probing the coupling. This is why we refer to the strong interaction coupling as "running of the coupling," and is explained with the renormalization group. The renormalization group is a more general concept that describes any kind of scale variation in a physical system. From our present understanding, we cannot observe an isolated elementary particle like an electron or quark. This *bare particles* are an excitation of the elementary quantum field, which we can write in a Lagrangian. But bare particles are not identical to the ones detected in experiments. The observed real particles are called *dressed* or *clothed particles* which are surrounded by a *cloud*

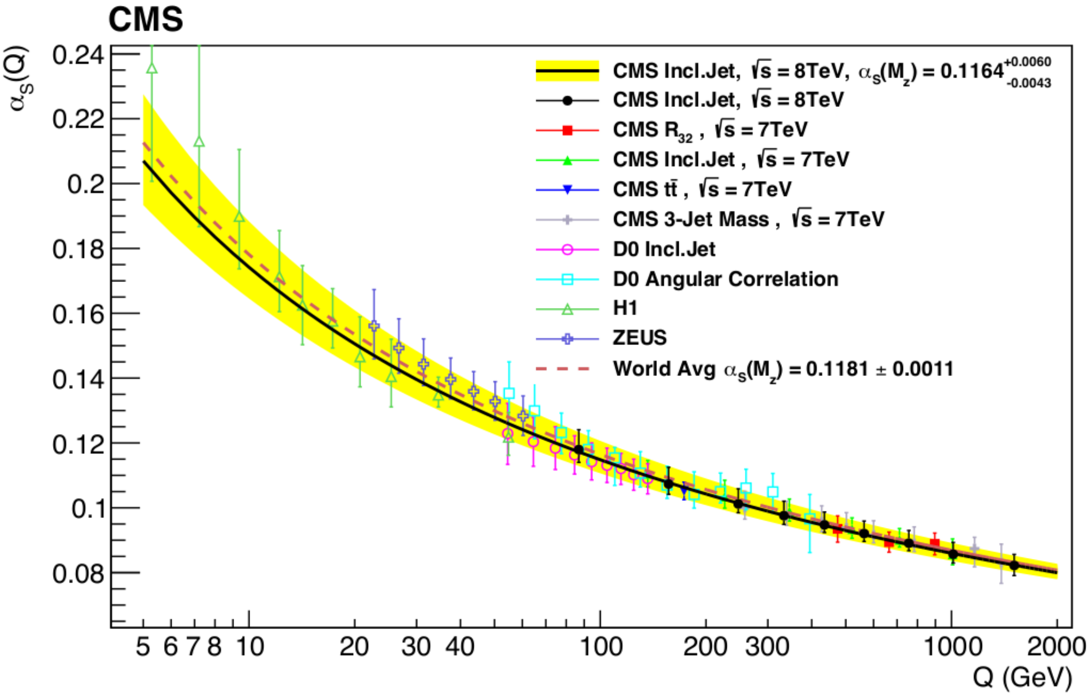

Figure 1.2: Measurements of the Running coupling constant of QCD as a function of scale Q obtained by using the CT10 next-to-leading order PDF set [7]. The solid line and the uncertainty band are obtained by evolving the calculated coupling with reference as Z-boson mass, $\alpha_s(m_Z)$. The values are calculated for 2-loop 5-flavor RGEs. Image source [7].

or *sea* of virtual particles lying off shell.

The renormalization exhibits a transformation group that transfers quantities from the bare terms to the dressed terms. In other words, the virtual quark sea forms a notional *covering* induced by the renormalization group. We encounter divergent loop integrals while quantizing a theory. As QCD is a renormalizable theory, there are finite superficially divergent amplitudes, and these divergences can be eliminated by replacing bare parameters of the QCD Lagrangian (i.e., the bare coupling and fermion masses) with the renormalized parameters measured at an arbitrary scale, μ, referred to as the *renormalization scale.* Assuming we know the strong coupling constant $\alpha_s \equiv \frac{g^2}{4\pi}$ at an energy scale Q^2, the required renormalization group equation (RGE) that gives the energy dependence can be derived from Callan-Symanzik equation. Considering massless fermions, the RGE for strong coupling constant is given as,

$$Q^2 \frac{\partial}{\partial Q^2} \alpha_s(Q^2) = \beta \left(\alpha_s(Q^2)\right), \tag{1.9}$$

where $Q = |q|$, and q is four-momentum exchanged in the process. The β function of QCD on the right-hand side can be computed perturbatively by finding the relevant Green functions and, generally, expressed as a series in terms of coupling.

$$\beta = -2\alpha_s \left(\frac{\alpha_s}{4\pi}\beta_0 + \frac{\alpha_s^2}{(4\pi)^2}\beta_1 + \dots\right). \tag{1.10}$$

The QCD β function depends on the renormalization scheme used and also on the gauge. But in a mass-independent regularization scheme like MS (minimal subtraction) scheme, the β-function is also gauge-independent [8, 9]. The first coefficient for the one-loop case is given as [10, 11]

$$\beta_0 = \left[\frac{11}{3}C_A - \frac{2}{3}n_f\right], \tag{1.11}$$

where n_f is the number of quark flavors that, at a given energy scale, can be considered to be massless. We approximate the RGE (Eq. (1.9)) using the truncating the β-function expansion to leading order term, to obtain:

$$\alpha_s(Q^2) = \frac{\alpha_s(\mu^2)}{1 + \beta_0 \frac{\alpha_s(\mu^2)}{\pi} \log \frac{Q^2}{\mu^2}}, \tag{1.12}$$

where μ is an arbitrary reference scale. We define the QCD scale, $\Lambda_{\rm QCD}$ as the scale at which the coupling $\alpha_s(\Lambda_{\rm QCD})$ diverges, which breaks down the perturbation theory. At the leading order, we have,

$$\alpha_s(\mu) = \frac{2\pi}{\beta_0 \log \frac{\mu}{\Lambda_{\rm QCD}}}. \tag{1.13}$$

We can trust the perturbative expansion of QCD only when $Q \gg \Lambda_{\rm QCD}$. As $g(\Lambda_{\rm QCD}) \sim 1$, one can say that for $Q \ll \Lambda_{\rm QCD}$ the theory is coupled strongly (*confinement*), and for $Q \gg \Lambda_{\rm QCD}$ it is weakly coupled (*asymptotic freedom*). It is due to this confinement principle that any attempt to split a hadron never produces an isolated quark but more hadrons in color-neutral states.

1.1.2 Quark-Gluon plasma

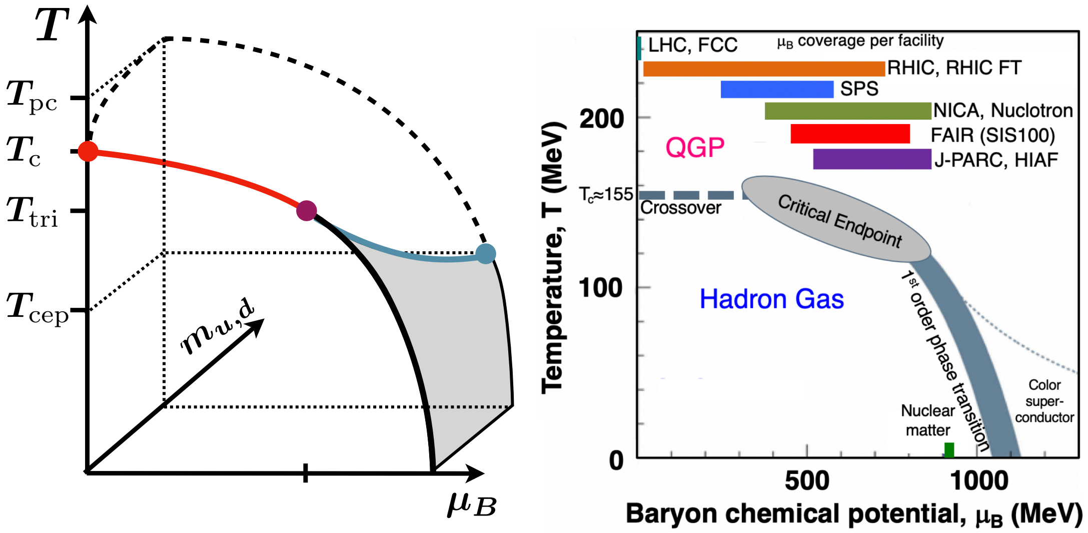

Figure 1.3: (Left) A sketch of QCD phases in the space of net-baryon chemical potential (μ_B), temperature (T), and light quark masses ($m_{u,d}$). Image source [12]. Hypothesized QCD phase diagram as the temperature of the bulk QCD matter plotted as a function of net chemical potential. Image source [13]. See text for details.

Any attempt to break a hadron (baryon or meson) by supplying energy leads to the production of more quark anti-quark pairs which participate in producing new color neutral states. This is the essence of the quark confinement principle we mentioned in the previous section. But if the high temperature and/or high-density medium conditions are maintained for sufficient duration, the hadrons would melt into a soup of quarks and gluons called **Quark-Gluon Plasma** (QGP), the idea of which first took shape in late 1970s [14, 15].

Fig. (1.3)(right) shows the speculative phase diagram of strongly interacting matter in the space of temperature and net-chemical potential. This diagram is the backplane of the 3D phase diagram of QCD shown in the Fig. (1.3)(left). This 3D phase diagram has physical strange quark mass but varying light quark masses. Quark masses are the experimental inputs in QCD theory. The front plane of the 3D phase diagram corresponds to zero light quark masses and consists of a second-order transition curve (red line) meeting the first-order transition curve (solid black line) at the tri-critical point (magenta dot). A tri-critical point is defined as a point at which 3 distinct coexisting phases become identical. The other end of the second-order transition line in the zero light quark mass plane meets the temperature axis at the critical point (red dot). A critical point is the one at which 2 distinct coexisting phases become identical. The blue curve is the locus of second-order order transition points meeting the plane of physical light quark masses at the critical endpoint (blue dot), marks as T_{cep} on the temperature axis.

We are yet to locate the critical endpoint, as can be seen by the patch in Fig. (1.3)(right). The net baryon chemical potential axis could be understood as the baryon density axis. Low μ_B corresponds to medium when the number of baryons and anti-baryons are almost equal. With increasing μ_B, the system has more baryons than anti-baryons. Near zero μ_B-T value, we have the QCD vacuum. Critical point and pseudo-critical point temperatures are sometimes interchangeably used in literature, and the region between extending up to the critical endpoint is referred to as *crossover*. In Fig. (1.3)(right) region under crossover, critical endpoint and first-order phase transition line are occupied by hadron gas. It is the region where quarks are still confined to hadrons. Furthermore, the unbounded region above it is all QGP. At large μ_B and low temperature, a *color superconductor* state is predicted. The core of neutron stars could also be placed somewhere in the large μ_B and low-temperature region. The lower end of the small green line on the μ_B axis corresponds to regular nuclear matter. All nuclei of the periodic table lie on this single point. This small green line marks the nucleon gas-to-liquid phase transition. Various collision experiments are and will be attempting to probe a range of μ_B marks as corresponding bands at the top region of the plot. LHC collisions correspond to a small patch at low μ_B and high-temperature region of this phase diagrams as shown.

The largest portion of the speculative phase diagram of the QCD is occupied by this QGP [16, 17]. This phase supposedly existed in the early universe for a short time around the *quark epoch* before the formation of baryonic matter. The only accessible laboratory for probing this state is high-energy collision experiments, where quark matter could exist as a transient stage. So far, the experimental findings indicate the formation of an inviscid medium [18, 19]. A theoretical lower limit for the shear viscosity to entropy density ratio (η/s) of strongly interacting matter has been known for a while [20]. However, the estimation of such low η/s for quark matter in heavy-ion collisions has become possible only recently using lattice QCD [21], and *Bayesian parameter estimation methods* [22].

1.2 Stages of high energy collision

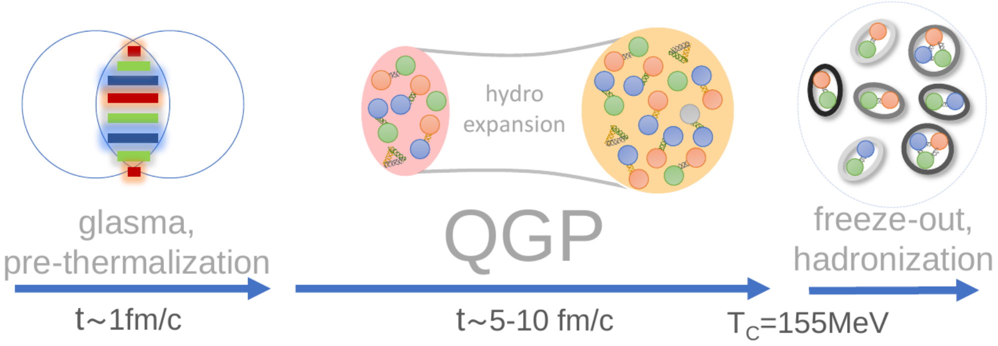

Figure 1.4: Overview of various stages of relativistic heavy-ion collision with typical time scales. Image source [23].

What makes this problem of characterizing QGP so difficult is the sheer complexity of the system. In high-energy collisions, the only variables in our control are particle species and the energy of the collision. All the rest has to be inferred indirectly from the observables. Predicting the transport and thermodynamic properties of a medium formed in the collision by analyzing patterns in the produced particle yields is a scrupulous task. Hence, modeling of such a complex system can only be dealt phenomenologically [24]. Fig. (1.4) shows the big picture of high energy heavy-ion collisions which emerged from the interplay of theoretical, experimental, and phenomenological progress over the last decade. Right at the moment of collision, from what we expect, partons in the participating nucleons from the Lorentz contracted nuclei strongly interact with each other producing a region of coherent chromoelectric and chromomagnetic fields called *glasma*. These fields evolve, and the deposited energy is highly inhomogeneous. The fireball expands until it reaches close-to-equilibrium, and this stage is referred to as *pre-equilibrium*, and it lasts for about 1 fm/c [25, 26]. The use of low-order hydrodynamics as the next stage of collision is purely motivated by its phenomenological success in explaining soft sector experimental observables. The duration for which this stage lasts in LHC and RHIC is around 5-10 fm/c. This stage is dominated by QGP and it continues until the system has cooled enough for hadronization to begin. *Hadronization* is the stage where quarks combine into color neutron hadrons (baryons and mesons) which are then detected. This is a relatively simple yet compelling picture of the complete evolution of the fireball. The unreasonable success of this description is what, for now, allows us to keep using it. However, the actual physical dynamics need not have such a distinct separation between stages, which we explain next.

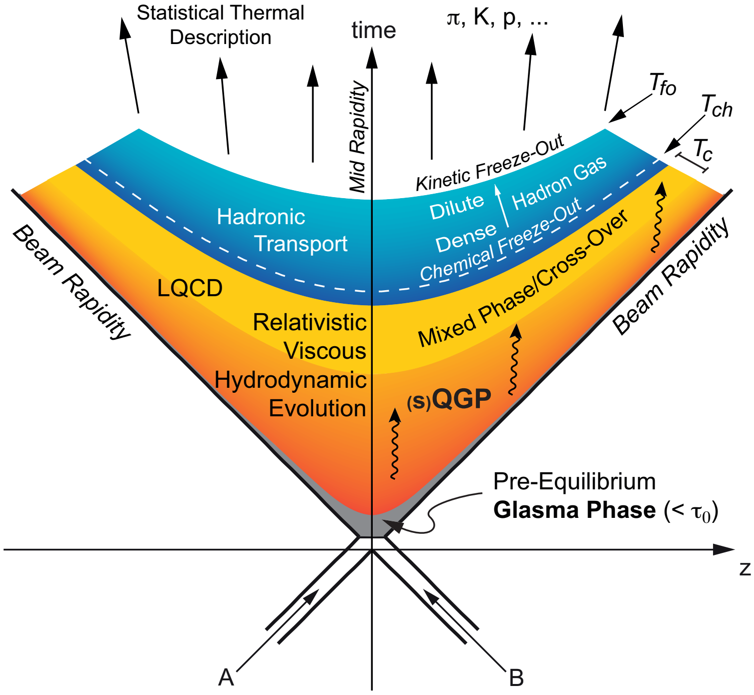
Statistical Thermal Description
time
π, K, p, ...
Mid Rapidity
T_{fo}
T_{ch}
T_c
Kinetic Freeze-Out
Dilute
Hadron Gas
Dense
Chemical Freeze-Out
Hadronic Transport
LQCD
Relativistic Viscous Hydrodynamic Evolution
Mixed Phase/Cross-Over
Beam Rapidity
Beam Rapidity
(s)QGP
Pre-Equilibrium
Glasma Phase (< τ_0)
z
A
B

Figure 1.5: Spacetime diagram of a collision event marked with various stages and temperatures. Image source [27]. See text for details.

Fig. (1.5) provides a bit more detailed overview of the heavy-ion collision. We have no direct probe to investigate the initial stage of collision. Photons are produced in almost every stage of collision, but distinguishing between them is challenging. Quarkonia could potentially act as initial state observables as they are produced right after the early hard scattering stage. The hydrodynamic stage is modeled only for light quarks with an appropriate equation of state. However, there could also be heavy-light quarks, including any other resonances which can form at that system temperature. Each particle species can hadronize at different temperatures. Hence we need not have hadronization at sharp one instant. But instead, we would have a mixed phase as shown in Fig. (1.5). The pseudo-critical temperature (T_{pc}) should occur in this mixed region. The currently agreed upon value of T_{pc} for QGP computed by Lattice QCD collaborations is roughly 156 MeV [28–30]. Once hadronized, the particles will still undergo inelastic collisions among themselves, which could alter their species. This point is called chemical freezeout, and the corresponding temperature is marked as T_{ch}. Resonance decay could happen before this point. Beyond this point, the hadron gas cools further and gets dilute enough that even elastic collision also stops marking the kinetic freezeout (T_{fo}) point. The particles from this surface are captured in the detectors. The most abundant species are the lightest and stable ones, viz. pions, kaons, and protons.

1.3 Signatures of quark-gluon plasma in high energy collision

The medium created in high energy collision doesn't last beyond 20 fm/c and has a small spatial extent of a nuclear volume before it hadronizes into particles that decay into stable particles to be detected. Hence, the best we can do is to find the nature of the medium created to find correlations and patterns in the particles detected. Below we briefly discuss the indirect signatures that strongly indicate the formation of a thermalized quark-gluon medium. These signatures also help us deduce the properties of such a medium.

1.3.1 Jet quenching

The initial hard scattering at the point of collision produces hadrons through strong interactions, often resulting in a collimated cluster of final hadrons referred to as jets. Jets have been found in e^+e^-, proton anti-proton [31, 32] and lepton-proton [33] collisions as well, and their production rates are calculable in perturbative QCD [34]. This higher-order jet-production perturbative QCD calculations have become a standard tool for studies such as finding running coupling constant [35] and Higgs boson searches [36]. The phenomenon where the energetic partons in a jet lose their momentum due to interaction with the QGP medium is called *jet quenching* [37]. Perturbative QCD jet calculations for *proton-proton* collisions have shown agreement with experimental data [38]. Consider a jet parton propagating with multiple interactions with thermal partons in the thermalized medium. It will lose energy and result in transverse momentum broadening and suppression of final jet hadron spectra. The energy loss of partons is proportional to jet transport coefficient [39], which is the averaged transverse momentum broadening normalized to the unit length of propagation

$$\hat{q}_a = \sum_{b,(cd)} \int dq_\perp^2 \frac{d\sigma_{ab\to cd}}{dq_\perp^2} \rho_b q_\perp^2 \tag{1.14}$$

where index a is for jet parton colliding with medium parton of index b to produce partrons c and d, governed by the partonic scattering cross section $\sigma_{ab\rightarrow cd}$. ρ_b is the local density of medium parton inclusive of degeneracy and degrees of freedom and $q_\perp$ is the parton transverse momentum.

1.3.2 Collective flow

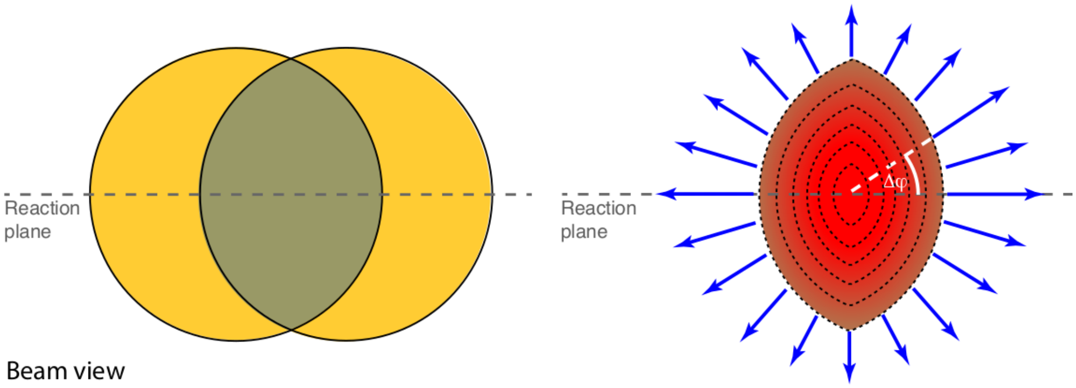

Figure 1.6: Origin of collectivity. (Left) The overlap region of the two nuclei in the non-central collision produces spatial anisotropy in the fireball. (Right) The resulting anisotropy in the momentum space. The dotted lines represent surfaces of constant pressure. These lines are closer along the reaction plane, indicating larger pressure. Image source [40].

The hadrons produced in the final stage of high-energy collisions possess a certain collective flow. By collective flow, we mean that the hadrons detected across different pseudorapidity and azimuthal angles are correlated to some extent. Jean-Yves Ollitrault in 1992 predicted that such flow in high energy collisions could shed some light on properties of hot and dense quark matter [41]. Unlike in the case of weakly interacting gas, where the azimuthal distribution of particles would be isotropic. The azimuthally anisotropic distribution of particles after freezeout reflects the existence of spatial fluctuations in earlier stages. To find the collective flow, we expand the azimuthal dependence of the invariant yield of particles in the Fourier space relative to the reaction plane [42].

$$E\frac{d^3N}{d^3p} = \frac{1}{2\pi}\frac{d^2N}{dy\; p_T\; dp_T}\Big(1+\sum_{n=1}^{\infty} 2\; v_n\; cos[n(\phi-\Psi_{RP})]\Big), \tag{1.15}$$

where the reaction plane(Ψ_R) is spanned by the impact parameter vector and the beam axis (z-axis). E is the particle energy with transverse momentum–p_T

detected at an azimuthal angle of ϕ with respect to the lab x-axis. y is the rapidity. The n^{th} harmonic coefficient, $v_n = \langle cos[n(\phi - \Psi_{RP})]\rangle$, are theoretical equivalent of the experimentally observable quantity. Only the cosine term is considered in the Fourier distribution because the sine terms vanish due to symmetry with respect to the event plane. In the modern picture, collective flow is modeled by considering a single particle azimuthal probability distribution, $P(\phi)$, which fluctuates from event to event [43] and is given as,

$$P(\phi) = \sum_{n=-\infty}^{\infty} V_n \, e^{-in\phi}. \tag{1.16}$$

Here, $V_n = v_n \, e^{in\Psi_{RP}}$ is a complex Fourier flow coefficient whose magnitude(v_n) and phase(Ψ_{RP}) fluctuate from event to event. This modern definition is convenient for finding multiparticle correlations between v_n and Ψ_{RP}. If QGP is fluid-like, the collective flow would primarily be of hydrodynamic origin. But flow could also arise due to some other effects like correlations among particles in jets, resonance decay, and vacuum QCD effects like partonic bremsstrahlung, interference, etc., which occurs mainly at very low multiplicities [44]. All these contributors are referred to as *non-flow effects* and are not related to the event plane [45]. To extract true hydrodynamic flow, various observables have been devised, viz., symmetric cumulants and correlations between the magnitudes or phases of the complex flow in different harmonics. Furthermore, various phenomenological models can obtain observables that match the experimental data [46, 47]. However, the detection of flow in small systems has further complicated the already difficult situation.

1.3.3 Quarkonia suppression

A bound state of heavy quark-antiquark (c,b,t) is referred to as quarkonium to describe which a nonrelativistic Schrödinger equation with phenomenological potential suffices. The heavy quark anti-quark pair forms in the early hard scattering stage of collision could form a bound state and evolve in the medium before it decays into lighter particles at freezeout. The bound state could dissociate in the hot medium of quarks and gluons, resulting in lesser production when compared to the scaled-up production in proton-proton collisions. Cornell potential developed in the 1970s has been widely used to model the quarkonia bound state is given as

$$V(r) = -\frac{4}{3}\frac{\alpha_s}{r} + \sigma\, r, \tag{1.17}$$

where α_s and σ are the running coupling constant and the QCD string tension, respectively. The first term in the potential is the coulombic part effective at short distances. The factor of 4/3 originates from the the color charge factor i.e. $\frac{(N_c^2-1)}{2N_c} = \frac{4}{3}$ for $N_c = 3$. The second term is the long-distance linear confining part. There are various mechanisms through which dissociation could happen in QGP. Some of these are gluonic dissociation, collisional damping, and color screening. There are ways in which dissociation could happen even if there were no such medium as QGP but just a multi-parton scattering environment. These effects are collectively called the *cold nuclear matter* effects. We will look at quarkonia suppression in detail in the next few chapters.

1.3.4 Direct photons

From what we know so far, in almost all stages of the collision, there exist processes for generating photons. If detected and identified, these photons could potentially tell us a lot about the mechanisms generating them and the environment around them. In general, photons at high transverse momentum ($p_T > 4$ GeV/c) are the probes of QCD hard scattering, whereas, at low p_T, they are generated via multi-particle production. The study of photons in collisions was first suggested in 1975 by Escobar [48], and in 1976 by Farrar-Frautschi [49], and Feinberg [50].

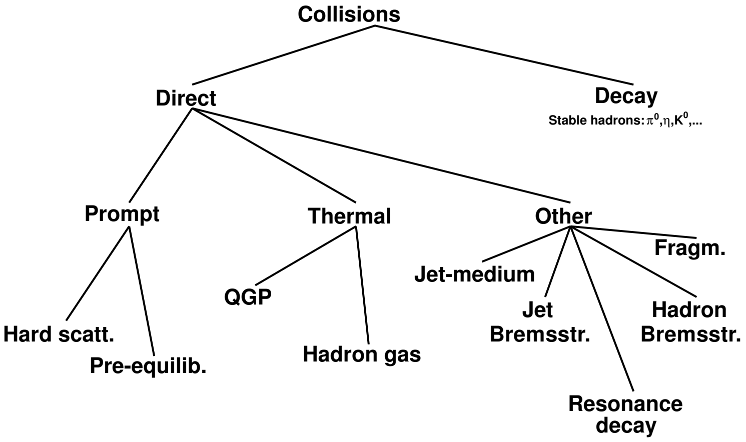

Figure 1.7: Various terminologies used for real photons produced in heavy-ion collision depending upon different mechanisms in which they are generated. Image source [51].

As photons are color neutral, they have a larger mean free path in the high-density hadronic medium and deconfined quark matter. This allows them to escape the interaction region mostly unaltered. The real photons produced before the freeze-out stage of the collision are termed *direct photons*. These are produced due to processes other than hadron decay (e.g., $\pi^0 \rightarrow \gamma\gamma$) and were considered to have a significant contribution from equilibrating QGP. Their number is usually smaller than the photons arising from the decay of final state hadrons, like η,π^0, etc. These hadron decay photons are interesting in their own right, but they also act as a difficult-to-subtract background for the direct photon. In Fig. (1.7), we see the hierarchy of photon generation in heavy ion collisions. Direct photons are categorized depending on the processes in which they are generated. Photons generated from initial hard scattering are mostly explained with pQCD processes like annihilation ($q\bar{q} \rightarrow g\gamma$) and Compton scattering ($gq \rightarrow q\gamma$). These are called *prompt* direct photons as they carry information about nuclear partons. The other category is of low p_T direct photon called *thermal*, which tells us about the temperature and collective evolution of the system. Earlier motivations were to gain access to the initial temperature of the system by considering direct photons as thermal radiation. And later on, the theoretical tools were developed to extract additional information on the initial condition, viscosity, and the effect of large even though the short-lived magnetic field, from the study of direct photons, [51]. Theoretical calculations have been struggling to explain all direct photon spectra and flow coefficients simultaneously, unlike hadrons. These problems have been termed "direct photon puzzle". At present, photons study at high p_T has helped us understand initial geometry. However, extraction of initial system temperature and estimation of QGP properties from low p_T direct photons has not been satisfactory. Direct photon's role in the initial collision state and the supposedly produced magnetic field is still under investigation.

1.3.5 Strangeness enhancement

A nucleon consists of *up* and *down* quarks, whose masses are 2.2 MeV/c^2 and 4.7 MeV/c^2, respectively. Being lightest, these two quarks are abundantly produced in high energy collisions than the strange quarks, which have a relatively large mass of 96 MeV/c^2. In the lowest order, there are two channels for strange quark production, viz. quark fusion($q\bar{q} \rightarrow s\bar{s}$) and gluon fusion ($gg \rightarrow s\bar{s}$). Johann Rafelski and Berndt Müller (1982) found that strange quark production is dominated by gluon fusion [54, 55]. Furthermore, the contribution from quark fusion is less than gluon fusion by almost an order of magnitude [56]. Johann Rafelski also found that the QGP lifetime has to be sufficiently large to maintain the tem-

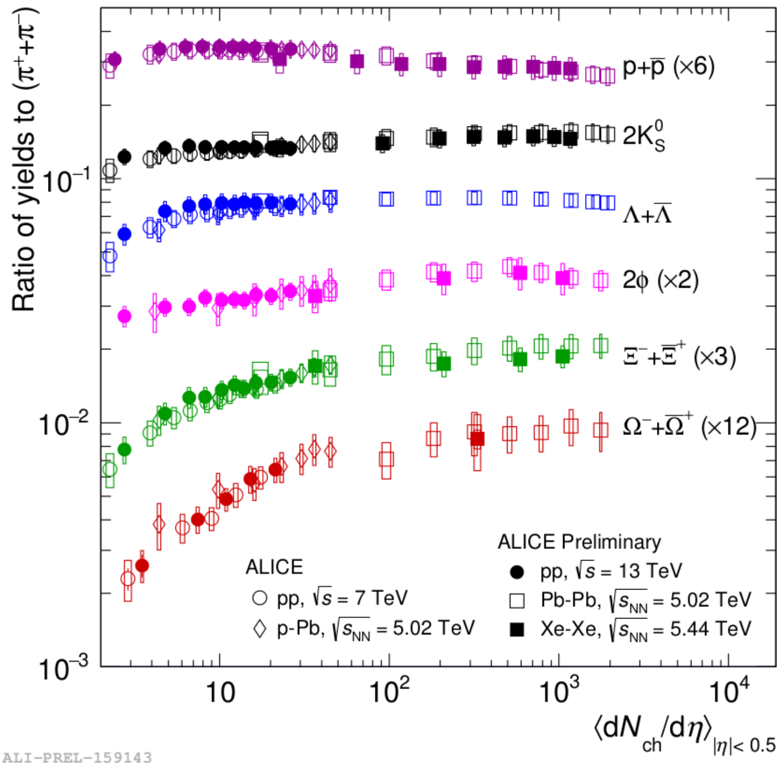

Figure 1.8: Transverse momentum integrated yields of Kaon (black), Lambda (blue), Xi (green) and Omega (red) particles scaled to pion yields as a function of $\langle dN_{ch}/d\eta \rangle$ at midrapidity [52]. For each particle species, the data points seem to lie on the respective particle species curve irrespective of the collision system or energy of collision. Image source [53].

perature, $T > 2m_s$, for the chemical equilibrium abundance of strange quarks to be equivalent to that of light quarks. The QGP lifetime monotonically increases with *number of participating nucleons* (N_{PART}) or system size. This equilibrium state of *up*, *down*, *strange* quarks, and gluons continue till freezeout. And after hadronization hence produces an abundance of strange hadrons compared to scaled-up *proton-proton* collision strangeness yields. Detection of abundant formation of multi-strange baryons like Omega [$\Omega(sss)$] and Xi [$\Xi(uss/dss)$] and their anti-particles strengthened the claim of QGP formation. As gluon fusion is more conducive in high-energy partonic medium, we expect enhancement of strangeness in QGP. The first experimental measurement was made by the CERN WA97 experiment and later by the STAR experiment by the RHIC facility, followed by CERN LHC. And recently, ALICE measurements have confirmed strangeness enhancement even in proton-nucleus, and high multiplicity proton-proton collision [52]. This measurement could help in finding the onset of deconfinement in small systems, which is an actively studied problem. Fig. (1.8) shows relative yields of four strange hadrons varying with charged particle multiplicity pseudorapidity density. The results obtained for Pb-Pb, p-Pb, p-p, and collisions for different energies appear to lie on the same curve for each strange hadron. This means that the relative production of strange particles across all systems does not depend on collision energy but is driven by $\langle dN_{ch}/d\eta \rangle$. This is an important recent discovery. Hence strangeness enhancement has become a prominent and well-tested indicator of QGP formation.

Chapter 2

Theoretical framework of quarkonia suppression

In this chapter, the prerequisites for the bottomonium suppression study are explained. Firstly, the effective theory of quarkonium in QGP, the energy scales relevant to this system, and the corresponding degrees of freedom are described. This is followed by the theoretical framework of medium effects that influence quarkonium production in QGP, which are color screening, gluonic dissociation, and collisional damping. The non-QGP effect of shadowing is also explained.

2.1 Quarkonia effective theory: potential non-relativistic QCD (pNRQCD)

While describing a lot of physical phenomena, we encounter different energy/ momentum scales often differing by orders of magnitude, e.g. in hydrogen atoms, these scales are proton mass (in MeV), electron mass (in KeV), and binding energy (in eV). The idea behind constructing an effective field theory (EFT) is to build a suitable approximation of the full theory, which works well only at a given energy/momentum scale, assuming that the physics at one scale is not sensitive to the details of the dynamics at the other. Effectively, we can eliminate the contribution of very large or very small scales from consideration to a specific scale of interest by sending it to infinity or zero, respectively. Furthermore, by considering subsequent terms in the expansion in the ratio of small to large scale, the range of accuracy of the theory can be systematically improved. This concept of EFT was first introduced in the context of chiral dynamics by Weinberg [57]. For a detailed review on heavy quark EFT, we refer to [58–60]. For bound states involving at least one heavy quark, we need a non-relativistic (NR)EFT from QCD, where heavy quark mass will play the role of a large energy scale that needs to be integrated out. Some examples of such EFT are Heavy Quark Effective Theory [61, 62] for heavy-light bound states and Non-Relativistic QCD (NRQCD) [63–65] for heavy quarkonia states. Typical scales associated with bound states are mass (m) of quark, momentum (mv), and binding energy (mv^2), where v is the quark's relative velocity. And for non-relativistic system ($v << 1$), these scales follow the hierarchy, $m >> mv >> mv^2$. These scales are referred to as **hard** (m), **soft** (mv) and **ultrasoft** (mv^2). To consider suppression of quarkonia in a hot medium, we could narrow down our focus to only the ultrasoft scale of binding energy by integrating out the soft scale from NRQCD, which reduces it to another EFT called potential NRQCD (pNRQCD).

There is an intrinsic scale in QCD, Λ_{QCD}, which is the only dimensionful parameter of pure QCD. QCD scale is different for the number of flavors into consideration.At energy scales, $E \gg \Lambda_{\text{QCD}}$ only, we have an acceptable perturbative expansion. We need to consider the position of Λ_{QCD} scale with respective to ultrasoft scale. We will assume for heavy quark, $m \gg \Lambda_{\text{QCD}}$. From NRQCD, integrating out the degrees of freedom associated with the soft scale ($|\vec{p}| = mv$) requires us to have $|\vec{p}\,| \gg \Lambda_{\text{QCD}}$. Furthermore, if we have $|\vec{p}\,| \gg E \gtrsim \Lambda_{\text{QCD}}$, then we have a weakly coupled pNRQCD. The degrees of freedom at which pNRQCD operates are ultrasoft gluons, heavy quark color singlet, and color octet states. It turns out that the color singlet potential is attractive. Hence it could exist either as an unbound or bound state. Whereas the color octet potential is repulsive, hence the transition of color singlet state to color octet state could in inferred as dissociation of quarkonium.

Table 2.1: Energy scales relevant for the dynamics quarkonium in QGP medium.

QCD scale	Λ_{QCD}
hard scale	m
soft scale	$mv \sim \langle 1/r \rangle$
ultra soft scale	$E \sim mv^2$
Debye mass	m_D
temperature	T

The pNRQCD action is given as [66] :

$$S_{\text{pNRQCD}} = S_A + \int d\tau d^3r d^3R \Bigg[O^{a\dagger}(D_\tau + H_8)O^a + S^\dagger(\partial_\tau + H_1)S \\ + \frac{g}{\sqrt{2N_c}} \vec{r}\vec{E}^a(S^\dagger O^a + O^{a\dagger}S) + \frac{g}{2}\vec{r}\vec{E}^a O^{b\dagger} O^c d^{abc} \Bigg]. \tag{2.1}$$

Here,
S_A is the gauge sector part of the QCD action,
S and O are the singlet and octet fields,
$\vec{E^a}$ is the chromoelectric field,
$\vec{r}$ and $\vec{R}$ are the relative motion and center of mass coordinates,
d^{abc} is the symmetric structure constants in the anti-commutation relation of the generators infinitesimal SU(N_c) group:

$$\{T^a, T^b\} = \frac{\delta^{ab}}{N_c} + d^{abc}T^c, \tag{2.2}$$

where H_1 and H_8 are the singlet and octet Hamiltonians, respectively.

2.2 Quarkonium potential

Using Hard Thermal Loop resumed perturbation theory, Mikko Laine *et al.* [67] derived a static potential between heavy quark and heavy anti-quark at finite temperature in Minkowski time as,

$$\boxed{\begin{aligned} V(r,m_D) = {} & \frac{\sigma}{m_D}(1-e^{-m_D r}) - \alpha_{\text{eff}}\left(m_D + \frac{e^{-m_D r}}{r}\right) \\ & -i\alpha_{\text{eff}}T\int_0^\infty \frac{dz\,2z}{(1+z^2)^2}\left(1-\frac{sin(m_D r z)}{m_D r z}\right), \end{aligned} \qquad (2.3)}$$

where
$\alpha_{\text{eff}} = 4\alpha_s^S/3$,
r is the separation between heavy quark and heavy anti-quark,
σ is the string tension, whose value is 0.192 GeV^2
m_D is the Debye mass of the thermal medium found perturbation theory in the hard thermal loop approximation as:

$$m_D = T\sqrt{4\pi\alpha_s^T\left(\frac{N_c}{3}+\frac{N_f}{6}\right)}$$

here, $N_c = 3$ and $N_f = 3$ are the number of color charges and the number of flavors, respectively, $\alpha_s^T = \alpha_s(2\pi T)$ is the hard scale coupling constant. This potential is valid in the regime T$\gg 1/r \gtrsim m_D$ [68].

2.3 Hot matter effects

In this section, we look at the hot matter effects, which are the mechanisms assisting the dissociation of quarkonium in the QGP medium. It is due to these effects that the suppression in quarkonia is expected in heavy ion collisions. These effects must be accounted for while calculating the yield of the quarkonia resonances at the freezeout. The effects we are considering are color screening, collisional damping, and gluonic dissociation.

2.3.1 Gluonic dissociation

In the pNRQCD action (2.1), the ultrasoft scale processes are given by the interaction terms, which are given by the dipole interaction at the lowest order as

$$\frac{g}{\sqrt{2N_c}}\vec{r}\vec{E^a}(S^\dagger O^a + O^{a\dagger}S). \qquad (2.4)$$

This term describes a color singlet state of $b\bar{b}$ transitioning to a color octet state through interaction with an ultrasoft gluon. The color octet potential is repulsive.

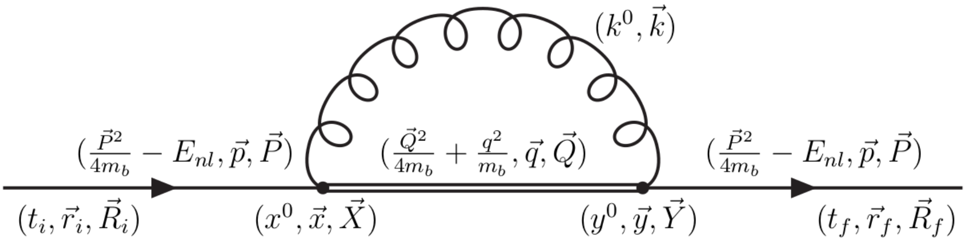
$(k^0, \vec{k})$
$(\frac{\vec{P}^2}{4m_b} - E_{nl}, \vec{p}, \vec{P})$
$(\frac{\vec{Q}^2}{4m_b} + \frac{q^2}{m_b}, \vec{q}, \vec{Q})$
$(\frac{\vec{P}^2}{4m_b} - E_{nl}, \vec{p}, \vec{P})$
$(t_i, \vec{r}_i, \vec{R}_i)$
$(x^0, \vec{x}, \vec{X})$
$(y^0, \vec{y}, \vec{Y})$
$(t_f, \vec{r}_f, \vec{R}_f)$

Figure 2.1: Self-energy diagram of a heavy quarkonium. The single and double lines are the representatives of the color singlet and doublet propagators. The singlet state on the right emits an ultrasoft gluon (curly lines) and transitions into a color doublet state at the chromoelectric dipole vertex (dot), which then transitions back after reabsorbing the same soft gluon. In the case of the quarkonium in QGP, the soft gluon is facilitated by the plasma medium. Image source [66].

Hence this process corresponds to the dissociation of $b\bar{b}$. In the position space singlet and octet fields propagators are given as

$$\begin{aligned} S_{fi} &= R_{fi} S^r_{fi}, \\ O^{ab}_{fi} &= \delta^{ab} R_{fi} O^r_{fi}, \end{aligned} \tag{2.5}$$

where R_{fi} is the center of mass frame (CM) propagator and S^r_{fi}, O^r_{fi} are relative motion coordinate frame (RM) propagators, describing propagation from $\vec{x}_{b,i}$, $\vec{x}_{\bar{b},i}$ at time t_i to $\vec{x}_{b,f}$, $\vec{x}_{\bar{b},f}$ respectively at time t_f.

The CM coordinates are introduced as follows:

$$\vec{R}_f = \frac{1}{2}(\vec{x}_{b,f} + \vec{x}_{\bar{b},f}) \qquad ; \qquad \vec{R}_i = \frac{1}{2}(\vec{x}_{b,i} + \vec{x}_{\bar{b},i}), \tag{2.6}$$

and the RM coordinates are introduced as:

$$\vec{r}_f = \vec{x}_{b,f} - \vec{x}_{\bar{b},f} \qquad ; \qquad \vec{r}_f = \vec{x}_{b,i} - \vec{x}_{\bar{b},i}, \tag{2.7}$$

Now, the CM propagator can be expressed as

$$R_{fi} = \int \frac{d^3Q}{(2\pi)^3} \; e^{iQ(\vec{R}_f - \vec{R}_i) - i\frac{\vec{Q}^2 t}{4m_b}}, \tag{2.8}$$

where, $t = t_f - t_i$. The CM propagator in the infinite mass limit approaches a δ-function,

$$R_{fi} = \longrightarrow \delta^3(\vec{R}_f - \vec{R}_i) \qquad \text{provided} \qquad m_b \to \infty \tag{2.9}$$

The RM propagator for singlet and octet states in terms of Schrödinger wave function are given respectively as [66]:

$$S^r_{fi} = \sum_{n=l}^{\infty}\sum_{l=0}^{n-1}\sum_{m=-l}^{l} \psi_{nlm}(\vec{r}_f)\psi^*_{nlm}(\vec{r}_i)e^{-iE_{nl}t} + \text{continuum states}, \tag{2.10}$$

$$O^r_{fi} = \sum_{l=0}^{\infty}\sum_{m=-l}^{l}\int_0^{\infty} dq\; \chi_{qlm}\;(\vec{r}_f)\;\chi^*_{qlm}\;(\vec{r}_i)\; e^{-i\frac{q^2 t}{m_b}}. \tag{2.11}$$

We now make an ansatz that for the octet state, the wavefunction can be factorized into the angular part and radial part as

$$\chi_{ql}(\vec{r}) = \frac{h_{ql}(r)}{r}\; Y_{lm}(\phi,\theta), \tag{2.12}$$

For these wave functions, we consider normalization using the following completeness relation,

$$\sum_{l=0}^{\infty}\sum_{m=-l}^{l}\int_0^{\infty} dq\; \chi^*_{qlm}(\vec{r'})\chi_{qlm}(\vec{r}) = \delta^3(\vec{r}-\vec{r'}). \tag{2.13}$$

The correction in the singlet propagator up to the first order in g^2 is due to due the singlet-octet dipole vertex term as given by

$$\begin{aligned} S^{1-8}_{fi} &= -\frac{ig^2}{2N_c}\int_{t_i}^{t_f} dx^0 dy^0 \int d^3x\; d^3y S^r_{fy} y^i \delta^{ab} O^r_{yx} x^j S^r_{xi}, \\ &\cdot \int d^3Y\; d^3X\; R_{fy}\Big(\partial_{x^0}\partial_{y^0}\Delta^{ab}_{ij}(y^0-x^0,\vec{Y}-\vec{X})\Big)R_{yx}R_{xi}, \end{aligned} \tag{2.14}$$

where g is calculated at the ultra soft energy scale and $\Delta^{ab}_{ij}(y^0-x^0,\vec{Y}-\vec{X})$ is the ultra soft gluon propagator given as

$$\Delta^{ab}_{ij}(x) = i\delta^{ab}\delta_{ij}\int dk\widetilde{dk}\Big(\Theta(-x^0)e^{-ikx} + \Theta(x^0)e^{ikx}\Big), \tag{2.15}$$

with $dk\widetilde{dk} = d^3k/(2\pi)^3/(2|\vec{k}|)$. For calculating the gluonic dissociation cross section, we first find the contribution of self-energy, Σ, because of the singlet to octet transition as

$$-i\Sigma_{nlm}(\vec{P})Vt\; e^{-i(\frac{\vec{P}^2}{4m_b}+E_{nl})t} = \int d^3r_f d^3R_f d^3r_i d^3R_i e^{-i\vec{P}\vec{R}_f}\psi^*_{nlm}(\vec{r}_f)S^{1-8}_{fi}\psi_{nlm}(\vec{r}_i)e^{i\vec{P}\vec{R}_i}. \tag{2.16}$$

Using $\delta^3(0) = V$ and doing spacial part integration, we get

$$\Sigma_{nlm} = \frac{iC_F g^2}{t} \sum_{l'=0}^{\infty} \sum_{m'=-l'}^{l'} \int_{t_i}^{t_f} dy^0 \int_{t_i}^{y^0} dx^0 \int d^3Q \; dq \; dk\widetilde{dk} \; \vec{k}^2 |\langle nlm|\hat{\vec{r}}|ql'm'\rangle|^2 \tag{2.17}$$

$$\cdot \; \delta^3(\vec{k} + \vec{Q} - \vec{P})(e^{i\Sigma_E^{+}(y^0 - x^0)} + e^{i\Sigma_E^{-}(y^0 - x^0)}), \tag{2.18}$$

where,

$$\Sigma_E^{\pm} = \frac{\vec{P}^2 - \vec{Q}^2}{4m_b} \pm |k| + E_{nl} - \frac{q^2}{m_b}. \tag{2.19}$$

As t → ∞,

$$\Sigma_{nlm} = iC_F g^2 \sum_{l'=0}^{\infty} \sum_{m'=-l'}^{l'} \int dq \; dk\widetilde{dk} \; \vec{k}^2 |\langle nlm|\hat{\vec{r}}|ql'm'\rangle|^2 \left(\frac{i}{\Sigma_E^{+} + i0^{+}} - \frac{i}{\Sigma_E^{-} - i0^{+}} \right), \tag{2.20}$$

where $\vec{P} = \vec{Q} + \vec{k}$. For the singlet to octet transition as shown in Fig. (2.1) and given as process $b\bar{b}_1 \rightarrow b\bar{b}_8 + g$. The width Γ_{diss} for this process in the rest frame of singlet state $b\bar{b}_1$ is given as

$$\Gamma_{\text{diss},nl} = \frac{1}{2l+1} \sum_{m=-l}^{l} 2 \; Im(\Sigma) \tag{2.21}$$

$$\Gamma_{\text{diss},nl} = \frac{2\pi C_F g^2}{2l+1} \sum_{m=-l}^{l} \sum_{l'=0}^{\infty} \sum_{m'=-l'}^{l'} \int dq \; dk\widetilde{dk} \; \vec{k}^2 |\langle nlm|\hat{\vec{r}}|ql'm'\rangle|^2 \delta(\Sigma_E^{-}). \tag{2.22}$$

Looking at Σ_E^{-} in the rest frame of singlet, where $\vec{P} = 0$, we notice that the δ-function in Eq. (2.19) leads to

$$\Sigma_E^{-} = |\vec{k}| - \frac{\vec{k}^2}{4m_b} + E_{nl} - \frac{q^2}{m_b} \approx |\vec{k}| + E_{nl} - \frac{q^2}{m_b}. \tag{2.23}$$

This approximation holds as $|\vec{k}| \sim m_b g^4$ for the ultrasoft gluons. The relation between width, Γ_{diss} and cross section is given by

$$\Gamma_{\text{diss},nl} = (N_c^2 - 1) N_c \int \frac{d^3k}{(2\pi)^3} \sigma_{diss,nl}(E_g), \tag{2.24}$$

with $E_g = |\vec{k}|$. The factor $(N_c^2 - 1)N_c$ comes from adding the various outgoing

gluon species and the octet state colors.
Inverting the above equation and using the Eq. (2.22), we the cross section as

$$\sigma_{diss,nl}(E_g) = \frac{2\pi^2\alpha_{nl}E_g}{(2l+1)N_c^2}\sum_{m=-l}^{l}\sum_{l'=0}^{\infty}\sum_{m'=-l'}^{l'}\int_0^\infty dq|\langle nlm|\hat{\vec{r}}|ql'm'\rangle|^2\delta\Big(E_g+E_{nl}-\frac{q^2}{m_b}\Big). \tag{2.25}$$

Rewriting this equation as:

$$\sigma_{diss,nl}(E_g) = \frac{\pi^2\alpha_{nl}E_g}{N_c^2}\sqrt{\frac{m_b}{E_g+E_{nl}}}\sum_{l',m',m}\frac{|\vec{I}_{nlm}^{\,ql'm'}|^2}{2l+1}, \tag{2.26}$$

where,

$$\vec{I}_{nlm}^{\,ql'm'} = \int d^3x\psi_{nlm}^*(\vec{r})\vec{r}\chi_{ql'm'}(\vec{r}). \tag{2.27}$$

Evaluating the integral by inserting the spherical harmonics, the above equation then reduces to:

$$\boxed{\sigma_{diss,nl}(E_g) = \frac{\pi^2\alpha_{nl}E_g}{N_c^2}\sqrt{\frac{m_b}{E_g+E_{nl}}}\frac{(l+1)|J_{nl}^{q,l+1}|^2+l|J_{nl}^{q,l-1}|^2}{2l+1} \qquad (2.28)}$$

where,

$$J_{nl}^{q,l'} = \int_0^\infty dr\ r\ g_{nl}^*(r)\ h_{qi'}(r). \tag{2.29}$$

These results for cross-section and decay width are valid at zero temperature. To calculate finite temperature decay from these expressions, we need a gluon distribution function as a weight for gluonic dissociation cross-section, for which we use the Bose-Einstein distribution,

$$\boxed{\Gamma_{\mathrm{diss},nl}(T) = \frac{g_d}{2\pi^2}\int_0^\infty\frac{dE_g\ E_g^2\ \sigma_{diss,nl}(E_g)}{e^{E_g/T}-1}, \qquad (2.30)}$$

where, g_d is the degrees of freedom of gluons.

2.3.2 Collisional damping

At finite temperature, the $b\bar{b}$ bound state will experience scattering with medium constituents, which could contribute to the dissociation width of the quarkonium.

The dissociation due to this phenomenon is referred to as *collisional dmping*. The imaginary part of the complex heavy quark anti-quark potential V_{nl} is responsible for this effect. The dissociation width corresponding to collisional damping [69] is calculated by taking the expectation value of the imaginary part of the complex potential as:

$$\boxed{\Gamma_{\text{damp},nl} = \int g_{nl}(r)^{\dagger}\,\text{Im}(V)\,g_{nl}(r)\,dr, \qquad (2.31)}$$

where, $g_{nl}(r)$ is the singlet wavefunction of the bottomonium.

2.3.3 Color screening

Consider two electromagnetic charges placed at a distance r apart in vacuum with the coulomb's potential $(-1/r)$ governing the force between them. If now the same system is placed in vacuum, the potential between charges assumes *Yukawa form* $(-e^{-m_E r}/r)$, where the parameter m_E is called the electric or Debye mass. Both of these potential forms are depicted in Fig. (2.2)(left), showing shortening of potential range between the opposite charges when placed in plasma when compared to the vacuum case. This phenomenon is termed as *Debye screening*. An analogous effect also exists for color charges in QGP and the corresponding effect is called *color screening*.

Eq. (1.17) is the empirical relation for the potential between quark and anti-quark. It has a coulombic part that dominates at small r and a linear part that dictates the large r behavior as shown in Fig. (2.2)(right) with the grey and black curve for the zero temperature. If system temperature is increased, the potential strength decreases and at large r, potential goes flat. This signifies that a colored bound state with a certain binding energy would be set free once the temperature is increased above a certain value where the potential for that bound state goes flat.

After being produced in hard scattering, the heavy quarks ($q\bar{q}$) traverse through QGP, where the range of their potential is shortened due to color screening in the plasma. A drifting quark anti-quark pair will form a bound state below a specific medium temperature. One possibility is that due to the color screening effect, the heavy quark anti-quark pair will drift apart from each other enough to not form a quarkonium but, instead, a heavy-light bound state. This is one of the potential

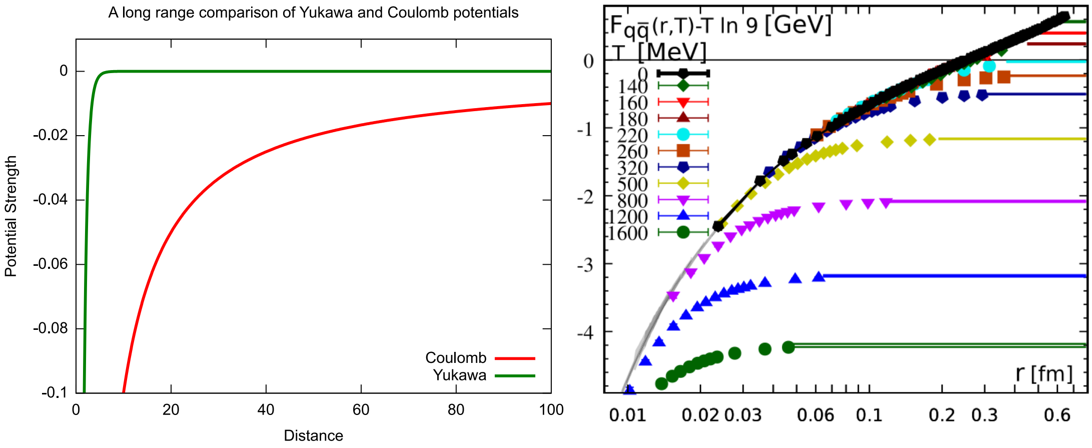

Figure 2.2: (Left) Comparison of Coulomb and Yukawa potentials. Image source [70]. (Right) The plot of free energy of quark anti-quark pair, $F_{q\bar{q}} - T\ ln\ 9$ in the continuum limit, which is a quantity analogous to the potential between quark and anti-quark pair with appropriate normalization convention. Image source [71].

causes of the reduced production of quarkonia. This quarkonia suppression due to color screening was first proposed by Matsui and Satz in 1986 [72].

Consider the expanding fireball right after the collision, for which, at the moment, the largest temperature will lie at its center with surfaces of reducing temperatures as we move away from the center. And these temperatures reduce as the fireball evolves. Now consider production of a heavy quark pair, $q\bar{q}$ at time $t = 0$ at a location (r_Q, ϕ_Q) at mid-rapidity plane $(\eta = 0)$ with energy, $E_Q = \sqrt{m_Q^2 + p_Q^2}$ and velocity, $\vec{v}_Q = \vec{p_Q}/E_Q$. Let's say the heavy quark pair forms quarkonia in time $t_F = \gamma_Q \tau_F$, where τ_F is the proper formation time and $\gamma_Q = E_Q/m_Q$ is the Lorentz factor. The quarkonia are unlikely to form in the region where the medium temperature of greater than its dissociation temperature due to color screening. The survival of quarkonia is more probable if it forms outside the surface of the dissociation temperature of that particular quarkonia species. This condition can be implemented with the condition $|\vec{r}_Q + \vec{v}_Q t_F| \geq r_s$, where r_s is the radius of dissociation temperature surface is approximated to be a sphere. On simplification, this above condition takes the following form:

$$cos(\phi) \geq A, \qquad \text{where,} \qquad A = \frac{(r_s^2 - r^2)m_Q - \tau_F^2\ p_T^2/m_Q}{2\ r\ \tau_F\ p_T}. \tag{2.32}$$

Consider a radial probability distribution for the production of $q\bar{q}$ pair in hard scattering collisions at r as:

$$f(r) = \left(1 - \frac{r^2}{\mathrm{R_T^2}}\right)\theta(\mathrm{R_T} - r), \tag{2.33}$$

where R_T is the maximum fireball radius for a given collision setting.
The net survival probability due to color screening becomes:

$$\boxed{S(p_T) = \frac{\int_0^{R_T} r\, f(r)\, dr \int_{\phi_{-max}}^{\phi_{max}} d\phi}{2\pi \int_0^{R_T} r\, f(r)\, dr} \tag{2.34}}$$

2.4 Cold nuclear matter effects

For calculating the nuclear modification factor (R_{AA}), which is an experimental observable used to infer suppression, we make a comparison of yields of *nucleus-nucleus* collisions with scaled up *proton-proton* collisions. In the previous section, we looked at the effects responsible for the dissociation of quarkonia due to the presence of the QGP medium. In *proton-nucleus* collisions, there are mechanisms that result in reduced production of quarkonia as compared to *proton-proton* collision. Moreover, we expect these effects also to be present in *nucleus-nucleus* collisions. These mechanisms are termed as *cold nuclear matter* (CNM) effects and should be accounted for as they do not necessarily signify the formation of a hot quark-gluon medium. In this section, among many such effects, we look at nuclear shadowing. It is predicted [73] that due to nuclear shadowing accounts for suppressed production of charmonium (J/ψ) and bottomonium (Υ) by a factor of 20% and 10% respectively when evaluated for pPb collisions at the collisional energy of 5 TeV.

2.4.1 Nuclear shadowing

Parton Distribution Functions (PDFs) $F_i^{p\in A}(x, Q^2)$ are the momentum distribution functions of the partons within a free nucleon. The nuclear Parton Distribution Functions (nPDFs) $F_i^p(x, Q^2)$ of a nucleon in the nucleus measured in Deep Inelastic Scattering (DIS) experiments were found to be quite different from the PDFs of a free nucleon, suggesting the presence of a nuclear effects [75, 76]. Furthermore, the factorization theorem in perturbative QCD facilitates the calculation

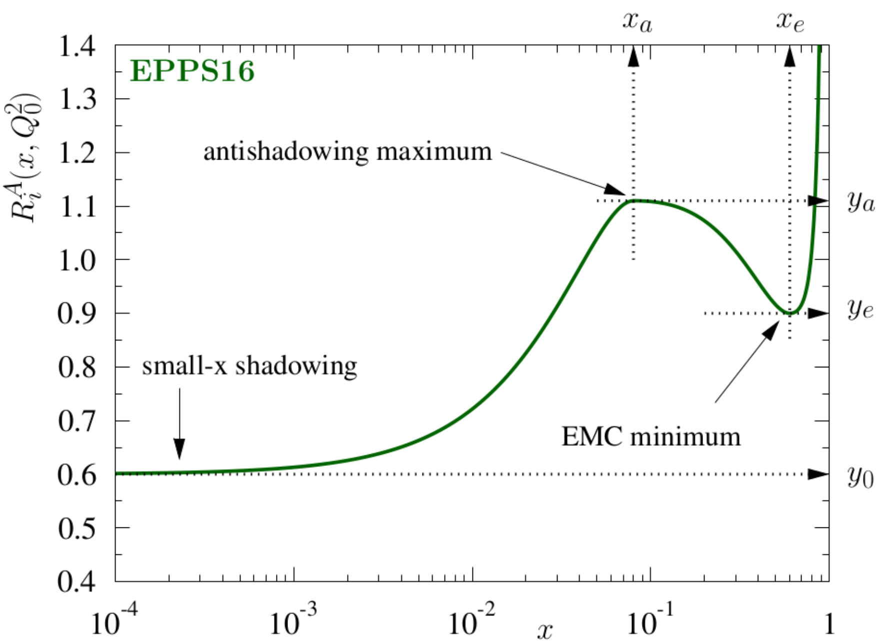

Figure 2.3: The ratio of nuclear parton distribution function to free parton distribution function ($R_i^A = F_i^{p\in A}(x,Q^2)/F_i^p(x,Q^2)$) is plotted on the y-axis, as a function of the Bjorken x variable on the x-axis. Bjorken x represents the fraction of hadron momentum that parton caries. The smaller than unity feature of R_i^A is called small-x shadowing, responsible for nuclear shadowing effect. Image source [74].

of hard scattering cross section using PDFs. This means that the quarkonia production cross-section is related to PDFs of colliding species of particles. The cross sections in DIS and fixed nuclear-target Drell–Yan (DY) process can be consistently obtained for these nuclear effects by considering the modification of PDFs for free partons and allowing Dokshitzer–Gribov–Lipatov–Altarelli–Parisi (DGLAP) equation to carry out Q^2 dependence [77–79]. The DGLAP or GLAP equations of QCD describe the evolution of parton distribution functions for variation in energy scales. The sets of global fits of these nPDFs measured in experiments have been released, the most recent one of which is EPPS16 [80]. EPPS16 is the set of next-to-leading order (NLO) nuclear PDFs obtained at high collisional energies for charged-lepton, proton, and deuteron, collisions with the nucleus. These EPPS16 nPDF sets are used in our model as shadowing factors as a function of atomic mass number A, Bjorken scaling x, and virtuality, Q^2. Shadowing factors parametrizes the modifications of the nucleon parton density distributions in the nucleus. In our model, we need to calculate the shadowing effect as a function of centrality or impact parameter using the method given in Ref. [81], where the authors calculated shadowing along the path traversed by parton inside the nucleus by assuming shadowing being proportional to local Woods-Saxon nuclear density $\rho_A(\vec{r}, z)$ as:

$$S^i(\vec{r}, x, A, Q^2, z) = 1 + N_\rho[S^i(x, A, Q^2) - 1]\frac{\int dz\ \rho_A(\vec{r}, z)}{\int dz\ \rho_A(0, z)}, \tag{2.35}$$

where ρ is the woods-Saxon distribution which is taken as an approximation for nuclear density distribution. $\rho_A(0, z)$ is the density at the center of the nucleus. And the normalization N_ρ is selected such that above form of $S^i(x, A, Q^2, \vec{r}, z)$ satisfies the following condition:

$$\frac{1}{A}\int d^2r dz \rho_A(s) S^i_\rho(x, A, \mu, \vec{r}, z) = S^i(x, A, \mu), \tag{2.36}$$

where $s = \sqrt{r^2 + z^2}$. The production cross section for quarkonia in *proton-proton* collision is given using color evaporation model [82] as:

$$\sigma_{pp} = \int dx_1 dx_2 f_g(x_1, A, Q^2) f_g(x_2, B, Q^2) \sigma_{gg-Q\bar{Q}}(x_1, x_2, Q^2), \tag{2.37}$$

where $f_g(x_1, A, Q^2)$ are the parton distribution function of protons obtained from CT14 [83] global analysis of experimental data. The production cross-section of quarkonia in the *nucleus-nucleus* collision is obtained using:

$$\sigma_{AB} = \int dz_1 dz_2 dr^2 dx_1 dx_2 f^i_g(x_1, A, Q^2, r, z_1) f^j_g(x_2, B, Q^2, b-r, z_2) \sigma_{gg-Q\bar{Q}}(x_1, x_2, Q^2). \tag{2.38}$$

Over the LHC's measurable rapidity range, gg (gluon-gluon) processes dominate quarkonium production. Hence the functions, f^i_g,f^j_g in the above equation are obtained in terms of shadowing factors and gluon PDFs in a proton as follows:

$$f^i_g(x_1, A, Q^2, r, z_1) = \rho_A(s) S^i_\rho(x_1, A, Q^2, r, z_1) f_g(x_1, Q^2), \tag{2.39}$$

$$f^j_g(x_2, B, Q^2, r, z_2) = \rho_B(s) S^j_\rho(x_2, B, Q^2, r, z_2) f_g(x_2, Q^2). \tag{2.40}$$

The shadowing correction to quarkonia production in AA collisions is calculated as:

$$\boxed{S_{sh}(b,p_T) = \frac{d\sigma_{AA}/dy}{T_{AB}(b)\sigma_{pp}/dy}, \qquad (2.41)}$$

where T_{AB} is the nuclear overlap function.

Chapter 3

Bottomonium suppression in Pb-Pb collisions at CERN LHC energies

3.1 Introduction and literature review

Quarkonia suppression is one of the prominant signatures of QGP formation in heavy-ion collisions. Quarkonia are the mesonic bound state of heavy quark and heavy anti-quark, which are produced in the early stage of collision. They could dissociate due to interaction with partons in the medium and would be detected lesser in number relative to collision systems where we do not expect QGP, like at low energies and in pp collisions [72]. In order to quantify this suppressed production of quarkonium, an observables called as nuclear modification factor(R_{AA}) is measured in experiments. It is the quarkonia yield in heavy-ion collision divided by the yield of the quarkonium in pp collision scaled by number of binary collisions, N_{coll}. Its value being less than one, greater than one and equal to one indicates suppression, enhancement and no medium effect, respectively. Surprisingly, there are effects which contribute to suppression but are not related to a thermalized medium. These non-QGP effects originates from the conditions before the collision and these should be accounted into the total suppression scheme [84]. These non-QGP effects are sometimes also referred to as the cold nuclear matter (CNM) effects. The R_{AA} is measured over a wide range of collision energies and for different colliding nuclei as a function of centrality, N_{part}, transverse momentum, p_T and rapidity, y.

To model quarkonia suppression theoretically from first principles is a daunting task given the bulk, transient and complex nature of the system. Contemporary studies resort to phenomenological models to qualitatively reproduce R_{AA} data. Sequential suppression of different species of heavy quark bound states could potentially act as thermometer of QGP [85]. Studies on heavy quark diffusion has helped shed some light on properties of QGP using various semiclassical approaches [86, 87]. Some progress has been made in the last decade to understand quarkonia dynamics in a thermal medium using open quantum system and pNRQCD [88–92]. Phenomenological models have been put forth to explain the measured values of quarkonia suppression for a wide range of beam center of mass energies and collision systems [93]. Few attempted explaining centrality and p_T dependencies of [94–96]. Moreover, even fewer predict all three dependencies (centrality, p_T and rapidity) of the suppression over a wide range of available center of mass energies [97, 98].

In the previous study published in [Eur. Phys. J C **79**, 147 (2019)], our group had explained the p_T and N_{part} dependence of R_{AA} over a range of LHC energies. It was based on the suppression due to color screening, gluonic dissociation, and collisional damping under $(1 + 1)$-dimensional Bjorken's expansion of the thermalized medium. The net quarkonium yield was determined using a rate equation that combines suppression and recombination due to correlated quark anti-quark pairs. In the current study, we start with the initially produced bottomonia yields, which evolve in $(3 + 1)$-dimensional hydrodynamic medium. This initial yield is influenced by a CNM effect used here called "Shadowing", which has been updated for the newly available parton distribution functions and shadowing factors. The bottomonium bound state, while drifting through QGP, could dissociate due to gluonic dissociation, collisional damping, and color screening, which are adapted to the $(3 + 1)$-dimensional hydrodynamic expansion. Color screening has been streamlined by eliminating the need of assuming a pressure profile of collision. A lattice QCD-based equation of state (EOS) from the Wuppertal-Budapest Collaboration has been utilized. The input parameters for the hydrodynamics are constrained using the transverse momenta and rapidity spectra for pions from the ALICE experiment. And lastly, after considering the possibility of recombination of correlated bottom quark and anti-quark pair, we find the final number of bottomonia for the ground state and excited states [99]. We then find a quantity called survival probability (S_p) which is theoretically equivalent to the experimentally measured R_{AA}. We determine this as a function of transverse momentum, centrality, and rapidity at 2.76 TeV and 5.02 TeV energies and then compare with the corresponding R_{AA} values for $\Upsilon(1S)$ and $\Upsilon(2S)$ states. On comparison, we find a reasonably well agreement between S_p and R_{AA} at two LHC energies.

The arrangement of the topics in this chapter is as follows. In Sec. (3.2), we briefly describe the $(3+1)$-dimensional hydrodynamics used to model the bulk of medium using ECHO-QGP, followed by the quarkonia suppression formalism with various effects incorporated explained in Sec. (3.2.2). Sec. (3.2.3) and Sec. (3.2.4) present the quarkonia recombination mechanism and final yield of quarkonia, respectively. And finally, in Sec. (3.3), we present the suppression results and discussion of two bottomonium states, Υ(1S) and Υ(2S).

3.2 Formalism

Here we describe formalism in brief. The suppression formalism, which has been developed in our previous work [100], has been adapted for the $(3+1)$-dimensional viscous hydrodynamics. More details about individual medium effects used can be found in [101–103].

3.2.1 (3+1)-dimensional hydrodynamical expansion of the medium

Hydrodynamics has been quite successful in explaining bulk observables from ultra-relativistic heavy-ion collisions for a wide range of systems and energies [104–107]. The agreement of hydrodynamical predictions with experimental results has been taken as indirect evidence for the correctness of dynamics. Bjorken's hydrodynamics assumes that the fireball expands only along the longitudinal direction and is restricted to the plateau region of rapidity spectra (dN/dy vs y). This leads to the key variables of dynamics, e.g. temperature, pressure, energy density, entropy density, to become an explicit function of proper time [108]. Thus, although models based on Bjorken's evolution are adequate to estimate the observables at midrapidity, yet they are ineffective in providing the complete spacetime evolution of the system. In order to simulate the true dynamics of a collision that holds up expansion along the transverse directions and larger rapidities, one has to switch to the complete $(3+1)$-dimensional hydrodynamics. ECHO-QGP is a FORTRAN-based code to find the solutions of the conservation equations, $d_\mu N^\mu = 0$ and $d_\mu T^{\mu\nu} = 0$, where d_μ is the covariant derivative, N^μ is the four current, and $T^{\mu\nu}$ is the energy-momentum tensor. To solve these equations numerically in (3+1)-dimensions with relativistic speeds and viscous conditions, Israel-Stewart's second-order formalism has been used in ECHO-QGP [109]. A Cooper-Frye prescription handles the freeze-out stage, where the produced particles are assigned their momenta at the constant temperature hypersurface. We vary the input parameters of the ECHO-QGP so that the particle momentum spectra calculated here to match with the measured spectra from experiments, as explained below. We mark the end of the QGP phase at the value of proper time when the maximum temperature of the system drops below the pseudo critical temperature, T_{pc}.

The equation of state (EOS) from Wuppertal-Budapest (WB) Collaboration [110] replaces the earlier quasiparticle EOS [111]. WB EOS is spline interpolation with the hadron Resonance Gas (HRG) EOS [112] for the hot and dense hadronic matter after hadronization. WB EOS computed from the lattice QCD is a better choice as the pseudo critical temperature range of QGP predicted by their analysis lies close to the presently agreed upon value [113]. We ran the hydrodynamics code for 11 values of the impact parameter covering the $0-100\%$ centrality range. We chose the geometric Glauber initialization in ECHO-QGP [114]. A rapidity profile of p$-$p collisions is also employed as an input. The two parameters characterizing this profile are Δ_s; which is the extension of the rapidity plateau, and σ_η; which is the width of the Gaussian fall-off of the profile. Values for both of these parameters are varied until the shape of pions (π^+) rapidity spectra matches with that from the experimental pions rapidity spectra for the two mentioned LHC energies as shown in Fig. (3.1) [115, 116]. The values of the relaxation time coefficient for the viscosity of second order, τ_π and the shear viscosity to entropy density ratio, η/s are taken from [117, 118]. The thermalization time in the code is set for both the energies viz. 2.76 TeV and 5.02 TeV at 0.20 fm/c [104, 117, 119]. The inelastic nucleon-nucleon cross-section is taken as to be 61.8 mb and 70 mb for 2.76 TeV and 5.02 TeV, respectively [114]. Lattice QCD predicts the formation of a thermalized

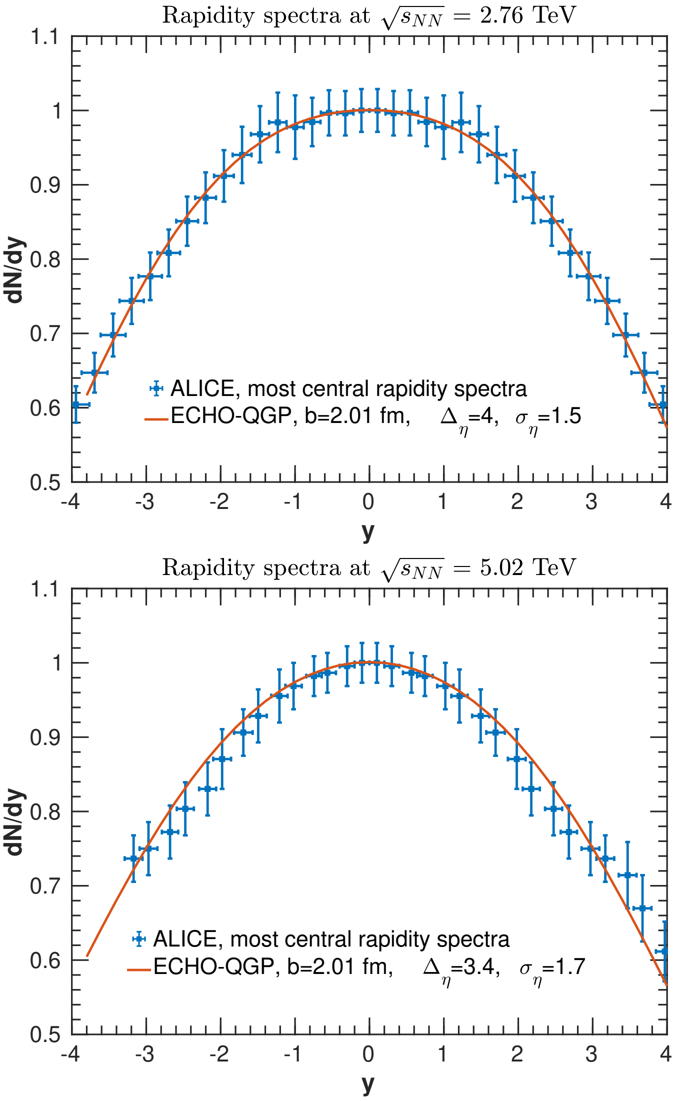

Figure 3.1: Pion(π^+) rapidity spectra for the two mentioned LHC energies from ALICE (symbols), normalized to their respective maxima for the most central collision (with impact parameter, b) compared with those obtained from ECHO-QGP (line).

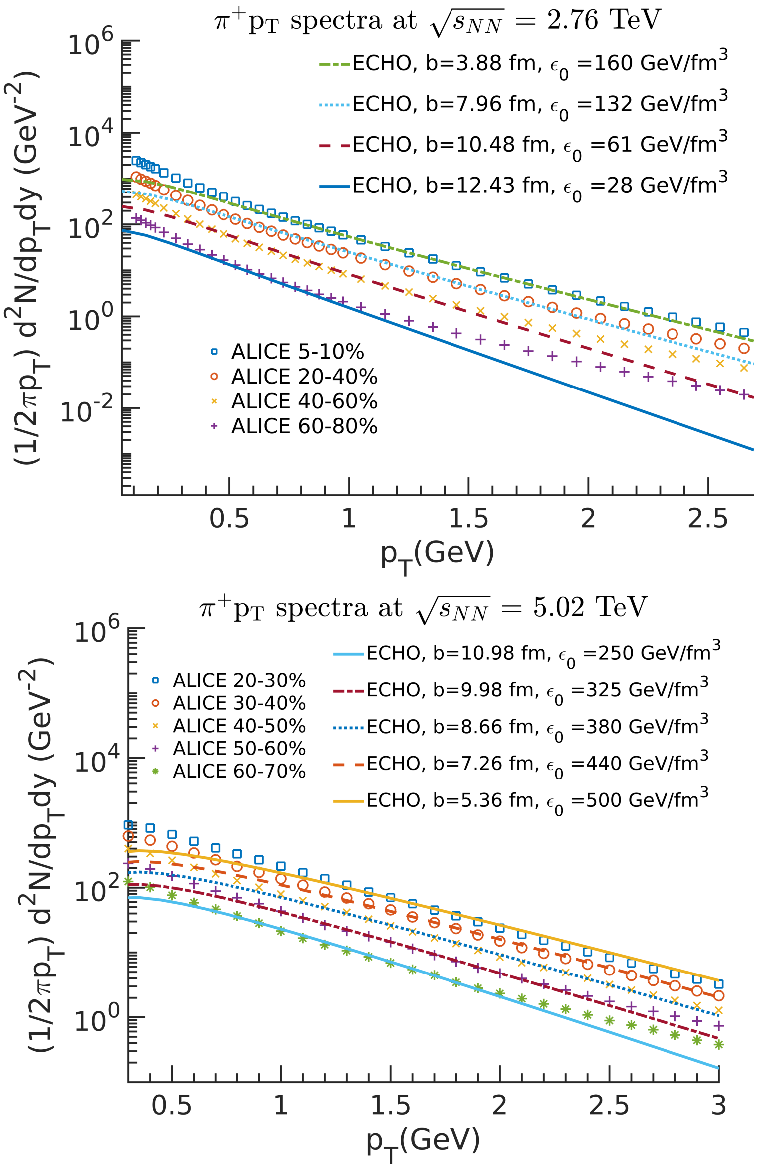

Figure 3.2: Pion(π^+) p_T spectra from experiments (symbols) compared with those obtained from ECHO-QGP (lines) for the mentioned LHC energies and centralities.

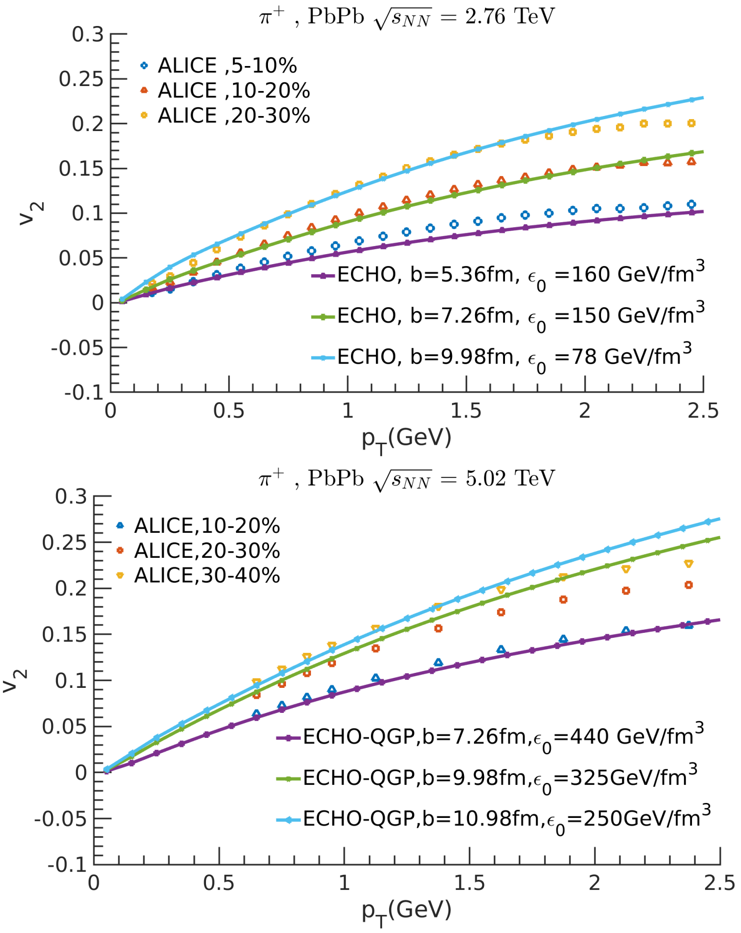

Figure 3.3: Pion(π^+) elliptic flow from experiments (symbols) compared with those obtained from ECHO-QGP (lines) for the mentioned LHC energies and centralities.

medium at energy density above 1.0 GeV/fm^3 [120]. Initial energy density, which goes as an input in ECHO-QGP, was at first calculated roughly using an approximate relation $\epsilon_0 = \frac{1}{A_T \tau_0} J(y,\eta) \frac{dE_T}{dy}$ involving overlap area, initial thermalization time and the differential transverse energy [108, 121]. However, the peak values of the pion p_T-spectra for these values fall shorter than the experimental values. Hence, we varied the initial energy density at each centrality such that the pions p_T-spectra from ECHO-QGP matches that from experiment values [122, 123]. The comparison of the pion spectra at a few of these centralities is shown in Fig. (5.3). The key parameters used in the ECHO-QGP hydrodynamics are summarized in Table (3.1).

Table 3.1: The Key parameters used as input in ECHO-QGP.

Parameters	**Values**	
Initialization	Geometric Glauber	
Equation of State	WB EoS spline interpolated with HRG	
Grid Size (fm)	$30 \times 30 \times 30$	
Grid points	$125 \times 125 \times 125$	
Relaxation time for viscosity, τ_π	3	
η/s	$0.1 \approx 1.25 \times (1/4\pi)$	
t_{start}(fm/c)	0.2	
	For 2.76 TeV	**For 5.02 TeV**
Extension of the rapidity plateau in p-p collision	4	3.4
Width of the gaussian falloff in pp collision, σ_η	1.5	1.7
σ_{NN}(mb)	61.8	70

The suppression formalism, described in the next section, requires the temperature of the medium at different centralities and rapidities as a function of proper time in the transverse plane, which are obtained from the ECHO-QGP. Calculation of suppression at all transverse (x,y) points is computationally infeasible. Hence, temperatures are integrated over the transverse plane at all centrality, rapidity, and proper time with a Gaussian weight factor and are taken as an input in the suppression formalism. The standard deviation of this Gaussian profile is varied within a specific range which is explained in the results and discussion section.

3.2.2 Suppression mechanisms

The bottom quark anti-quark pair produced in the hard scattering of colliding nuclei in the early stage of collision combines to form the bottomonia mesons. These heavy-flavor mesons will drift in the medium, and their decay products are eventually detected. During their time in the medium, these meson bound states are affected by various medium dependant dissociation mechanisms like color screening, collisional damping, and gluonic dissociation, which are individually explained below along with the possible recombination due to correlated $b - \bar{b}$ pairs and the non-medium effect of shadowing.

Gluonic dissociation

Gluonic dissociation is referred to as the process where a bottomonium color singlet state absorbs a soft gluon in the medium and gets excited to a color octet state. The cross-section for this process is calculated as [124];

$$\sigma_{\mathrm{diss},nl}(E_g) = \frac{\pi^2 \alpha_s^u E_g}{N_c^2} \sqrt{\frac{m_q}{E_g + E_{nl}}} \frac{(l+1)|J_{nl}^{q,l+1}|^2 + l|J_{nl}^{q,l-1}|^2}{2l+1}, \tag{3.1}$$

where, E_g is the soft gluon energy, E_{nl} is the eigenvalues corresponding to the bottomonium wavefunction ($g_{nl}(r)$), m_q is bottom quark mass in GeV, N_c is the number of color charges, $\alpha_s^u = \alpha_s(m_q \alpha_s^2/2) \approx 0.59$ and

$$J_{nl}^{q,l'} = \int_0^\infty r \; g_{nl}^*(r) \; h_{ql'}(r) \; dr, \tag{3.2}$$

where g_{nl}^* and $h_{ql'}(r)$ are the singlet and octet wavefunction of bottomonium, respectively, obtained after numerically solving the 3-dimensional Schrödinger's equation. We integrate the cross-section in Eq. (3) with Bose-Einstein distribution as weight factor over gluon momentum to calculate the dissociation width due to gluonic dissociation, i.e., $\Gamma_{\mathrm{gd},nl}$. The validity of the above cross-section assumes T$\ll 1/r$, where T is the medium temperature, and r is the distance between quark and antiquark[125]. This regime is different from the one for which collisional damping holds, due to which our final results for T$\ll 1/r$ may have less accuracy.

Collisional damping

We expect bottomonium to dissociate while it traverses through the plasma due to the *momentum transfer* arising out of the collision. To account for this effect, we use a potential non-relativistic QCD (pNRQCD) formalism which depends on the imaginary part of the color potential between quark anti-quark pairs. The complex potential between quark anti-quark pair located inside the QGP medium as determined by Laine et al., [67] using effective field theory, is given as,

$$\begin{aligned} V(r, m_D) = {} & \frac{\sigma}{m_D}(1 - e^{-m_D r}) - \alpha_{\mathrm{eff}} \left(m_D + \frac{e^{-m_D r}}{r} \right) \\ & - i \alpha_{\mathrm{eff}} T \int_0^\infty \frac{dz \; 2z}{(1+z^2)^2} \left(1 - \frac{sin(m_D r z)}{m_D r z} \right), \end{aligned} \tag{3.3}$$

where,

$\alpha_{\text{eff}} = 4\alpha_s^S/3$,
σ is the string tension, whose value is 0.192 GeV^2,
m_D is the Debye mass which is expressed as;

$$m_D = T\sqrt{4\pi\alpha_s^T\left(\tfrac{N_c}{3}+\tfrac{N_f}{6}\right)}.$$

Here, N_c and N_f are the number of color charges and number of flavors, respectively. This potential is valid in the regime T$\gg$ $1/r \gtrsim m_D$ [68]. We take the expectation value of the imaginary part of this potential to get the dissociation width corresponding to collisional damping [69] as,

$$\Gamma_{\text{damp},nl}(\tau, p_T, b) = \int g_{nl}(r)^\dagger \ \text{Im}(V)\ g_{nl}(r)\ dr, \tag{3.4}$$

where, $g_{nl}(r)$ is the singlet wavefunction of the bottomonium.

In our previous work [100], the explicit τ dependence of gluonic dissociation widths and collisional damping widths in Eq. (3.4) arose from the analytical expression for temperature, $T(\tau)$, obtained by solving Bjorken's dynamics. We have now replaced it with the tabulated temperature values from ECHO-QGP at each centrality and rapidity integrated over the transverse plane for each bottomonium state.

Color screening

Due to the presence of free color charges in QGP medium, the bottom quark and anti-quark (b and $\bar{b}$) experience a short-range Yukawa-type color charge potential dependent on the medium temperature. As a consequence of this, the formation of bound states in the medium is suppressed if the medium temperature goes beyond a certain temperature (dissociation temperature). This phenomenon is called the color screening [72] in an analogous way to the Debye charge screening in the quantum electrodynamics plasma. Different bottomonia species take different times, after the collision, to form the corresponding bottom anti-bottom bound states termed as their respective formation times(τ_f). Consider a screening region in the fireball as a sphere with a screening radius(r_s) defined for a bottomonium state depending on its dissociation temperature(T_D). Suppose a $b\bar{b}$ quark pair forms at the position $\vec{r}_Q$. Then it will likely form a bound state if it escapes the screening region in time equal to its formation time. The condition for which could be given by $|\vec{r}_Q + \vec{v}_T\tau_F| \geq r_s$, where $\vec{v}_T$ is the transverse drift velocity of the heavy quark in the medium. Here τ_F is the vacuum formation time of bottomonium.

Considering the transverse motion of this bottomonium state, we can simplify the above condition as;

$$cos(\phi) \geq Y \quad ;\text{where}, Y = \frac{[(r_s^2 - r_Q^2)m_Q - \tau_f p_T^2/m_Q]}{2r_Q \tau_f p_T}, \tag{3.5}$$

where, m_Q is the mass of the bottomonium state under consideration. Let us now consider a transverse radial distribution of $b\bar{b}$ produced after the hard scattering as:

$$h(r) = \left(1 - \frac{r^2}{\mathrm{R_T^2}}\right)\theta(\mathrm{R_T} - r). \tag{3.6}$$

The quantity $\mathrm{R_T}$ in the above equation is the maximum fireball radius obtained for different centralities from Modified Glauber analysis [126].

The color screening survival probability is given by:

$$S_{cs}(p_T) = \frac{4}{\pi R_T^2}\int_0^{R_T} dr\, r\, \phi_{max}(r)\left(1 - \frac{r^2}{\mathrm{R_T^2}}\right), \tag{3.7}$$

where $\phi_{max}(r)$ is the maximum positive azimuthal angle allowed by the condition in Eq. (3.5).

In our previous work [100], we equated an assumed pressure profile in the transverse plane with the cooling law to obtain the screening time (time to drop initial pressure to the pressure corresponding to the dissociation temperature). Screening time is then equated to the bound state formation time (at the boundary of the screening region) to obtain the screening radii [103]. Here we eliminated the need for this assumption of pressure profile in the transverse plane by directly finding the screening radii from the transverse temperature evolution using ECHO-QGP. We take the minimum radius of the oval-shaped contour shown in Fig. (3.4) as the screening radius at the evolution time equal to the formation time for a given bottomonium species. The temperature contours are marked for the dissociation temperature of all the bottomonium states at all centralities. The dissociation temperature (T_D) of different bottomonium states are borrowed from the analysis given in [127].

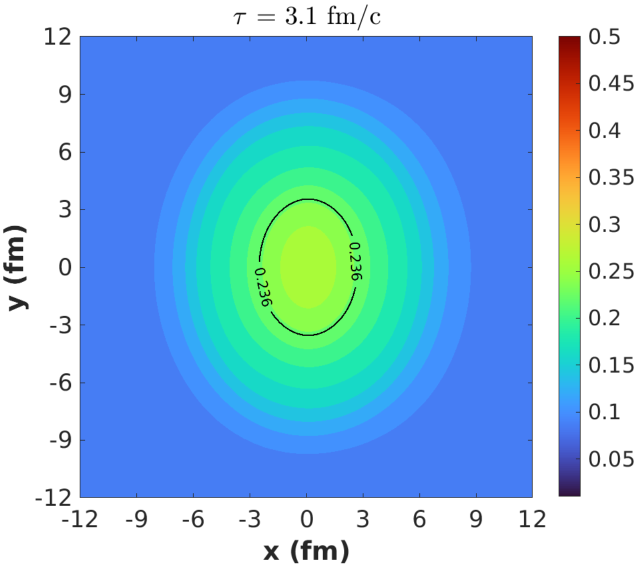

Figure 3.4: The transverse temperature profile for 2.76 TeV collisional energy in ECHO-QGP at $N_{part} = 130$, rapidity $= 1.44$ at $\tau = 3.1$ fm/c which is taken as the formation time of $\Upsilon(3S)$. The region inside the contour of $T_D = 236$ MeV for $\Upsilon(3S)$ state depicts the screening region. As it is not for the most central collision, the fireball cross section is oval-shaped.

CNM effect: Nuclear shadowing

The shadowing correction to R_{AA} applied in our formalism is a modified version of the similar work by R. Vogt [128]. We have replaced the shadowing factors used for gluons from EPS09 [129] to the more recent EPPS16 [130]. The central fit set is selected from various error sets in EPPS16. The parton distribution function of gluons has been updated to CT14 [131] from the earlier PDFs CTEQ6 [132]. The contribution of suppression arising due to the shadowing effect is expressed as [133]:

$$S_{sh}(p_T, b) = \frac{d\sigma_{AA}/dy}{T_{AA} d\sigma_{pp}/dy}. \tag{3.8}$$

The shadowing effect influences the number of initially produced bottomonia(N_Q). Hence, the shadowing corrected the initial number of bottomonium is calculated as $N_Q^i(\tau_0, b) = N_Q(\tau_0, b) S_{sh}(p_T, b)$.

3.2.3 Recombination mechanisms

We have incorporated the possibility of recombination of $b\bar{b}$ due to de-excitation from octet to singlet state with a gluon emission, even though it will be negligible for the case of bottomonium. We find the recombination cross-section in QGP using detailed balance from gluonic dissociation cross-section as [134]

$$\sigma_{f,nl} = \frac{48}{36}\sigma_{d,nl}\frac{(s - M_{nl}^2)^2}{s(s - 4m_q m_{\bar{q}})}, \tag{3.9}$$

where s is the Mandelstan variable, M_{nl}, m_q and $m_{\bar{q}}$ are the masses of bottomonia states, bottom quark, and bottom anti-quark, respectively. We then define a recombination factor as the thermal average of the product of the above cross-section and relative velocity between b and $\bar{b}$ as, $\Gamma_{F,nl} = \langle \sigma_{f,nl}\ v_{rel} \rangle_k$.

3.2.4 Final number of bottomonium

Due to all of the above effects, the bottomonia can dissociate, or the correlated $b\bar{b}$ pair can recombine again into bound states. We assume that this interplay of dissociation and recombination is governed by a simple first-order differential equation given as [135];

$$\frac{dN_Q(\tau)}{d\tau} = \frac{\Gamma_{F,nl} N_q N_{\bar{q}}}{V(\tau)} - \Gamma_{D,nl} N_Q, \tag{3.10}$$

where, N_Q is the bottomonia yield at a given value of proper time (τ). The first and second terms on the right hand side of this equation correspond to the recombination and dissociation terms, respectively. $\Gamma_{F,nl}$ and $\Gamma_{D,nl}$ are the corresponding recombination and dissociation rates. N_q and $N_{\bar{q}}$ are the number of heavy quark and anti-quark produced in p−p collision. $V(\tau)$ is the instantaneous volume of the expanding fireball.

The solution for the above first order differential equation under the approximation that $N_Q < N_q$,$N_{\bar{q}}$ is given by,

$$N_Q(\tau_{QGP}, p_T) = \epsilon(\tau_{QGP}, p_T)\left[N_Q(\tau_0) + N_q N_{\bar{q}} \int_{\tau_0}^{\tau_{QGP}} \frac{\Gamma_{F,nl}(\tau, p_T)}{V(\tau)\ \epsilon(\tau, p_T)} d\tau\right], \tag{3.11}$$

where τ_{QGP} is the QGP lifetime and τ_0 is the initial time at which we start hydrodynamics and which also marks the beginning of the QGP stage.

The first term inside the bracket on the right hand side in Eq. (2) is the bottomonia produced at the initial hard scattering stage. $N_Q(\tau_0)$ is calculated as [136]:

$$N_Q(\tau_0, b) = \sigma_Q^{NN} T_{AA}(b), \tag{3.12}$$

where σ_Q^{NN} is the production cross-section of the bottomonium at a given collisional energy. $T_{AA}(b)$ is the nuclear overlap function. $V(\tau)$ in Eq. (2) is volume of fireball given by the formula;

$$V(\tau) = \tau_0 \pi R_T^2 \left(\frac{\tau_0}{\tau}\right)^{\frac{1}{R}-1}, \tag{3.13}$$

where, R_T is the radius of colliding nuclei and R is the Reynold's number. $\epsilon(\tau, p_T)$ in Eq. (2) is a suppression factor integrated cumulatively in τ values and is given by:

$$\epsilon(\tau, p_T) = \exp\left(-\int_{\tau'_{nl}}^{\tau} \Gamma_{D,nl}(\tau', p_T) d\tau'\right). \tag{3.14}$$

Eq. (2) also has a multiplicative suppression factor, which is integrated for the complete QGP lifetime and is calculated as:

$$\epsilon(\tau_{QGP}, p_T) = exp\left(-\int_{\tau'_{nl}}^{\tau_{QGP}} \Gamma_{D,nl}(\tau, p_T) d\tau\right). \tag{3.15}$$

In the above equation, τ'_{nl} is the time required for the formation of a given bottomonium state within QGP.

We then calculate the ratio, $S'_p = N_Q/N_Q^i$ referred to as the survival probability. The color screening has been considered as an independent effect, and hence the total survival probability is calculated as $S_p = S'_p \times S_{cs}$. We find this survival probability for 5 bottomonia states which are $\Upsilon(1S)$, $\Upsilon(2S)$, $\chi_{b0}(1P)$, $\chi_{b0}(2P)$ and $\Upsilon(3S)$. A feed-down scheme dictates the total yield after all possible decays from higher excited states [101]. The Survival probability(S_p) obtained after feed down for $\Upsilon(1S)$ and $\Upsilon(2S)$ is plotted and compared with the respective R_{AA} obtained from experiments.

3.3 Results and discussions

Results have been generated for a centrality range of $0-100\%$, transverse momentum range of $1-30$ GeV/c, and rapidity range of $|y| < 3.6$, which covers the ranges of experimentally available data from CMS and ALICE at both 2.76 TeV and 5.02 TeV [137–140]. ALICE suppression data at forward rapidity complements well with the broader rapidity range of CMS data, especially for p_T and N_{part} dependence of $\Upsilon(2S)$ at $\sqrt{s_{NN}} = 5.02$ TeV. The standard deviation (σ_T) of the Gaussian weight factor used for integrating temperatures from ECHO-QGP,

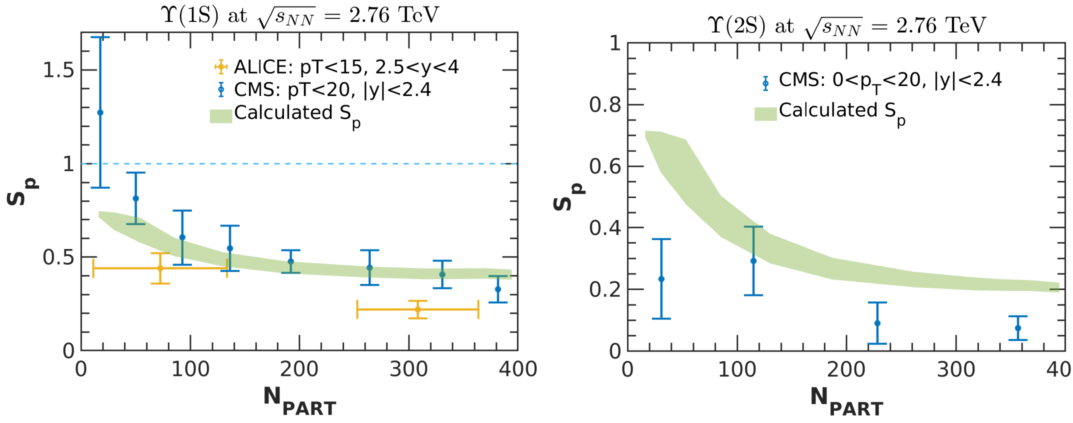

Figure 3.5: Centrality dependence of suppression for Υ compared with measured R_{AA} at $\sqrt{s_{NN}} = 2.76$ TeV.

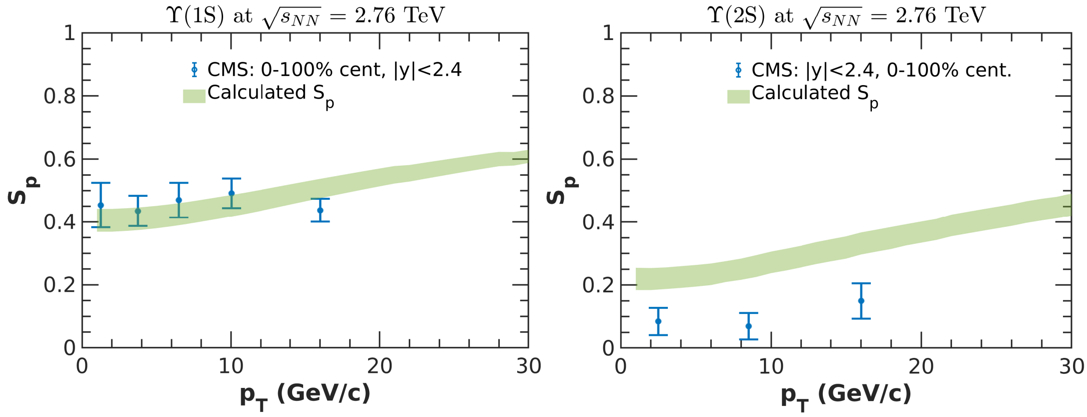

Figure 3.6: Transverse momentum dependence of suppression for Υ compared with measured R_{AA} at $\sqrt{s_{NN}} = 2.76$ TeV

as mentioned in Section (II-A) has been varied to obtain an uncertainty patch in the theoretically calculated suppression results as shown in the figures. For 2.76 TeV the standard deviation value lies between $0.7 < \sigma_T < 2.8$ and for 5.02 TeV, it spans as $1.4 < \sigma_T < 3.9$. Selecting σ_T greater than the upper limits for the two energies makes the QGP lifetime, in peripheral collisions at extreme rapidity values, smaller than the formation time of $\Upsilon(1S)$ and $\Upsilon(2S)$ states. Selecting σ_T smaller than the lower limits undermines the temperatures at large x-y values rendering the purpose of integration futile.

Fig. (3.5) depicts the centrality dependence of suppression for $\Upsilon(1S)$ and $\Upsilon(2S)$ states at 2.76 TeV as calculated by our present model. The corresponding experimental suppression data are shown for comparison. Our calculated values of the survival probability for $\Upsilon(1S)$ lie very close to the CMS data and follow the trend

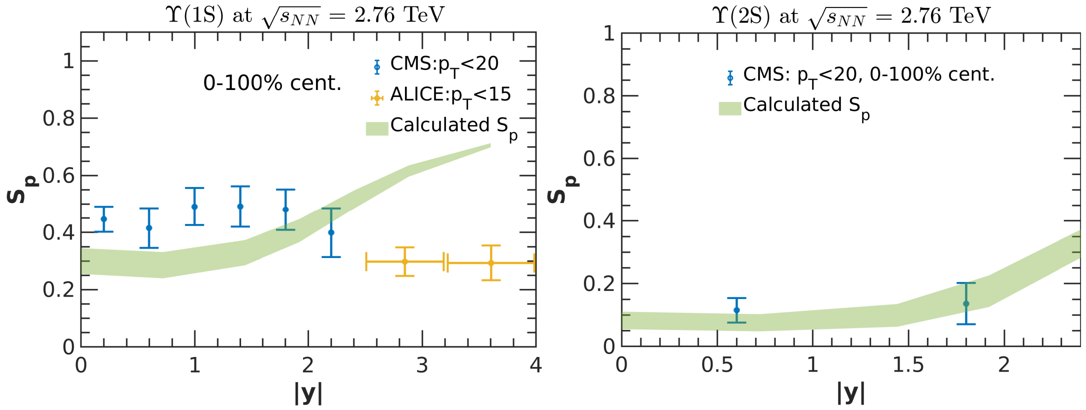

Figure 3.7: Rapidity dependence of suppression for Υ compared with R_{AA} at $\sqrt{s_{NN}}$ = 2.76 TeV.

of ALICE data. Whereas for $\Upsilon(2S)$, our predicted values are slightly less suppressed but mostly following the CMS data.

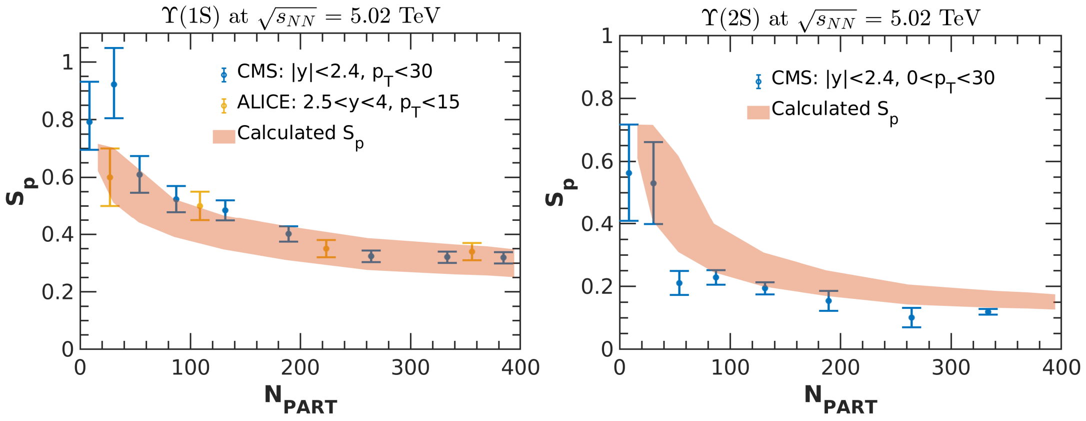

Figure 3.8: Centrality dependence of suppression for Υ compared with R_{AA} at $\sqrt{s_{NN}}$ = 5.02 TeV.

Fig. (3.6) shows the variation of our predicted values of suppression for $\Upsilon(1S)$ and $\Upsilon(2S)$ with respect to the transverse momentum at the 2.76 TeV center of mass energy. We find that the agreement among our calculated and measured values for $\Upsilon(1S)$ are reasonably well. However, for $\Upsilon(2S)$, calculated suppression is slightly lesser than the values from available data from CMS.

In Fig. (3.7), we have plotted our theoretical results of rapidity dependence of $\Upsilon(1S)$ and $\Upsilon(2S)$ suppression along with the corresponding experimental data. We find a quite reasonable agreement in the case of $\Upsilon(1S)$ then $\Upsilon(2S)$ within

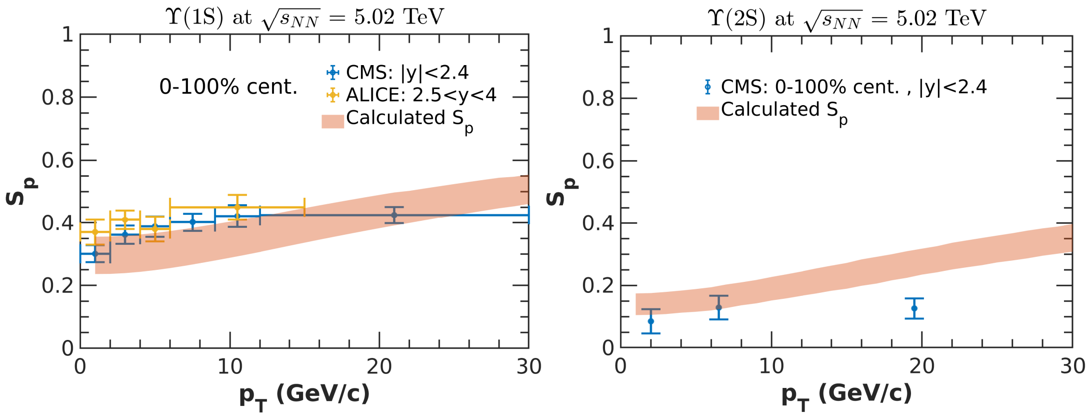

Figure 3.9: Transverse momentum dependence of suppression for Υ compared with R_{AA} at $\sqrt{s_{NN}} = 5.02$ TeV.

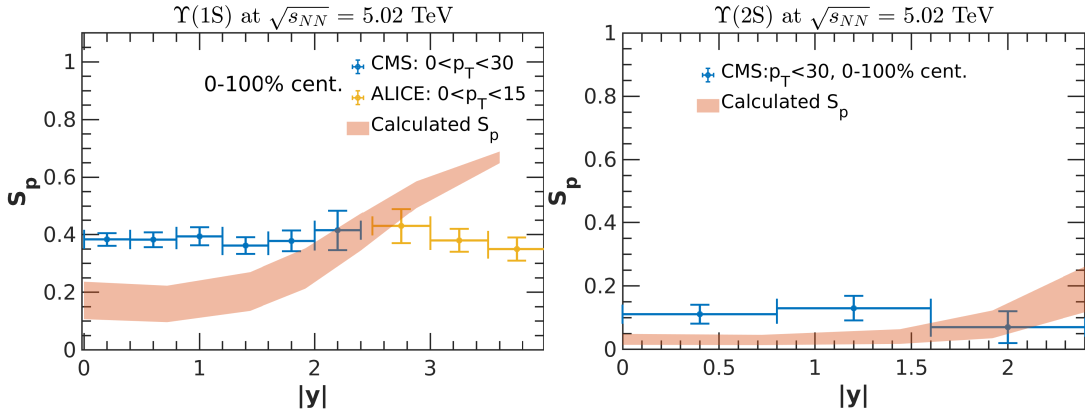

Figure 3.10: Rapidity dependence of suppression for Υ compared with R_{AA} at $\sqrt{s_{NN}} = 5.02$ TeV.

the uncertainty limit. Our predicted values show lesser suppression for $\Upsilon(2S)$ as compared with the corresponding experimental data. This rapidity dependence of suppression has become possible due to the interfacing of our earlier model with the ECHO-QGP's hydrodynamic expansion. Overall, for 2.76 TeV LHC center of mass energy, we find good agreement between our calculated bottomonium suppression values and the corresponding experimentally available data under the theoretical and measured uncertainty limit.

Fig. (3.8) depicts the variation of survival probability for both the bottomonium states with respect to the centrality at 5.02 TeV center of mass energy. The measured values of suppression from ALICE and CMS data shown on the same plot for comparison for $\Upsilon(1S)$ associated with the centrality dependence are quite close to each other. We clearly see a quite good agreement from Fig. (3.8) between our predicted values and the measured ones for both the bottomonium states over the whole centrality range. Since at 5.02 TeV LHC energy.

Transverse momentum dependence of the survival probability values are plotted in Fig. (3.9) along with the measured values of R_{AA} for both the bottomonium states at 5.02 TeV, center of mass energy. The agreement for $\Upsilon(1S)$ state is reasonably well, especially for low p_T values, whereas for $\Upsilon(2S)$, the predicted values are slightly less suppressed as compared to the CMS data.

Finally, rapidity dependent survival probability at 5.02 TeV energy is shown in Fig. (3.10) for both the bottomonium states. Compared with the corresponding experimental data, our results are close to the measured values for $\Upsilon(2S)$. For $\Upsilon(1S)$, our calculated suppression is not following the trend of ALICE and CMS data. We saw similar disagreement for the corresponding rapidity results at 2.76 TeV energy. These results might improve by further refining the input parameters taken in ECHO-QGP. Thus a complete dependence of bottomonium suppression for both the states spanning over two LHC energies has shown a convincing agreement with the measured values.

3.4 Summary

We have used a quarkonia suppression formalism to explain bottomonium suppression data at 2.76 TeV and 5.02 TeV LHC energies. ECHO-QGP has allowed us to find $(3 + 1)$-dimensional evolution of the relevant physical quantities associated with the medium formed just after the collisions. The temperatures at different centralities and rapidities have been extracted from the ECHO-QGP and fed into the suppression formalism. This facilitated us to include the rapidity dependence of suppression in formalism. The experimental data on transverse momentum(p_T) and rapidity(y) spectra have been utilized to fix the input parameters of the hydrodynamics. We have used the EOS from the Wuppertal-Budapest collaboration, which is computed from the first principle Lattice QCD. Modified color screening formalism has been used with the newer dynamics eliminating the need to assume a pressure profile for collisions in the transverse plane. The shadowing effect has been updated with the recent gluon PDFs and shadowing factors.

Chapter 4

Relativistic viscous hydrodynamics

Numerical simulations of relativistic hydrodynamics have been able to explain and predict measured data from high energy collision experiments. And at the same time, we have witnessed collision experiments pushing the development of relativistic hydrodynamics as a formal theory and its algorithmic implementation in simulations. The initial goal of fluid dynamics in the field of high energy physics had been to explain the low shear viscosity of quark-gluon matter and to put constraints on it. However, over the years, the ongoing progress in the field has opened up many new avenues, e.g., anisotropic fluid dynamics, hydrodynamics in small systems, the duality between fluid and gravity, contribution non-hydrodynamic modes, quasi-normal modes in black holes, etc. With the advent of LIGO's gravitational wave measurements, explaining neutron star mergers are also being explored. Nevertheless, here, we focus on the evolution of out-of-equilibrium hydrodynamics and its origin from microscopic theory in the limit.

4.1 Zeroth order hydrodynamics : Ideal fluid

The local four-velocity of fluid, $u^\mu \equiv \gamma(1, v^i)$, denotes the hydrodynamic flow. The hydrodynamic degrees of freedom are fluid four-velocity (u^μ), metric tensor

($g^{\mu\nu}$), and the Lorentz scalars – energy density (ϵ) and pressure (P) – using which we build the energy momentum tensor which is symmetric and transforms as a tensor under transformation. Following the standard procedure of effective field theories, we expand the charge current and the energy momentum tensor in powers of spatial derivatives. To 0^{th} order, it is given by the formula for ideal fluids:

$$\begin{aligned} N_0^\mu &= n_0 u^\mu, \\ T_0^{\mu\nu} &= \epsilon_0 u^\mu u^\nu - P_0 \Delta^{\mu\nu}, \end{aligned} \tag{4.1}$$

where $\Delta_{\mu\nu}$ is the projection operator which extracts the projection of the space-like part of the tensor it is operated on, which is given as:

$$\Delta^{\mu\nu} = g^{\mu\nu} + u^\mu u^\nu \tag{4.2}$$

This operator for an arbitrary $g^{\mu\nu}$ is orthogonal to the time-like velocity, $\Delta_{\mu\nu} u^\mu = \Delta_{\mu\nu} u^\nu = 0$ and it also satisfies the relation, $\Delta_{\mu\nu}\Delta^\nu_\rho = \Delta_{\mu\rho}$. And the thermodynamic quantities under local equilibrium in Eq. (4.1) are defined as:

$$\begin{aligned} \text{Conserved charge density :} \quad & n_0 = -u^\mu N_0^\mu, \\ \text{Pressure :} \quad & P_0 = \frac{1}{3}\Delta_{\mu\nu} T_0^{\mu\nu}, \\ \text{Energy density :} \quad & e_0 = u_\mu u_\nu T_0^{\mu\nu}. \end{aligned} \tag{4.3}$$

In the absence of external forces, the charge current and the energy momentum tensor are conserved:

$$\partial_\mu N_0^\mu = 0, \tag{4.4}$$

$$\partial_\mu T_0^{\mu\nu} = 0. \tag{4.5}$$

Here onwards, we consider the conservation of energy momentum tensor alone. We find the projection of the conservation equation along a direction parallel and perpendicular to the fluid four-velocity. The projection along the four-velocity is given as:

$$\begin{aligned} u_\nu \partial_\mu T^{\mu\nu}_{(0)} &= u^\mu \partial_\mu \epsilon + \epsilon\,(\partial_\mu u^\mu) + \epsilon\, u_\nu u^\mu \partial_\mu u^\nu - p\, u_\nu \partial_\mu \Delta^{\mu\nu}\,, \\ &= (\epsilon + p)\partial_\mu u^\mu + u^\mu \partial_\mu \epsilon = 0\ , \end{aligned} \tag{4.6}$$

where we used the identity $u_\nu \partial_\mu u^\nu = \frac{1}{2}\partial_\mu (u_\nu u^\nu) = \frac{1}{2}\partial_\mu 1 = 0$. And the projection of the direction perpendicular to four-velocity is,

$$\begin{aligned} \Delta^\alpha_\nu \partial_\mu T^{\mu\nu}_{(0)} &= \epsilon\, u^\mu \Delta^\alpha_\nu \partial_\mu u^\nu - \Delta^{\mu\alpha}(\partial_\mu p) + p\, u^\mu \Delta^\alpha_\nu \partial_\mu u^\nu \,, \\ &= (\epsilon + p)\, u^\mu \partial_\mu u^\alpha - \Delta^{\mu\alpha}\partial_\mu p = 0 \;. \end{aligned} \tag{4.7}$$

Where the covariant derivative (∂_μ) is decomposed along its spacial direction $\nabla^\mu \equiv \Delta^{\nu\mu}\partial_\nu$ and along temporal direction as $D \equiv u^\mu \partial_\mu$.

$$D\epsilon + (\epsilon + p)\partial_\mu u^\mu = 0 \tag{4.8}$$

$$(\epsilon + p) D u^\alpha - \nabla^\alpha p = 0 \;. \tag{4.9}$$

These two equations describe the ideal hydrodynamics.

4.2 Problem with ideal fluid dynamics

Ideal hydrodynamics ignore dissipation. The sound waves in ideal hydrodynamics would persist for an arbitrarily long time without damping. The presence of dissipation even outs the inhomogeneities in velocity, pressure, temperature, etc., due to the microscopic movement of fluid elements. Consider a system with constant intrinsic variables like pressure, density and energy density, and velocity of the volume elements as $v_y = v_z = 0$, $v_x \equiv v_x(y)$ as shown in Fig. (4.1). This is a homogeneous ideal fluid profile with velocity only along x direction, which varies with the depth of the fluid. However, this flow profile is not real as the microscopic fluid constituents moving along the y direction will transfer momentum along different layers of the fluid. This will make the velocity distribution profile more uniform, and the fluid will not remain stationary. This kind of frictional effect between fluid layers is characterized by dissipation.

To account for dissipation, one needs to add terms of gradients of hydrodynamic variables to the equation. But in order to allow gradient expansion, the extra terms added should be small. For hydrodynamics, quantities vary over the scale of fluid elements larger than the actual microscopic constituents length scale, the mean free path, i_{mfp}. We keep only those terms that are linear in the first gradient for now. This way, we can make up an effective theory of hydrodynamics.

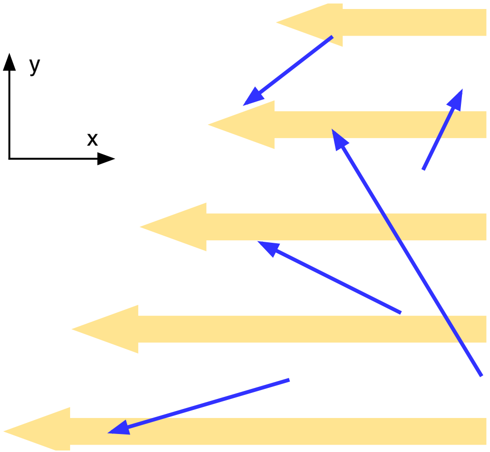

Figure 4.1: Stationary ideal fluid flow with a velocity gradient along y-direction is represented by thick yellow arrows. The thin blue arrows depict the flow of microscopic fluid constituents, which can transfer momentum from x to y direction, which will disrupt the stationary flow. Image source [141].

4.3 First order hydrodynamics : Navier-Stokes theory

To derive second-order relativistic viscous hydrodynamics, we begin with the fluid's energy momentum tensor:

$$\begin{aligned} T^{\mu\nu} &= T_0^{\mu\nu} + \Pi^{\mu\nu} \\ &= \epsilon u^\mu u^\nu - p\Delta^{\mu\nu} + \Pi^{\mu\nu}, \end{aligned} \tag{4.10}$$

where $\Pi^{\mu\nu}$ is the viscous stress tensor that stems from dissipation. For the ideal fluid case, energy and charge density local fluxes are in the same direction, i.e., $T^{\mu\nu}u^\nu = \epsilon u^\mu$ and $N^\mu = nu^\mu$. But for the relativistic system, the presence of dissipative currents leads to the separation of these two local fluxes. The *Landau frame* ($T^{\mu\nu}u^\nu = \epsilon u^\mu$) is where dissipation of energy does not appear explicitly and is which chooses the flow direction of total energy flux. In *Eckart frame* ($N^\mu = nu^\mu$), one chooses the direction of total conserved charge flux. In the Landau frame, the local rest frame is the frame where energy density is at rest, and in the Eckart frame, the local rest frame is where charge density is at rest. As the physics must be the same in either of these frames, one can show that heat flow in one frame is related to charge diffusion in the other frame [142]. Here we proceed with the Landau frame as we are not considering charge conservation.

Similar to the ideal fluid case, we project the energy momentum tensor conservation equation, $\partial_\mu T^{\mu\nu} = 0$ for the second order in the parallel and orthogonal direction to four-velocity:

$$\begin{aligned} u_\nu \partial_\mu T^{\mu\nu} &= D\epsilon + (\epsilon + p)\partial_\mu u^\mu + u_\nu \partial_\mu \Pi^{\mu\nu} = 0\,, \\ \Delta^\alpha_\nu \partial_\mu T^{\mu\nu} &= (\epsilon + p) D u^\alpha - \nabla^\alpha p + \Delta^\alpha_\nu \partial_\mu \Pi^{\mu\nu} = 0\ . \end{aligned} \tag{4.11}$$

In the above expressions, we have directly used the projection terms for the ideal part of $T^{\mu\nu}$ conservation equation from Eqs. (4.8) and (4.9). For the $\Pi^{\mu\nu}$ term above, we can use the following simplification:

$$\partial_\mu \left(u_\nu \Pi^{\mu\nu}\right) = u_\nu \partial_\mu \Pi^{\mu\nu} + \Pi^{\mu\nu} \frac{1}{2}\Big(\partial_\nu u_\mu + \partial_\mu u_\nu\Big). \tag{4.12}$$

Through the choice of frame, $u_\mu \Pi^{\mu\nu} = 0$, we lose the term on left hand side of the above equation, and the term $\frac{1}{2}(\ldots)$ denote symmetrization, for which we introduce a notation:

$$A_{(\mu} B_{\nu)} = \frac{1}{2}\left(A_\mu B_\nu + A_\nu B_\mu\right)\ . \tag{4.13}$$

Hence, the fundamental equations of relativistic fluid dynamics with viscosity are

$$D\epsilon + (\epsilon + p)\partial_\mu u^\mu - \Pi^{\mu\nu} \nabla_{(\mu} u_{\nu)} = 0 \tag{4.14}$$

$$(\epsilon + p) D u^\alpha - \nabla^\alpha p + \Delta^\alpha_\nu \partial_\mu \Pi^{\mu\nu} = 0\ . \tag{4.15}$$

Different forms of $\Pi^{\mu\nu}$ will lead to different theories of viscous fluid dynamics. To obtain the form of $\Pi^{\mu\nu}$, we look at the 2^{nd} law of thermodynamics, according to which entropy always increases for a closed system. Entropy density is related to energy density, temperature, and pressure by the following thermodynamic relation at equilibrium at zero chemical potential:

$$T ds = d\epsilon \qquad ; \qquad \epsilon + p = T s \tag{4.16}$$

The covariant form of the second law of thermodynamics is given as:

$$\partial_\mu s^\mu \geq 0, \tag{4.17}$$

s^μ here is the entropy 4-current in equilibrium, $s^\mu = s u^\mu$. Using the thermodynamic relations in Eq. (4.16), the second law could be rewritten as

$$\begin{aligned}\partial_\mu s^\mu &= Ds + \ (s)\ \partial_\mu u^\mu \\ &= \frac{1}{T}D\epsilon + \Big(\frac{\epsilon+\ p}{T}\Big)\partial_\mu u^\mu \\ &= \frac{1}{T}\Pi^{\mu\nu}\nabla_{(\mu}u_{\nu)} \geq 0\ ,\end{aligned} \tag{4.18}$$

where the simplification of the last line could easily be inferred from the Eq. (4.15). It is customary to split $\Pi^{\mu\nu}$ into a traceless part $\pi^{\mu\nu}$ (that is , $\pi^\mu_\mu = 0$) and a remaining part which has a non-zero trace,

$$\Pi^{\mu\nu} = \pi^{\mu\nu} + \Delta^{\mu\nu}\Pi\ . \tag{4.19}$$

For the traceless part of $\nabla_{(\mu}u_{\nu)}$, we now use the following new notation,

$$\nabla_{\langle\mu}u_{\nu\rangle} = 2\nabla_{(\mu}u_{\nu)} - \frac{2}{3}\Delta_{\mu\nu}\nabla_\alpha u^\alpha \tag{4.20}$$

Hence the second law of thermodynamics becomes:

$$\begin{aligned}\partial_\mu s^\mu &= \frac{1}{T}\Pi^{\mu\nu}\nabla_{(\mu}u_{\nu)} \\ &= \frac{1}{T}(\pi^{\mu\nu} + \Delta^{\mu\nu}\Pi)\nabla_{(\mu}u_{\nu)} \\ &= \frac{1}{2T}\pi^{\mu\nu}\nabla_{\langle\mu}u_{\nu\rangle} + \frac{1}{T}\Pi\nabla_\alpha u^\alpha \geq 0\end{aligned} \tag{4.21}$$

One choice of viscous stress tensor parts in order to satisfy the above inequality is:

$$\pi^{\mu\nu} = \eta\nabla^{\langle\mu}u^{\nu\rangle}\ , \quad \Pi = \zeta\nabla_\alpha u^\alpha\ , \quad \eta \geq 0\ , \quad \zeta \geq 0\ , \tag{4.22}$$

With these choices, $\partial_\mu s^\mu$ becomes a positive sum of squares. Eqs. (4.14), (4.15) and (4.22) constitute the relativistic Navier-Stokes theory of hydrodynamics.

4.4 Causality violation in Navier-Stokes equation

We will now do a perturbation analysis of the Navier-Strokes equation. Consider a small change in the energy density and fluid velocity of the system, which is at rest and in equilibrium:

$$u^\mu = (1, \vec{0}) + \delta u^\mu(t,x), \qquad \epsilon = \epsilon_0 + \delta\epsilon(t,x), \tag{4.23}$$

Here we assume a simplification in the perturbation that it only depends on just x-coordinate. The time evolution of the system is given by Navier-Stokes theory. Consider a particular direction in Eqs. (4.15) with $\alpha = y$:

$$(\epsilon + p)Du^y - \nabla^y p + \Delta^y_\nu \partial_\mu \Pi^{\mu\nu} \;=\; (\epsilon_0 + p_0)\partial_t \delta u^y + \partial_x \Pi^{xy} + \mathcal{O}(\delta^2) \;= 0 \tag{4.24}$$

The viscous stress tensor, $\Pi^{\mu\nu}$ of Eq. (4.19) with perturbations in its parts in Eq. (4.22) reduces to:

$$\Pi^{xy} = \eta\left(\nabla^x u^y + \nabla^y u^x\right) + \left(\zeta - \frac{2}{3}\eta\right)\Delta^{xy}\nabla_\alpha u^\alpha \;=\; -\eta_0\, \partial_x \delta u^y + \mathcal{O}(\delta^2)\ .$$

Using this, Π^{xy} in Eq. (4.24), we obtain a diffusion-like evolution equation for the variation in fluid velocity, $\delta u^y(t,x)$:

$$\partial_t \delta u^y - \frac{\eta_0}{\epsilon_0 + p_0}\partial_x^2 \delta u^y = \mathcal{O}(\delta^2)\ . \tag{4.25}$$

Consider a wave ansatz of mixed Laplace-Fourier kind to study different modes of the diffusion process,

$$\delta u^y(t,x) = e^{-\omega t + ikx} f_{\omega,k}.$$

Using it in your diffusion equation, Eq. (4.25), $\left(-\omega + \frac{\eta_0}{\epsilon_0 + p_0}k^2\right) f_{\omega,k} = 0$, we obtain a dispersion relation,

$$\omega = \frac{\eta_0}{\epsilon_0 + p_0}k^2\ , \tag{4.26}$$

We can find an estimate of the diffusion speed for a mode with wavenumber k as,

$$v_T(k) = \frac{d\omega}{dk} \;=\; 2\frac{\eta_0}{\epsilon_0 + p_0}k\ . \tag{4.27}$$

Note that v_T increases linearly with the wavenumber, which implies that with large k, the diffusion speed can attend an indefinitely larger value, even exceeding the speed of light, hinting **violation of causality**. This non-physical behavior of the relativistic Navier-Stokes theory occurs only for modes with short wavelengths ($k \gg 1$). And hydrodynamics is considered as an effective theory in the long wavelength limit ($k \to 0$). To avoid the instabilities of solutions at high k modes, there is a need to regulate the theory somehow.

One can regulate this theory in the following way. Instead of the Navier-Stokes equation, consider the *Maxwell-Cattaneo law* [143, 144],

$$\tau_\pi \partial_t \Pi^{xy} + \Pi^{xy} = -\eta_0 \partial_x \delta u^y \tag{4.28}$$

Here τ_π is a coefficient called as *relaxation time.*

We calculate the dispersion relation again for the perturbation δu^y with Eq. (4.28),

$$\omega = \frac{\eta_0}{\epsilon_0 + p_0} \frac{k^2}{1 - \omega \tau_\pi} \ , \tag{4.29}$$

In the hydrodynamics limit, $\omega, k \to 0$, we find the above relation coinciding with the diffusion equation of Navier-Strokes theory. The mode propagation speed for this modified dispersion relation is given as

$$v_T^{\max} \equiv \lim_{k \to \infty} \frac{d|\omega|}{d\ k} = \sqrt{\frac{\eta_0}{(\epsilon_0 + p_0)\tau_\pi}} \ , \tag{4.30}$$

which is finite and less than 1 in the limit $k \gg 1$ unless $\tau_\pi \to 0$.
Even though Maxwell-Cattaneo law is phenomenologically successful in restoring causality in Navier-Stokes theory, it is still an unsatisfactory extension as Eq. (4.28) does not originate from any first principle and has been introduced in an ad hoc manner. .

4.5 Second order hydrodynamics : Müller Israel Stewart theory

In Sec (4.3), for deriving the Navier-Stokes equation, we made use of entropy current for the equilibrium case, $s^\mu = s u^\mu$ in the covariant second law of thermodynamics, $\partial_\mu s^\mu \geq 0$. For a viscous fluid, the system could be out of equilibrium which would reflect in the entropy current expression. Ingo Müller [145], W. Israel and J. Stewart [146] (MIS) suggested that a contribution from viscous stress tensor to the entropy four current, which under the assumption that the deviations from equilibrium are not so large, the entropy current is given as [147]:

$$s^\mu = s u^\mu - \frac{\beta_0}{2T} u^\mu \Pi^2 - \frac{\beta_2}{2T} u^\mu \pi_{\alpha\beta}\pi^{\alpha\beta} + \mathcal{O}(\Pi^3) \ , \tag{4.31}$$

where β_0, β_2 are coefficients quantifying the strength of respective terms in second-order modifications of the entropy current. We follow the same procedure as we did in Sec. (4.3) to obtain the second law of thermodynamics as:

$$\begin{aligned}\partial_\mu s^\mu &= \frac{\pi^{\alpha\beta}}{2T}\left(\nabla_{\langle\alpha}u_{\beta\rangle} - \pi_{\alpha\beta}TD\left(\frac{\beta_2}{T}\right) - 2\beta_2 D\pi_{\alpha\beta} - \beta_2\pi_{\alpha\beta}\partial_\mu u^\mu\right)\\ &+\frac{\Pi}{T}\left(\nabla_\alpha u^\alpha - \frac{1}{2}\Pi\; TD\left(\frac{\beta_0}{T}\right) - \beta_0 D\Pi - \frac{1}{2}\beta_0\Pi\partial_\mu u^\mu\right) \geq 0\;. \qquad (4.32)\end{aligned}$$

The above inequality is guaranteed to be fulfilled if the viscous stress tensor parts have the form:

$$\boxed{\begin{aligned}\pi_{\alpha\beta} &= \eta\left(\nabla_{\langle\alpha}u_{\beta\rangle} - \pi_{\alpha\beta}TD\left(\frac{\beta_2}{T}\right) - 2\beta_2 D\pi_{\alpha\beta} - \beta_2\pi_{\alpha\beta}\partial_\mu u^\mu\right)\;,\\ \Pi &= \zeta\left(\nabla_\alpha u^\alpha - \frac{1}{2}\Pi\; TD\left(\frac{\beta_0}{T}\right) - \beta_0 D\Pi - \frac{1}{2}\beta_0\Pi\partial_\mu u^\mu\right)\;, \qquad (4.33)\end{aligned}}$$

where ζ is the bulk viscosity and η is the shear viscosity coefficient. In the limit of $\beta_0, \beta_2 \to 0$, Eq. (4.33) follows the Navier-Stokes equation. For finite values of β_0 and β_2, Eq. (4.33) contains terms with time derivatives of Π and $\pi_{\alpha\beta}$, which are in a way similar to the Maxwell-Cattaneo law, Eq. (4.28) if we identify $\beta_2 = \frac{\tau_\pi}{2\eta}$ and $\beta_0 = \frac{\tau_\Pi}{\zeta}$). The set of Eq. (4.14),(4.15) and (4.33) (and their variation) are called as “Müller-Israel-Stewart” equations for the 2^{nd} order fluid dynamics.

4.6 Hydrodynamics as a microscopic theory in the limit

The dynamics of any self-interacting system that adheres to Lorentz symmetry consists of excitations of fluid and non-fluid-like degrees of freedom. In the last section, we saw the evolution of relativistic hydrodynamics from a traditional point of view. Here we look at the origin of hydrodynamics with microscopic theory in a limit. We will first look at a general procedure and the meaning of hydrodynamic and non-hydrodynamic modes and we later derive the non-hydrodynamic mode for MIS theory.

4.6.1 Hydrodynamic and non-hydrodynamic modes

An essential criterion for dynamics to be explained with hydrodynamics is that the microscopic description of the system should, at late stages, show quasi-universal behavior in its evolution. This means that such a system would have a reduction in the number of degrees of freedom accessible to the system, and it eventually develops local thermodynamic equilibrium. For the phenomenological application of hydrodynamics for high energy collisions, we start with the energy momentum tensor, $\langle \hat{T}^{\mu\nu} \rangle$, in a microscopic model. This tensor can be treated as an operator for QFT applications. The following treatment of hydrodynamics can be carried out for any out-of-equilibrium microscopic theory, e.g., QFT, AdS/CFT, and Kinetic theory. We use the "mostly plus" metric signature $(-,+,+,+)$ in this section. The simplest of states in microscopic theory can be described with linear response theory, where we start a state in equilibrium and subject it to a small perturbation.

$$\hat{T}^{\mu\nu} = \langle \hat{T}^{\mu\nu} \rangle_{eq} + \delta \langle \hat{T}^{\mu\nu} \rangle, \tag{4.34}$$

where, $\langle \hat{T}^{\mu\nu} \rangle_{eq}$ and $\delta \langle \hat{T}^{\mu\nu} \rangle$ represents the *equilibrium* and *deviation from equilibrium* parts of the complete energy momentum tensor respectively. The perturbations that we consider here are in the background metric $g_{\mu\nu}$ that directly couples to $\hat{T}^{\mu\nu}$. The perturbation $(\delta g_{\alpha\beta}(y))$ in the flat spacetime metric $(\eta_{\alpha\beta})$ results in a variation in the expectation value of $\hat{T}^{\mu\nu}$, given as:

$$\delta \langle \hat{T}^{\mu\nu} \rangle (x) = -\frac{1}{2} \int d^4y \, G_R^{\mu\nu,\alpha\beta}(x^0 - y^0, \mathbf{x} - \mathbf{y}) \, \delta g_{\alpha\beta}(y), \tag{4.35}$$

where $G_R^{\mu\nu,\alpha\beta}(x^0 - y^0, \mathbf{x} - \mathbf{y})$ is the two point retarded correlator of the energy-momentum tensor calculated considering a global thermal equilibrium state of temperature T and is given as :

$$G_R^{\mu\nu,\alpha\beta}(x^0 - y^0, \ \mathbf{x} - \mathbf{y}) = -i \, \theta(x^0 - y^0) \langle [\hat{T}^{\mu\nu}(x), \hat{T}^{\alpha\beta}(y)] \rangle_T .$$

$G_R^{\mu\nu,\alpha\beta}$ is also referred to as the linear response function in the formal theory. We consider the *retarded* correlator here because the response follows the cause – perturbation in metric. Eq. (4.35) in the Fourier space is:

$$\delta \langle \hat{T}^{\mu\nu} \rangle (x) = -\frac{1}{2} \frac{1}{2(2\pi)^4} \int d^3k \int d\omega \, e^{-i\omega x^0 + i \mathbf{k}\cdot\mathbf{x}} \, G_R^{\mu\nu,\alpha\beta}(\omega, \mathbf{k}) \, \delta g_{\alpha\beta}(\omega, \mathbf{k}), \tag{4.36}$$

where the momentum $\mathbf{k}$ and frequency ω are the Fourier-transformed arguments. The frequency (ω) integral is over $\mathbb{R}$ and the momenta ($\mathbf{k}$) integral is taken over $\mathbb{R}^3$. The two point retarded correlator of the energy-momentum tensor can be decomposed into the addition of three independently evolving terms in the presence of rotational symmetry of the thermal state [148]. For simplicity, assume that the momentum along z-direction $\mathbf{k} = (0, 0, k)$ direction, then the three decoupled sets of components give the following three modes/channels:

- scalar → $\delta\langle\hat{T}^{12}\rangle)$
- shear → $\delta\langle\hat{T}^{0a}\rangle$, $\delta\langle\hat{T}^{3a}\rangle$ for $a = 1, 2$
- sound → $\delta\langle\hat{T}^{00}\rangle$, $\delta\langle\hat{T}^{03}\rangle$, $\delta\langle\hat{T}^{33}\rangle$

When we take $\mathbf{k} = 0$, or if we consider temperature to be zero, then all the three channels stated above will coincide. The frequency (ω) integral in Eq. (4.36) can

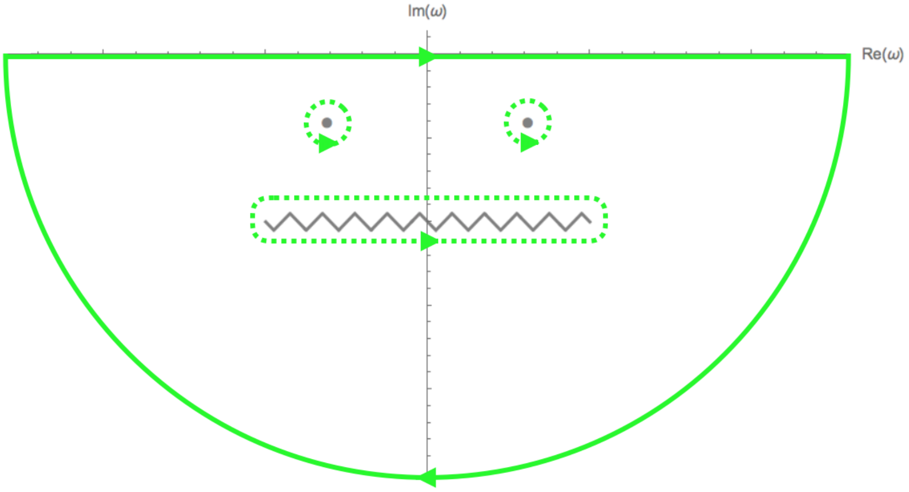

Figure 4.2: The plot depicts a typical contour considered for solving the complex frequency integral in Eq. (4.36) for a given value of $\mathbf{k}$. The retarded correlator is analytic in the upper quadrants of complex plane [141]. The singularities for different microscopic theories could take the form of single poles or branch cuts of the two point retarded correlator, $G_R^{\mu\nu,\alpha\beta}(\omega, \mathbf{k})$, in the lower half of the complex plane. Such singular contributions could be called a mode. There could be finite or infinite modes of a microscopic model. The modes nearest to the real axis are dominant, and they are the least damped ones. Image source [149].

be evaluated as the contour integration in terms of the singularities of retarded correlator as shown in Fig. (4.2) From studies based on free QFT [150] holography [148, 151, 152] and kinetic theory [153], we expect in general singularities as either single poles or as branch cuts, located symmetrically to the imaginary axis. For a given value of frequency, $\omega = \omega_{\text{sing}}(k)$, the singularity at late times provides a contribution of the form,

$$\delta\langle\hat{T}^{\mu\nu}\rangle(x) \sim e^{-i\,\omega_{\text{sing}}(k)\,x^0 + i\,\mathbf{k}\cdot\mathbf{x}}, \tag{4.37}$$

where $\omega_{\text{sing}}(k)$ is a complex frequency whose real part is responsible for the time oscillations while energy momentum tensor approaches to its equilibrium form. Such singularities are called as **hydrodynamic modes** – an excitation of equilibrium plasma. Furthermore, the imaginary part of $\omega_{\text{sing}}(k)$ is called **non-hydrodynamic mode** and is responsible for dissipation. These could be modeled as a solution of linearized hydrodynamic equations. The time for equilibration for each of such modes is proportional to $1/\Im[\omega_{\text{sing}}(k)]$ the ones for which $\Im[\omega_{\text{sing}}(k)] \to 0$ are long-lived ones. Both the non-hydrodynamic and hydrodynamic modes are together called as the collective modes of the system. In the case of the absence of conserved charges, there are just two types of hydrodynamic modes, one occurring in the sound channel and the other from the shear channel. The non-hydrodynamic modes are also called transient modes as they are short-lived relative to the longest timescale of $1/\Im[\omega_{\text{sing}}(k)]$.

For many causal systems, one can attempt to find the analytic structures of the underlying microscopic theory as shown in Fig. (4.3). However, we know little about the excitations in QCD at non-zero temperatures and at densities achieved in high energy collisions. Finding the non-hydrodynamic modes of QGP through experimental measurements could help us find the underlying dynamics of the system. We cannot observe these modes directly from the collision, obviously, but the non-hydrodynamic modes may leave some detectable signature on the dynamical evolution of the system. This is feasible when the hydrodynamic mode is well separated from the non-hydrodynamic mode, the latter of which is dominant. Such a situation may occur in peripheral heavy-ion collisions and in small systems.

4.6.2 Non-hydrodynamic mode in MIS theory

The procedure of finding poles of retarded correlator varies between theories. Here we motivate it for MIS theory. Eq. (4.35) for a classical system can be reframed as follows to calculate the retarded potential by considering the variation

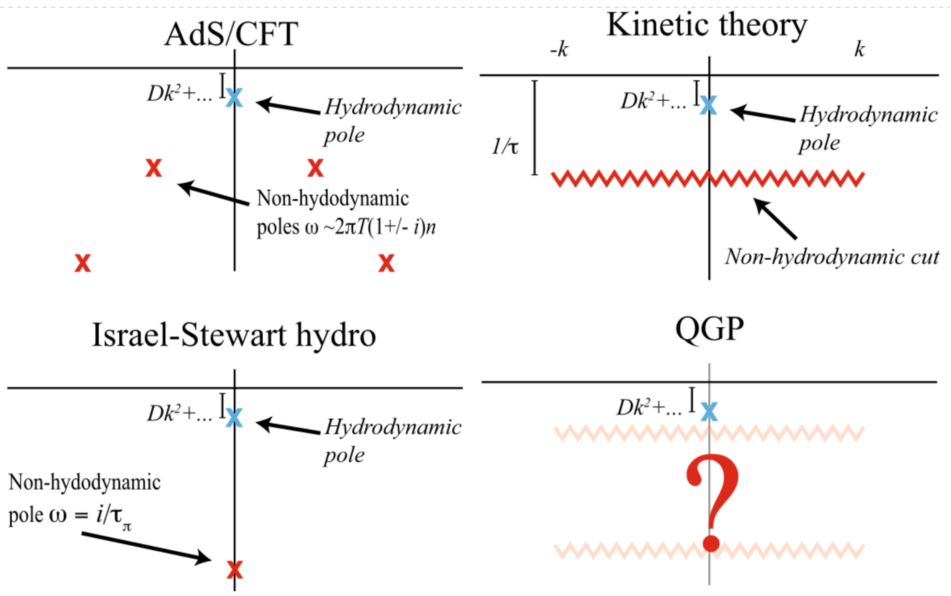
AdS/CFT
Dk²+... I
Hydrodynamic pole
Non-hydodynamic poles ω ~2πT(1+/- i)n
Kinetic theory
-k
k
1/τ
Dk²+... I
Hydrodynamic pole
Non-hydrodynamic cut
Israel-Stewart hydro
Dk²+... I
Hydrodynamic pole
Non-hydodynamic pole ω = i/τ_π
QGP
Dk²+... I
?

Figure 4.3: Analytic structure appearing in different microscopic models of fluids. All self-interacting systems with Lorentz symmetry have hydrodynamic poles (blue cross) in the long wavelength limit. The non-hydrodynamic sector varies among theories and closely depicts the degrees of freedom of the underlying microscopic theory. The goal is to determine the underlying QGP dynamics in high energy collisions and their analytic structure. Image source [154]

of $T^{\mu\nu}$ with respect to the metric,

$$G^{\mu\nu,\gamma\delta} = -2\left.\frac{\delta T^{\mu\nu}\left(g,t,\mathbf{x}\right)}{\delta g_{\gamma\delta}}\right|_{g=\text{Minkowski}} . \tag{4.38}$$

We first try finding the retarded correlator for the Navier-Stokes equation using a variational approach [155]. Recall the energy momentum tensor for this theory from Eq. (4.2), (4.10) and (4.19),

$$T^{\mu\nu} = \epsilon u^{\mu}u^{\nu} - p(g^{\mu\nu} + u^{\mu}u^{\nu}) + (\pi^{\mu\nu} + \Pi). \tag{4.39}$$

The small fluctuation in the metric $\delta g_{\mu\nu}$ will induce a fluctuation in ϵ and u^{μ} as $\delta\epsilon$ and δu^{μ} respectively around a constant background. Up to a linear order in perturbation, we find,

$$\delta T^{\mu\nu} = \delta\epsilon u_0^{\mu}u_0^{\nu} + \left(c_s^2\delta\epsilon + \delta\Pi\right)\Delta_0^{\mu\nu} + 2(\epsilon_0 + P_0)\delta u^{(\mu}u_0^{\nu)} + P_0\delta g^{\mu\nu} + \delta\pi^{\mu\nu}\,, \tag{4.40}$$

where

$$\delta\Pi = -\zeta\delta\nabla\cdot u\,, \quad \delta\pi^{\mu\nu} = -\eta\delta\sigma^{\mu\nu}\,. \tag{4.41}$$

For the perturbation in metric, the condition $u^\mu u_\mu = -1$ leads to $u^0 = 1 + \frac{\delta g_{00}}{2}$. To calculate the retarded correlator in Eq. (4.38), the $\delta\epsilon$, δu^μ, $\delta\pi^{\mu\nu}$ and $\delta\Pi$ terms needs to be expanded to first order in perturbation source, $\delta g_{\mu\nu}$. Perturbations also enter in velocity gradient term through Christoffel symbols :

$$\nabla_\mu u^\nu = \partial_\mu u^\nu + \Gamma^\nu_{\mu\lambda} u^\lambda \qquad ; \quad \Gamma^\nu_{\mu\lambda} = \frac{1}{2} g^{\nu\rho}(\partial_\mu g_{\rho\lambda} + \partial_\lambda g_{\rho\mu} - \partial_\rho g_{\mu\lambda}). \tag{4.42}$$

Calculating all of these terms is a tedious task hence we select a metric perturbation along a specific direction as $\delta g^{\mu\nu} = \delta g^{\mu\nu}(t, x_3)$ which is equivalent to setting the direction of wave vector $\mathbf{k} = k\mathbf{e}_3$. With this choice and using Eq. (4.40) in Eq. (4.38) we obtain the correlator which we Fourier transform as

$$G_R^{\mu\nu,\alpha\beta}(\omega, k) = 2\pi \int_{-\infty}^{\infty} dt\; e^{\omega t} G_R^{\mu\nu,\alpha\beta}(t, k). \tag{4.43}$$

The retarded correlator in momentum space are [141]:

$$\begin{aligned} G^{00,00}(\omega, k) &= -2\epsilon_0 + \frac{k^2(\epsilon_0 + P_0)}{\omega^2 - c_s^2 k^2 + i\omega k^2 \gamma_s}\,, \\ G^{01,01}(\omega, k) &= \epsilon_0 + \frac{k^2 \eta}{i\omega - \gamma_\eta k^2}\,, \\ G^{12,12}(\omega, k) &= P - i\eta\omega\,, \end{aligned} \tag{4.44}$$

where γ_η is the shear damping length and γ_s is the sound attenuation lengths given as as

$$\gamma_\eta \equiv \frac{\eta}{\epsilon_0 + P_0}\,, \qquad \gamma_s = \frac{4\eta}{3(\epsilon_0 + P_0)} + \frac{\zeta}{(\epsilon_0 + P_0)}\,. \tag{4.45}$$

Results in Eqs.(4.44) are accurate only to the first order in k and ω as they were obtained from 1^{st} order Navier Stokes hydrodynamics. But our system of interest is 2^{nd} order hydrodynamics which is causal and satisfies the Maxwell-Cattaneo relations for $\pi^{\mu\nu}$ and Π :

$$\tau_\pi D\pi^{\mu\nu} + \pi^{\mu\nu} = -\eta\sigma^{\mu\nu} \tag{4.46}$$

where $\sigma^{\mu\nu}$ is called the shear flow tensor. Considering small perturbation in Eq. (4.46) in momentum space gives us:

$$\delta\pi^{\mu\nu} = -\eta \frac{\delta\sigma^{\mu\nu}}{1 - i\omega\tau_\pi} \tag{4.47}$$

We can replace the perturbed $\delta\pi^{\mu\nu}$ in Eq. (4.41) with the above one, and thus we can obtain the correlator for second order hydrodynamics by replacing $\eta \to \frac{\eta}{1-i\omega\tau_\pi}$ in Eq. (4.44). And hence the retarded correlator for the shear channel is given as:

$$G^{01,01}(\omega,k) = \epsilon_0 + \frac{k^2(\frac{\eta}{1-i\omega\tau_\pi})}{i\omega - (\frac{\gamma_\eta}{1-i\omega\tau_\pi})k^2} \tag{4.48}$$

$$\tag{4.49}$$

$$G^{01,01}(\omega,k) = \epsilon_0 + \frac{k^2\eta}{i\omega(1-i\omega\tau_\pi) - \gamma_\eta k^2}\,. \tag{4.50}$$

We finally find the poles of this correlator has two single poles located at,

$$\omega^+ = \frac{-i + \sqrt{4\gamma_\eta k^2\tau_\pi - 1}}{2\tau_\pi}\,, \quad \omega^- = \frac{-i - \sqrt{4\gamma_\eta k^2\tau_\pi - 1}}{2\tau_\pi}\,. \tag{4.51}$$

At $k = 0$, the pole ω^+ vanishes. One of the features of Maxwell Cattaneo's theory is the emergence of new modes, which was not present in Navier Stoke's theory, which can be obtained by Taylor expanding ω^- for $k = 0$ in Eq. (4.51),

$$\boxed{\omega^-(k) \simeq -\frac{i}{\tau_\pi} + i\gamma_\eta k^2 + \dots} \tag{4.52}$$

According to this dispersion relation, this mode is over-damped, and it does not vanish as $k \to 0$. This $\lim_{k\to 0}\omega^- \to$ (const) behavior is apparently not consistent with the regime where gradient expansion applies, which requires both k and ω to be small. This ω^- mode is a non-hydrodynamic mode in the shear channel. The working definition for a **non-hydrodynamic mode** is it being absent for Navier Stokes theory. While this is a terrible way to define it, no suitable alternate definition (and name) has come up yet. From Eq. (4.52), we could say that **in the leading order, the non-hydrodynamic mode is related to the *shear relaxation time*, τ_π, of the MIS theory**. The study of non-hydrodynamic modes for various microscopic theories is still in its infancy, but recent studies suggest that they are an unavoidable feature of theories and may offer insights into the degrees of freedom of a given underlying microscopic theory under consideration.

Evaluating linearised hydrodynamics provided us with two-point correlations

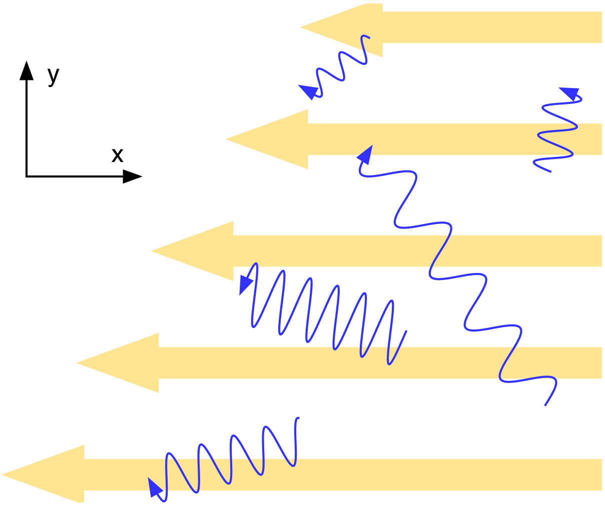

Figure 4.4: The thick arrows correspond to the shear mode of the inhomogeneous velocity profile $v_x(y)$ of the flow of the medium. When the medium is in local thermal equilibrium, the sound and shear modes generate fluctuations represented by wiggly arrows. The propagation of these modes and the interaction between them contribute to the generation of shear viscosity. Image source [141].

of $T^{\mu\nu}$ in equilibrium state and encountered modes that are freely propagating. By analyzing the non-linearities of the hydrodynamic equation, the interaction between modes could be found out. The correlations at equilibrium for the current, J^μ and energy momentum tensor, $T^{\mu\nu}$ will be modified by these interactions between modes. This will furthermore recast the transport coefficients σ, η, and ζ from their initial values set in the first order hydrodynamics. In addition to equilibration due to momentum exchange between layers of fluid, as shown in Eq. (4.1), the momenta are also transferred at a short wavelength than the length scale of the flow inhomogeneity. These collective excitations are due to the sound and shear channel non-hydrodynamics mode and the interaction between them and are present even in thermal equilibrium. that of the inhomogeneous flow through shear and sound mode collective excitations as shown in Fig. (4.4). Even in thermal equilibrium, these collective excitations will be present, which will modify the measured shear viscosity from the equilibrium two point correlation function due to contribution from collective modes.

Chapter 5

Finding the onset of hydrodynamization using the non-hydrodynamic mode

5.1 Introduction and literature review

The fact that baryons have internal structure directly leads to the notion that a bulk medium of sub-nucleonic degrees of freedom should exist [156, 157]. An energy density of about 0.7 GeV/fm^3 is required to free up quarks from the nucleons [158, 159]. We now have convincing signs from experiments at the BNL Relativistic Heavy Ion Collider (RHIC) and the CERN Large Hadron Collider(LHC) that indicate a deconfined state of quarks and gluons called quark-gluon plasma (QGP) is formed for a sufficient distinguishable duration. Low-order hydrodynamic constitutive relations apparently explain the experimental observables of such a dynamic system quite well, even though there is a sizable pressure anisotropy. This applicability of low-order hydrodynamics has been referred to as *hydrodynamization*,[1], to distinguish it from local thermalization [160, 161]. Experimental confirmation of strangeness enhancement [162], elliptic flow [163] and jet quenching [164, 165] as the early indicators was subsequently followed by confirmation of other signatures like quarkonia suppression. Efforts now are directed towards quantitatively fixing the boundaries of various regions of Quantum Chromodynamics(QCD) phase diagram [166] and deducing the properties of QGP [167].

---

[1] In this study, we will refer to the applicability of low-order hydrodynamics as "hydrodynamization", in accordance with its definition in Ref. [160].

There are challenges involved in analytically solving non-perturbative QCD making the proof of deconfinement intractable [168]. Hence the progress in modeling a medium of quarks and gluons from first principles has been limited. Lattice QCD, even though computationally intensive, has been of help in understanding deconfinement, and other low-density phenomena where the numerical sign problem does not affect the calculations [169, 170]. For now, phenomenological models aided by lattice QCD seem to be the right approach in modeling such a complex system. The use of hydrodynamics in modeling the transient QGP stage has been quite surprising [171]. However, hydrodynamics as an effective theory for heavy-ion collisions, has evolved tremendously, especially in the last two decades. For an in-depth review of the hydrodynamics in heavy-ion collisions, please look up Refs. [172–178]. Apart from the traditional conversation equation approach, hydrodynamics can also be derived as a microscopic theory in the limit e.g., starting from kinetic theory or any QFT like QCD provided its dynamics show a quasi-universality at a large time scale [176]. This microscopic theory approach also helps in fixing the transport coefficients of the theory [173].

The energy momentum tensor for such a theory in a non-equilibrium state is decomposed as;

$$T^{\mu\nu} = \langle \hat{T^{\mu\nu}} \rangle_{eq} + \delta \langle \hat{T^{\mu\nu}} \rangle, \tag{5.1}$$

where the first and second term represents the equilibrium state of $T^{\mu\nu}$ and the deviation from the equilibrium, respectively. Under linear response theory, the second term can be expanded as;

$$\delta \langle \hat{T^{\mu\nu}} \rangle(x) = -\frac{1}{2} \int d^4 y G_R^{\mu\nu,\alpha\beta}(x^0 - y^0, \mathbf{x} - \mathbf{y}) \delta g_{\alpha\beta}(y), \tag{5.2}$$

where, $G_R^{\mu\nu,\alpha\beta}(x^0 - y^0, \mathbf{x} - \mathbf{y})$ is the retarded $2-$point correlator of $T^{\mu\nu}$. And $\delta g_{\alpha\beta}(y)$ is a small perturbing term added to flat space-time metric. This correlator when expressed in the Fourier space $[G_R^{\mu\nu,\alpha\beta}(\omega, \mathbf{k})]$, where ω is the angular frequency and, $\mathbf{k}$ is the momentum, has singularities. The solution of the $\delta \langle \hat{T^{\mu\nu}} \rangle(x)$ integral at late times has a contribution in terms of complex singular frequency in the ω-plane;

$$\omega_{sing} = \omega_h + i\,\omega_{nh} \tag{5.3}$$

where ω_h is the real part of frequency at singularity corresponding to excitation of equilibrium plasma, also called *hydrodynamic mode frequency*. ω_{nh} is termed as transient mode or *non-hydrodynamic mode frequency* and is associated with the dissipative effects. The transient mode is responsible for the disruption of the hydrodynamization process and is controlled with the *relaxation time* parameter which sets the duration for which viscous effects remain active. These are called the *quasi-normal modes* of out-of-equilibrium hydrodynamics, analogous to the *normal modes* of oscillatory systems in classical mechanics.

Right after the collision of heavy ions, we have a non-equilibrium system of partons for up to 1 fm/c. The fact that applying low-order hydrodynamics does not require local thermalization or even pressure isotropy to show agreement with the measurements [179] had been puzzling until we discovered that this evolution leads to an attractor [180–183]. This attractor guides the system evolution to a late-time universal trajectory even if initiated with a varied set of starting conditions [184].

The framework of hydrodynamics with initial conditions, followed by a hadron after-burner, has been quite successfully used to explain experimental data obtained from a wide range of systems [185, 186]. From most central to ultra-peripheral collisions, the system size decreases monotonically. For constant collisional energy, there should be a system size below which the QGP droplet will cease to *hydrodynamize* [187] as illustrated in Fig (5.1). Aleksi Kurkela *et al.*, [188] has performed a flow analysis with kinetic theory leading to hydrodynamization through a dimensionless physical quantity called opacity($\hat{\gamma}$) – a measure of transverse system size in terms of the mean free path. As the opacity varies from 0 to 5, the system goes through 3 stages in this order:(a) non-QGP (particle-like) stage, (b) intermediate transition stage, and (c) QGP (hydro-like) stage. Ulrich Heinz and Moreland [189] have emphasized considering the multiplicity rapidity density of charged particle – dN/dy along with HBT radii to quantify the smallest QGP size. According to Romatschke [178], the large p_T regime of flow is due to the non-hydrodynamic mode, and this mode can be studied through the relaxation time approach. He suggested that a large deviation of elliptic flow (v_2) for a variation in shear relaxation time for lowering multiplicity could potentially indicate a breakdown of low-order hydrodynamics. The last two of the above studies came

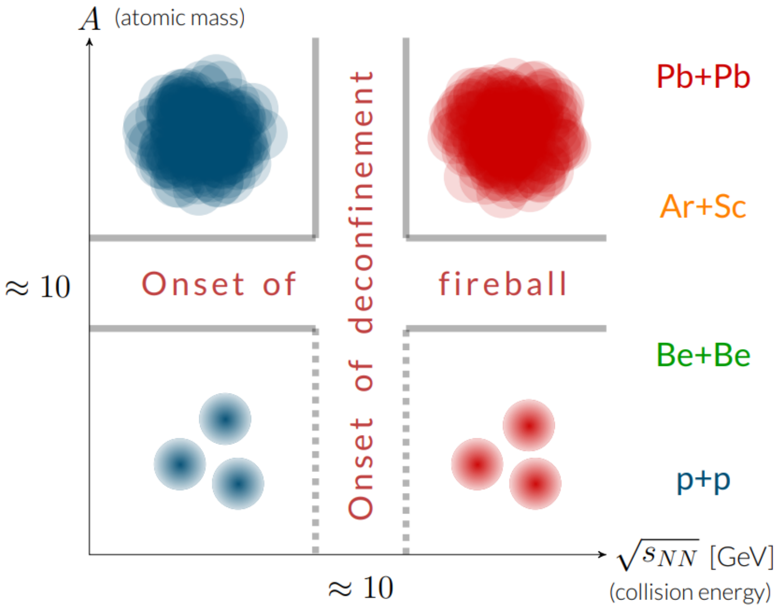

Figure 5.1: The four domains of hadron production are separated by two thresholds. Out of which the onset of deconfinement at low mass nuclei interactions is questionable. Finding the presence of these thresholds and their location is the aim. The present study deals with the onset at high $\sqrt{s_N}$ regime. Image source [27]

to the conclusion that this limit should be around or below $dN_{ch}/dy \approx 2$.

The role of relaxation time has been previously analyzed for different settings in hydrodynamics studies [190–194], including spatial and momentum eccentricity, entropy and elliptic flow for varying relaxation times. However, the primary focus of these studies was to find the range of τ_π and other second-order transport coefficients for which the observables were insensitive, which in turn meant that the magnitude of the second-order gradient terms is smaller in comparison to those of first-order gradient. In the present work, we check the sensitivity of observables to shear relaxation time in ultra-peripheral collision systems to test the breakdown of low-order hydrodynamics. In Sec. (5.2) we discuss the framework of the model used. In Sec. 5.2.1, we state the initial condition and input parameters involved in the model. Sec. (5.2.2) describes the observables obtained along with the experimental results in order to fix the centrality-related parameters. In Sec. (5.3), we present the results of elliptic flow as a function of transverse momentum and multiplicity rapidity density. And in Sec. (5.4), inferences are drawn based on results obtained along with the possible improvement to this work.

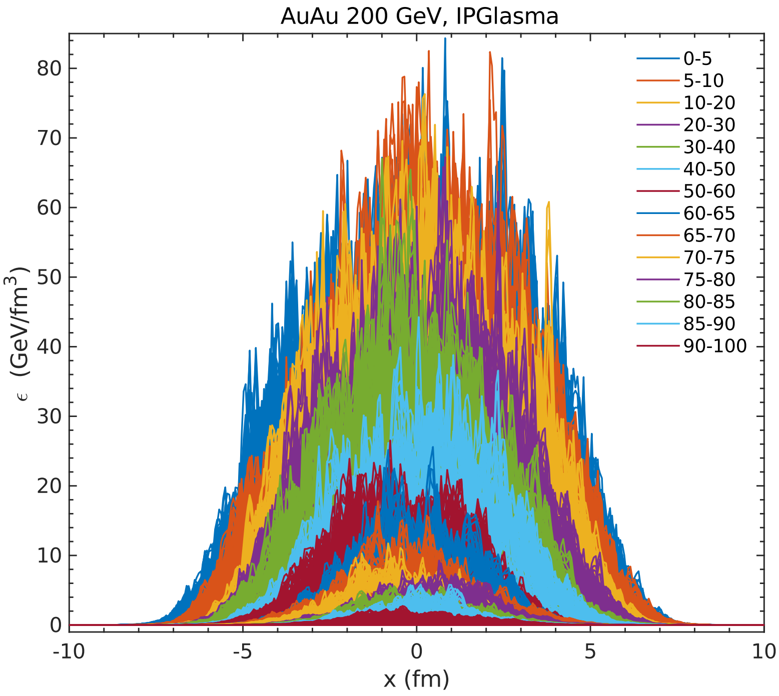

Figure 5.2: Energy density distribution as a function of transverse coordinate at $\tau = 0.6$ fm, midrapidity for 14 centrality classes of Au-Au IPGlasma runs at 200 GeV. The distribution for each centrality class has been superimposed for 400 IPGlasma events with different nucleon positions to account for event-by-event fluctuations.

5.2 Formalism

Hydrodynamics is the collective dynamical evolution of a suitably sized bulk medium adhering to the system's symmetries. For the relativistic case, the conservation laws take the form $\partial_\mu T^{\mu\nu} = 0$ for energy momentum tensor and $\partial_\mu N^\mu = 0$ for the conserved charge. The local values of temperature, $T(x)$, fluid velocity, $u_\mu(x)$, and chemical potential, $\mu(x)$ are chosen as hydrodynamic variables. For ultra-relativistic collisions, where a negligible amount of participating nucleons survive, the conservation equation for baryon number ($\partial_\mu N^\mu = 0$) can be ignored. The energy-momentum tensor can be decomposed as [199],

$$T^{\mu\nu} = \epsilon u^\mu u^\nu + \Delta^{\mu\nu} P + (w^\mu u^\nu + w^\nu u^\mu) + \Pi^{\mu\nu}. \tag{5.4}$$

Here, ϵ (energy density) and P (pressure) are scalar coefficients. w^μ represents the transverse vector coefficient. $\Delta^{\mu\nu} \equiv g^{\mu\nu} + u^\mu u^\nu$ is the projector operator orthogonal to the fluid velocity(u^μ) and $g^{\mu\nu}$ is the space-time metric. The above

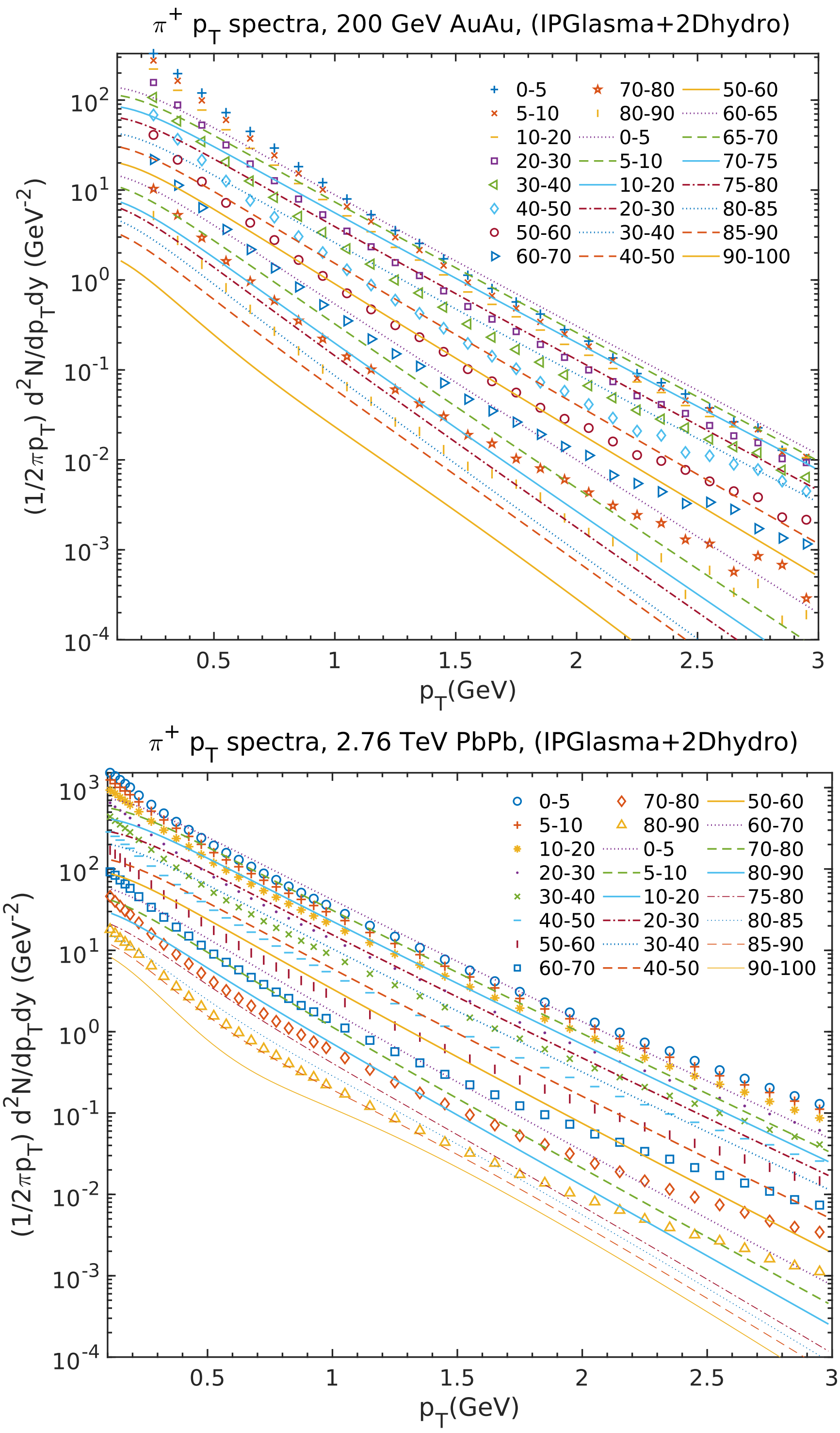

Figure 5.3: Pion(π^+) p_T-spectra generated (lines) for Au-Au at 200 GeV (left) and Pb-Pb at 2.76 TeV (right) for mentioned centrality classes compared with the corresponding PHENIX [195] and ALICE experimental results [196] (symbols).

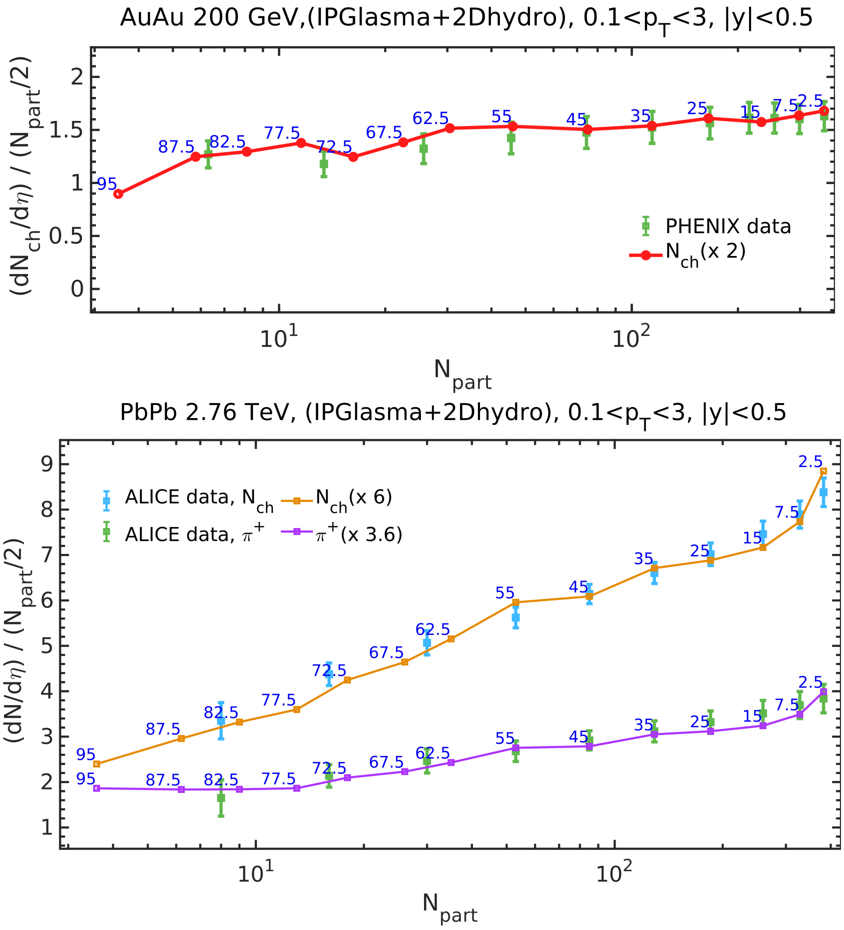

Figure 5.4: Charged particle multiplicity rapidity spectra generated (lines) for Au-Au 200 GeV (above) and Pb-Pb 2.76 TeV (below) as a function of the number of participants compared with corresponding PHENIX[195] and ALICE[197, 198] experimental data (error bars). The generated data points are labeled with the midpoint of the centrality range in blue color.

expression without the $\Pi^{\mu\nu}$ term corresponds to 0^{th} order ideal hydrodynamics. The $\Pi^{\mu\nu}$ tensor is introduced to account for the dissipative effects and is further decomposed as:

$$\Pi^{\mu\nu} = \pi^{\mu\nu} + \Delta^{\mu\nu}\Pi. \tag{5.5}$$

Π and $\pi^{\mu\nu}$ are the bulk and shear parts of the viscous stress tensor. The form of the shear stress tensor($\pi^{\mu\nu}$) and bulk pressure(Π) are set up in accordance with the covariant form of the second law of thermodynamics [172]. When we set entropy $4-$current expression as $s^\mu = su^\mu$, where s is entropy density, we get;

$$\pi^{\mu\nu} = \eta\sigma^{\mu\nu} \qquad \text{and} \qquad \Pi = \zeta\, \partial_\mu u^\mu, \tag{5.6}$$

where η (shear viscosity) and ζ (bulk viscosity) are the transport coefficients. $\sigma^{\mu\nu}$ (shear tensor) is a traceless, transverse and symmetric tensor. This form of $\pi^{\mu\nu}$ and Π leads to the 1^{st} order, Navier–Stokes theory. When we introduce perturbations in energy density and fluid velocity and evolve them, the diffusion speed obtained from the dispersion relation has a form that can increase arbitrarily. This theoretical formulation cannot be considered a satisfactory one if it violates causality. It turns out that if the term $(-\tau_\pi u^\alpha \partial_\alpha \pi^{\mu\nu})$ is added in the expression of $\pi^{\mu\nu}$ above, the resulting diffusion speed stays below the speed of light. The coefficient of this newly added term, τ_π is called *relaxation time*. But this is still a makeshift way to restore causality in the system. A good 2^{nd} order viscous hydrodynamics theory at the very least should reduce to the Navier–Stokes equation in the limit of long wavelengths, and must show causal signal propagation.

Müller [200], Israel and Stewart [201, 202](MIS) suggested modification of the entropy 4−current expression used above to include the following term with a viscous stress tensor:

$$s^\mu = su^\mu - \frac{\beta_0}{2T} u^\mu \Pi^2 - \frac{\beta_2}{2T} u^\mu \pi_{\alpha\beta}\pi^{\alpha\beta} + \mathcal{O}(\Pi^3) \tag{5.7}$$

where β_0 and β_2 are scalar coefficients. When we use this entropy 4−current in covariant 2^{nd} law of thermodynamics, the dissipative terms of energy momentum tensor take the following forms [172]:

$$\pi_{\alpha\beta} = \eta \left(\nabla_{\langle\alpha} u_{\beta\rangle} - \pi_{\alpha\beta} T u^\mu \partial_\mu \left(\frac{\beta_2}{T}\right) - 2\beta_2 u^\mu \partial_\mu \pi_{\alpha\beta} - \beta_2 \pi_{\alpha\beta} \partial_\mu u^\mu \right), \tag{5.8}$$

$$\Pi = \zeta \left(\nabla_\alpha u^\alpha - \frac{1}{2} \Pi\, T\, u^\mu \partial_\mu \left(\frac{\beta_0}{T}\right) - \beta_0 u^\mu \partial_\mu \Pi - \frac{1}{2} \beta_0 \Pi \partial_\mu u^\mu \right), \tag{5.9}$$

where, $\nabla^\mu = \Delta^{\alpha\mu}\partial_\alpha$ and $\nabla_{\langle\alpha u_\beta\rangle}$ is a symbol to represent traceless symmetrization of $\nabla_\alpha u^\beta$. A perturbative analysis with these newly obtained expressions leads to an inherently causal system. There are a few variants of this theory [203], depending on how many terms are kept in $\pi^{\mu\nu}$ and Π expression. The viscous hydrodynamics code used for this study is based on MIS theory. BRSSS theory [204] is a more comprehensive version of MIS hydrodynamics. A few 3^{rd} order versions have also been worked up [205, 206].

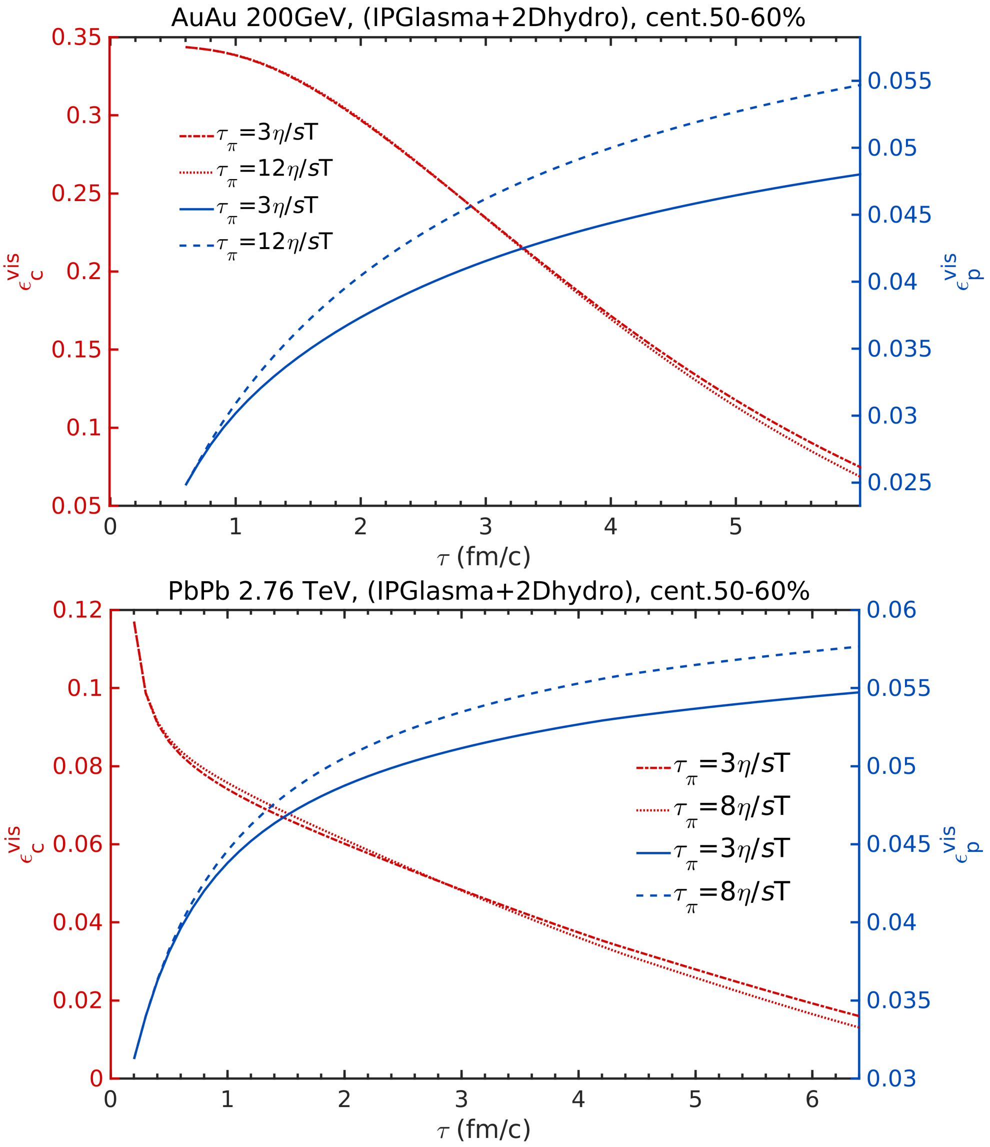

Figure 5.5: Spatial eccentricity (red) and momentum space eccentricity (blue) for the viscous case for Au-Au 200 GeV system (left) and Pb-Pb 2.76 TeV system (right) for the two mentioned relaxation times at $50-60\%$ centrality.

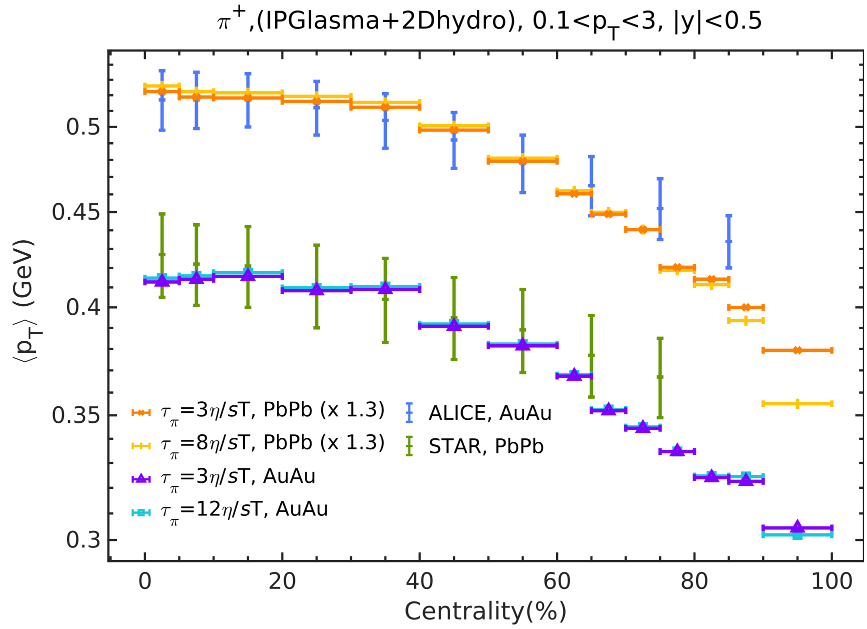

Figure 5.6: Pion mean p_T as a function of centrality for Au-Au at 200 GeV and Pb-Pb at 2.76 TeV. The corresponding experimental data for Pb-Pb from ALICE[197] and for Au-Au from STAR[207] have systematic errorbars.

The second-order viscous hydrodynamics used for this study is a publicly available code[1], ECHO-QGP [208, 209], based on MIS theory. It could be used in either $(2+1)$-D or $(3+1)$-D settings and has been utilized for bulk medium evolution in quarkonia suppression study [210]. Spacetime evolution of all $T^{\mu\nu}$ components could be extracted at the output. A tabular lattice QCD equation of state by Wuppertal-Budapest collaboration [211] has been utilized. In this equation of state, the values for energy density(ϵ), speed of sound(c_s), and pressure(P) are available starting with the temperature of 100 MeV. In order to get values below this temperature we spline interpolated temperature dependencies of quantities mentioned above with the corresponding values from hadron resonance gas model [212]. Dissipative corrections to the energy momentum tensor in ECHO-QGP are introduced in the same way as stated in Eq. (5.5). Here the evolution of the shear part of the viscous stress tensor is given by [208],

$$\pi^{\mu\nu} = -\eta\left(2\sigma^{\mu\nu} + \frac{4}{3}\frac{\tau_\pi}{\eta}d_\mu u^\mu \pi^{\mu\nu} + \frac{\tau_\pi}{\eta}\Delta^\mu_\alpha\Delta^\nu_\beta D\pi^{\alpha\beta} + \frac{\lambda_0}{\eta}\tau_\pi(\pi^{\mu\lambda}\Omega^\nu_\lambda + \pi^{\nu\lambda}\Omega^\mu_\lambda)\right) \tag{5.10}$$

Here, λ_0 is a scalar coefficient and Ω is a traceless, anti-symmetric, transverse vorticity tensor. d_μ is the covariant derivative given by $d_\mu u^\nu = \partial_\mu u^\nu + \Gamma^\nu_{\beta\mu} u^\beta$, where $\Gamma^\nu_{\beta\mu}$ are the Christoffel symbols. $D = u^\mu d_\mu$, is the comoving time derivative. The evolution of the bulk part of the viscous stress tensor is given by;

---

[1] http://theory.fi.infn.it/echoqgp/index.php

$$\Pi = -\zeta\left(d_\mu u^\mu + \frac{\tau_\Pi}{\zeta} u^\alpha d_\alpha \Pi + \frac{4}{3}\frac{\tau_\Pi}{\zeta}\Pi \, d_\mu u^\mu \right). \tag{5.11}$$

The values of the transport coefficients, τ_Π, λ_0, τ_π, η, ζ are required for solving the above two equations, which are obtained from the microscopic theory approach to hydrodynamics. τ_Π is the bulk viscosity relaxation time, which represents how quickly the above 2^{nd} order form of bulk pressure relaxes to its leading-order form in Eq. (5.6). The above two equations are derived under the metric signature choice of $(-1, +1, +1, +1)$.

5.2.1 Input parameters

The form of relaxation time has been worked out for hydrodynamics beginning from numerous microscopic theories, e.g., Boltzmann theory in the relativistic limit [202, 213], weakly coupled QCD [214] and AdS/CFT [204, 215, 216]. In ECHO-QGP, the relaxation time is introduced as:

$$\tau_\pi = \tau_{coe}\frac{\eta}{sT}. \tag{5.12}$$

The coefficient, τ_{coe} here controls the magnitude of shear relaxation time in viscous hydrodynamics. In Sec. (5.3), we see the consequence of varying this parameter on elliptic flow coefficients for Pb-Pb and AuA-u collisions. A transverse distribution of participating nucleons could serve as an initial condition for hydrodynamics. ECHO-QGP has an optical Glauber model as its default initial condition which assumes independent linear trajectories of nucleons in nuclei that are distributed according to Wood-Saxon distribution [217, 218]. Wood-Saxon distribution has a smooth plateau for the nucleus which decays softly towards the edges. Even though the Glauber model does not involve early-stage dynamics and fluctuations of any kind, it is still a good approximation nonetheless.

IPGlasma [219, 220] is a more realistic initial condition that includes the dynamics beginning from the moment of collision. It is based on the color glass condensate framework. The wavefunction of a nucleus or hadron at high energy could be explained with the effective theory of color glass condensate [221, 222]. In the IPGlasma model, the color charges inside the nucleons are Gaussian sampled and are taken as the source for gluon fields, which are then evolved using classical Yang-Mills equations [219]. We have used the publicly available[1] IPGlasma model that describes a boost invariant (2+1)-D initial state. The energy density in the transverse plane at $\tau_{start} = 0.2$ fm/c for Pb-Pb collision and $\tau_{start} = 0.6$ fm/c for Au-Au collision has been taken as an input for ECHO-QGP. Fig.(5.2) shows the initial energy densities for 14 centralities as a function of transverse coordinates for Au-Au collision. We ran the [IPGlasma initial condition + ECHO-QGP hydrodynamics] framework for 14 centrality values, with more values near peripheral collisions.

The distribution of the nucleons in the nucleus and the distribution of color charge inside nucleons are the key sources of initial state fluctuations in each collision event. Observables in collider experiments are averaged over a large number of collision events, to account for this event-by-event fluctuation. For both Au-Au and Pb-Pb collision systems, we produce an initial state with 400 different sets of nucleon positions that are then combined into one. The total inelastic nucleon-nucleon cross section is set to 61.8 mb for Pb-Pb system and 42 mb for the Au-Au system in both, IPGlasma and hydrodynamics, taken from Monte Carlo Glauber analysis [223]. Shear viscosity to entropy density ratio(η/s) is taken as a constant, 0.1 ($\approx 1.25 \times \frac{1}{4\pi}$) [158], which is above the theoretical minimum KSS limit [224]. Bulk viscosity has not been included in this study. The pseudo-critical temperature, at which quarks to hadron phase transition occur, has been calculated by various lattice QCD collaborations, is an input parameter. It is set to the recently calculated value of 156 MeV [225]. Chemical freezeout is a point at which the inelastic scatterings cease to exist between produced hadrons. This point is decided by the temperature, which in the present model is fixed at 150 MeV [226].

5.2.2 Fixing centrality parameters

Fig. (5.3) shows the p_T spectra of pions(π^+) produced for the two mentioned collision systems along with corresponding experimentally measured p_T spectra. The generated spectra adequately comply with experimental values only in the low p_T regime, where the hydrodynamic mode operates. The energy density profile plotted as a function of transverse coordinate from IPGlasma had to be scaled before being used in hydrodynamics. Fig. (5.2) shows this scaled energy density distribution. This fixed the energy density scaling parameter such that the produced p_T spectra and the maxima of rapidity spectra(dN/dy) at each centrality matches the corresponding experimental measured data for both collision systems.

---

[1] https://github.com/schenke/ipglasma

Fig. (5.4) shows rapidity spectra normalized to $N_{part}/2$ as a function of N_{part}. In addition to energy density scaling, the rapidity spectra had to be scaled to match experimental results, as shown in Fig. (5.4). For the Au-Au system, charged particle normalized rapidity spectra were scaled up by a factor of 2, whereas for Pb-Pb system, this scaling was 6, and the corresponding scaling used for pions was 3.6. We chose a centrality range spaced by 5% in peripheral collisions except for the last centrality class, 90-100%. The impact parameter and N_{part} values for all of these centrality ranges are taken from a Monte Carlo Glauber analysis [223]. The reason for taking more values towards the peripheral side was to capture fine variations of flow for decreasing dN/dy as could be seen in Fig. (5.10) in Sec. 5.3. However there was no experimental reference to set parameters for these in-between centrality values for p_T-spectra and dN/dy vs N_{part} plot. Hence, we selected two values around each experimental centrality point starting from 60% as could be seen in dN/dy vs N_{part} plot (Fig. 5.4). There was no experimental point at 90-100% so we settled with just one extrapolated value which follows the trend of data. The blue labels on data points in Fig. (5.4) are the mid-centrality value of that data point. For calculating observables for charged particles, we have added the corresponding values for the pions(π^++π^-), kaons(K^++K^-) and protons(p^++p^-) since these are abundantly produced species in high energy collisions. Momentum space eccentricity, which is the precursor of elliptic flow, can be calculated in terms of $T^{\mu\nu}$ components as:

$$e_p \equiv \frac{\int d^2x_\perp (T^{xx} - T^{yy})}{\int d^2x_\perp (T^{xx} + T^{yy})}. \tag{5.13}$$

ECHO-QGP calculates this quantity for the ideal hydrodynamic case, which takes the form:

$$e_p \equiv \frac{\int d^2x_\perp \left(u^x u^x - u^y u^y\right)(\epsilon + P)}{\int d^2x_\perp [2P + (\epsilon + P)\left(u^x u^x + u^y u^y\right)]} \tag{5.14}$$

To generate momentum eccentricity for the viscous case, we have modified the above expression by adding the viscous component term, $(\pi^{xx} + \pi^{yy})$ to the integrand in both numerator and denominator.

Fig. (5.5) shows spatial eccentricity(ϵ_c), and momentum space eccentricity(ϵ_p)

for Au-Au and Pb-Pb collision, generated at $50-60\%$ centrality for the two mentioned shear relaxation times. Momentum anisotropy quantified by momentum eccentricity increases at the expense of spatial anisotropy quantified by spatial eccentricities along the evolution[171]. The variation in non-hydrodynamic mode decay time seems to have a negligible effect on spatial eccentricity. The distinguishing feature between the two systems is that the early time ϵ_c for Pb-Pb decreases more rapidly than that for Au-Au collisions. Below the pseudo-critical temperature, the hadronic picture should emerge. Particles of various species are assigned momentum according to Cooper–Frye scheme [227]. The resulting momentum spectrum is then used to calculate the elliptic flow, $v_2 = \langle \cos[2(\phi - \Psi_{\mathrm{RP}})] \rangle$, where Ψ_{RP} is the reaction plane angle which acts as a reference plane and ϕ is the transverse plane angle for a given particle with respect to the reaction plane.

Fig. (5.6) shows the average transverse momentum evolution as a function of centrality. Results for the two values of shear relaxation time have been plotted and compared with experimental values for pions. We notice, that the model show agreement with experimental values for most of the centrality classes apart from the peripheral ones. The values for Pb-Pb collisions had to be scaled up by a factor of 1.3. This could be due to the underproduction of hadrons in the hydrodynamics because the multiplicity has been used as the weight factor for calculating mean p_T.

5.3 Flow results and discussion

5.3.1 Elliptic flow results for Au-Au and Pb-Pb collision systems

Romatschke [178] has put forth a quantitative test for the applicability of hydrodynamics by checking the sensitivity of certain observables (like elliptic flow) to the non-hydrodynamic mode. The idea is that hydrodynamics can be used to describe a system if the non-hydrodynamic mode is sub-dominant and there exists a local rest frame. With QCD as the microscopic theory, the approximate transverse momentum range of hydrodynamic mode is 3 to 7 GeV. Fig. (5.8) illustrates this p_T range where hydro and non-hydro modes operate.

This is what we have tried checking for Au-Au 200 GeV in Fig. (5.7) and for

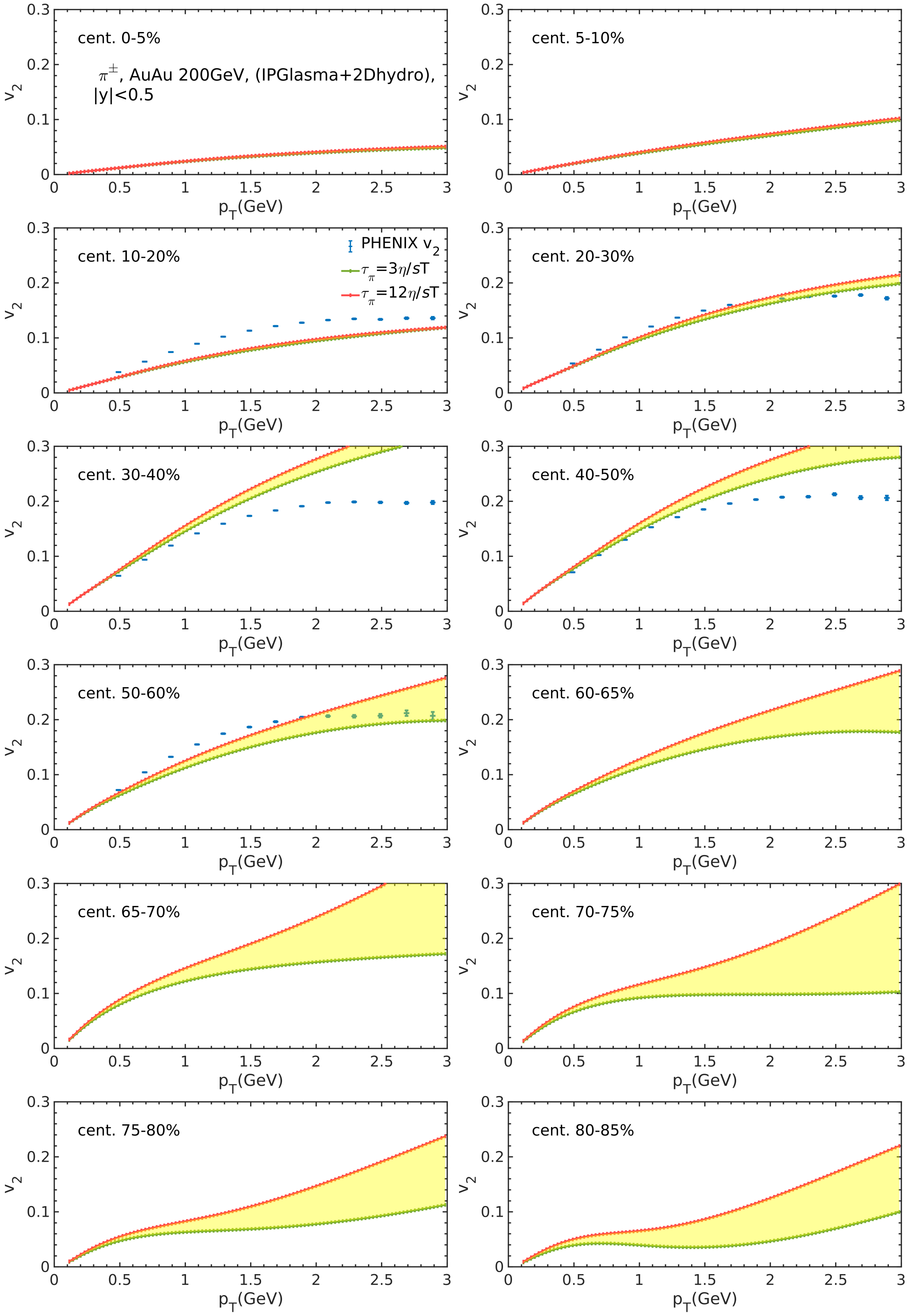
cent. 0-5%
$\pi^{\pm}$, AuAu 200GeV, (IPGlasma+2Dhydro), |y|<0.5
cent. 5-10%
cent. 10-20%
PHENIX v_2
$\tau_\pi=3\eta/sT$
$\tau_\pi=12\eta/sT$
cent. 20-30%
cent. 30-40%
cent. 40-50%
cent. 50-60%
cent. 60-65%
cent. 65-70%
cent. 70-75%
cent. 75-80%
cent. 80-85%
v_2
p_T(GeV)
0
0.1
0.2
0.3
0.5
1
1.5
2
2.5
3

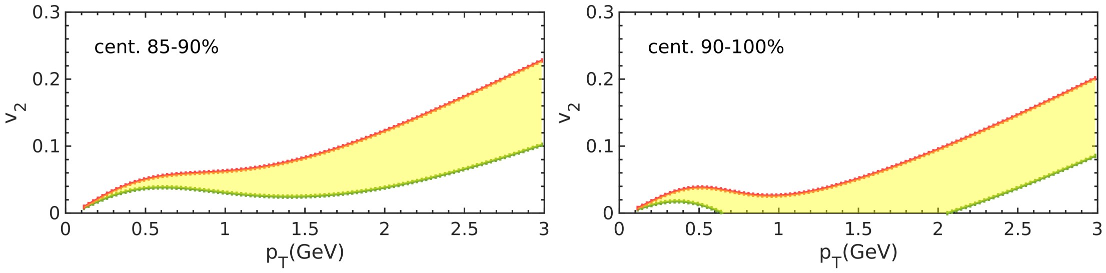

Figure 5.7: Pion(π^+) elliptic flow coefficient(v_2) as a function of transverse momentum(p_T) for 14 centrality classes for Au-Au 200 GeV system obtained with (IPGlasma+2Dhydro) set up along with experimentally measured elliptic flow (blue) from PHENIX [228] for the relaxation/non-hydrodynamic mode decay time, $\tau_\pi = 3\eta/sT$ (green) and $12\eta/sT$(red). The shaded area (yellow) highlights the difference in flow due to variations in relaxation time.

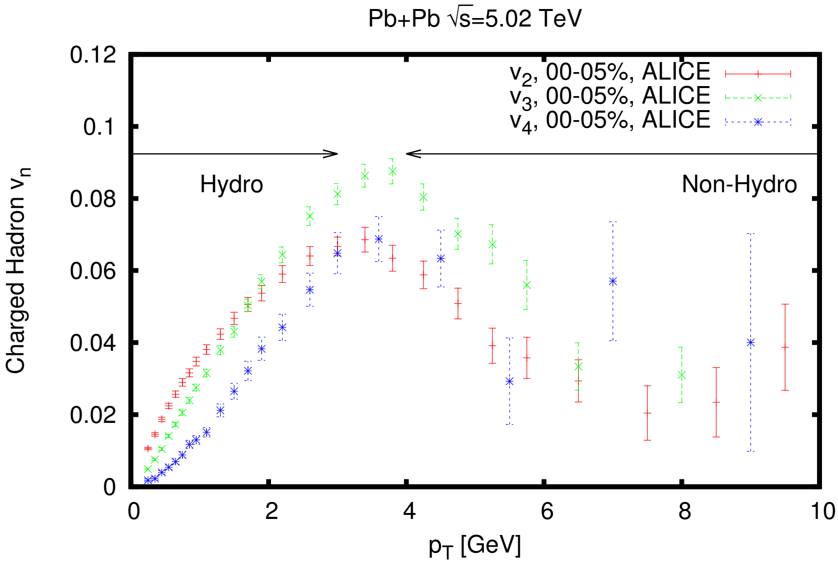

Figure 5.8: Experimental values of flow coefficients as a function of transverse momentum. Plot taken from [178]. Phenomenological studies that make use of viscous hydrodynamics have been able to explain flow experimental data only in the low p_T range. Beyond $p_T \approx 4$ GeV, the presence of a non-hydrodynamic mode has been suggested.

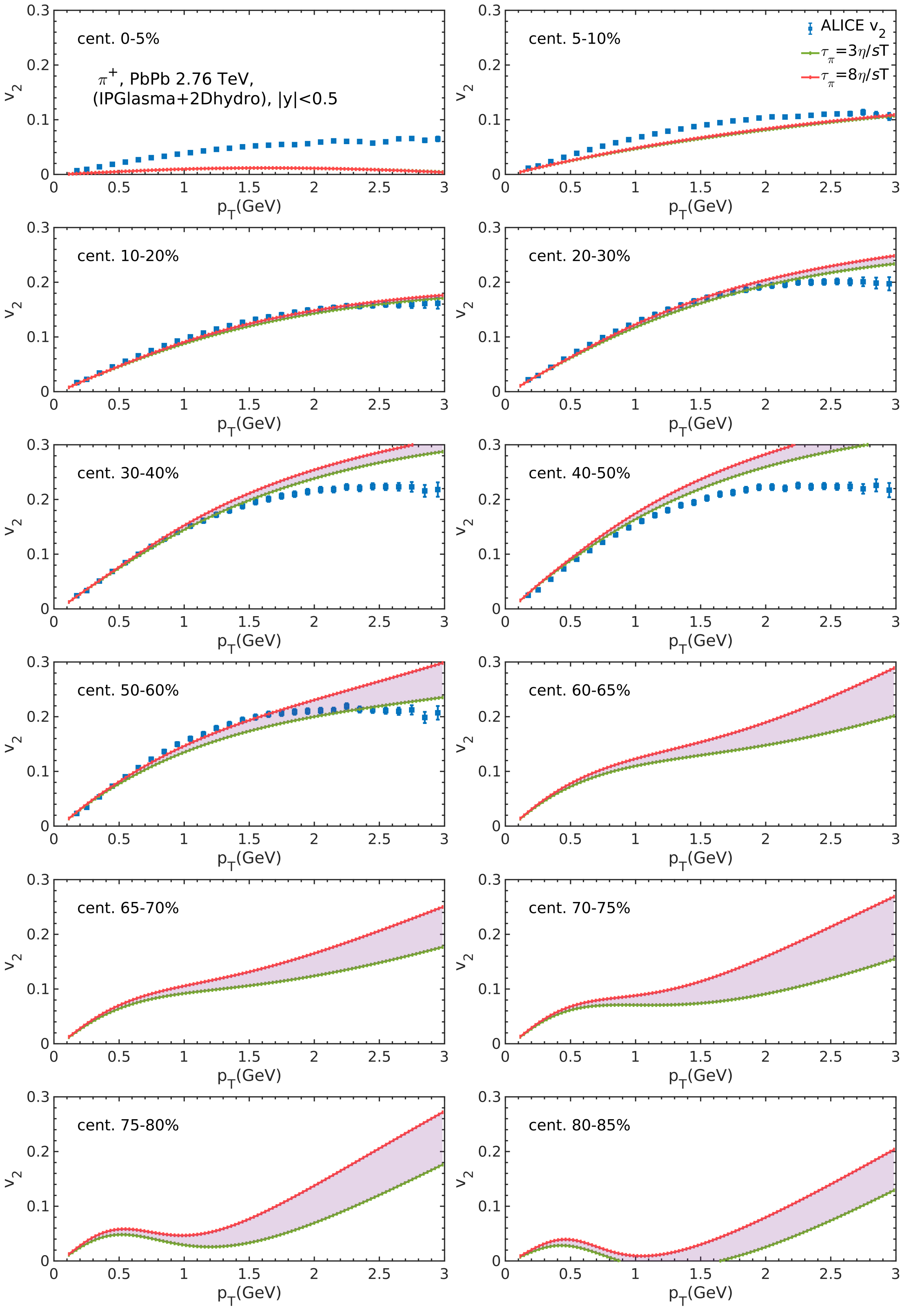
cent. 0-5%
π^+, PbPb 2.76 TeV,
(IPGlasma+2Dhydro), |y|<0.5
cent. 5-10%
ALICE v_2
$\tau_\pi=3\eta/sT$
$\tau_\pi=8\eta/sT$
cent. 10-20%
cent. 20-30%
cent. 30-40%
cent. 40-50%
cent. 50-60%
cent. 60-65%
cent. 65-70%
cent. 70-75%
cent. 75-80%
cent. 80-85%
v_2
p_T(GeV)
0
0.1
0.2
0.3
0.5
1
1.5
2
2.5
3

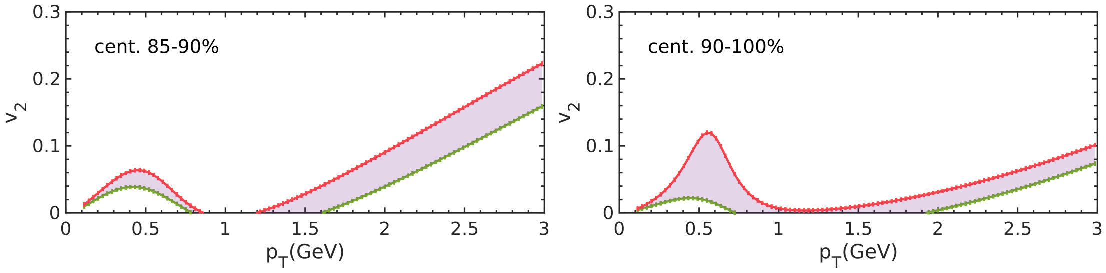

Figure 5.9: Pion(π^+) elliptic flow coefficient as a function of transverse momentum(p_T) for 14 centrality classes for Pb-Pb 2.76 TeV collision system obtained with (IPGlasma+2Dhydro) setup along withe elliptic flow measured at ALICE[229] (blue) for relaxation time $\tau_\pi = 3\eta/sT$(green) and $8\eta/sT$(red). The shaded area (violet) highlights the difference in flow due to variations in relaxation time. See the text for an explanation.

Pb-Pb 2.76 TeV in Fig. (5.9). Peripheral collisions are the system of interest but experimentally measured anisotropic flow results are only available up to 50-60% centrality class. We hence presented the results for the complete centrality range. In Fig. (5.7), for 0-5%, 5-10%, and 10-20% centralities, we see no separation between elliptic flow curves for non-hydrodynamic mode decay times, $\tau_\pi = 3\eta/sT$ and $12\eta/sT$. From 20-30% centrality class onwards we notice the separation between these two flow curves to be increasing. Experimental data has been plotted just for reference which shows our results are quite close to experimentally measured flow results. The important point to notice is that along increasing centrality, the point at which the two flow curves separate shifts towards lower p_T values. This means that with increasing centrality and decreasing system size, the hydrodynamic mode is shrinking, and the non-hydrodynamic mode is getting dominant. Hence in a way, we are witnessing the limit of applicability of low-order hydrodynamics for decreasing system size at constant collisional energy(here, 200 GeV).

5.3.2 Elliptic flow results for varying shear relaxation time

Fig. (5.9) shows p_T dependence of pion(π^+) elliptic flow with complete centrality range for $\tau_\pi = 3\eta/sT$ and $8\eta/sT$. We notice all the structures mentioned above for Au-Au, 200 GeV system. We notice a better match between produced elliptic flow and experimental data 10-20% onwards. We chose pions for this analysis because they are the lightest of particle species produced and hence adequately represent the bulk medium. One additional point to notice is, for $10-20\%$ centrality in Au-Au collisions and classes $0-5\%$, $5-10\%$ in Pb-Pb collision system, our model fails to reproduce the measured elliptic flow data.

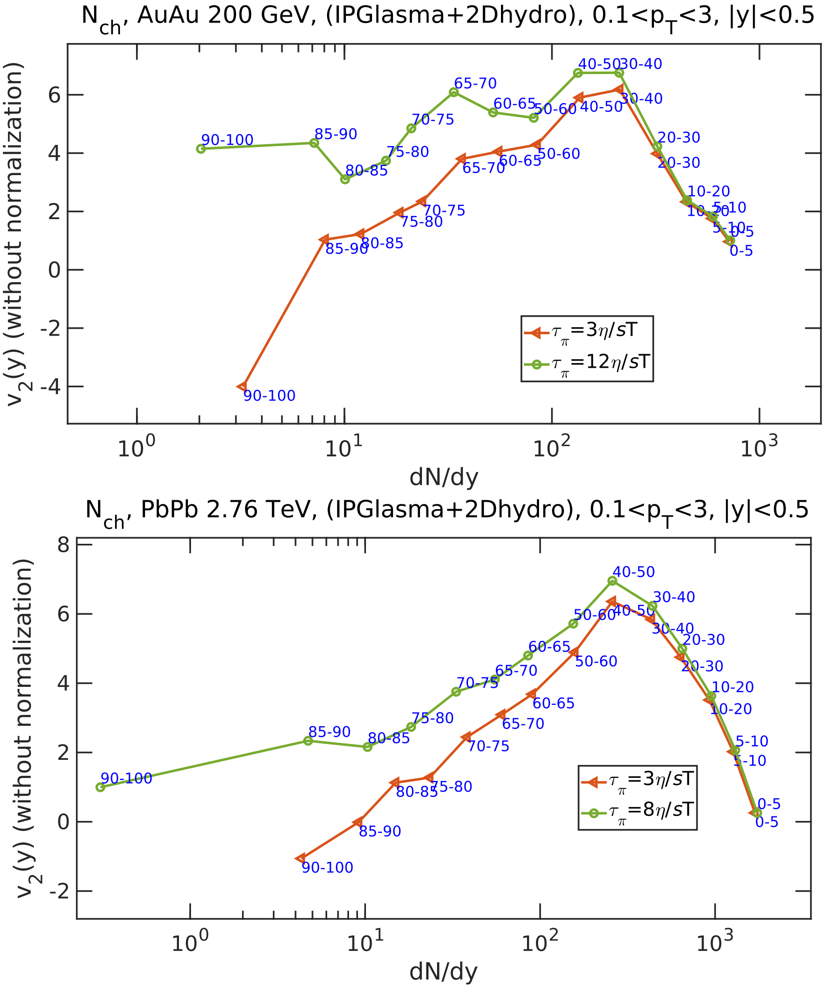

Figure 5.10: Un-normalized p_T integrated elliptic flow of charged particles as a function of N_{ch} rapidity density for Au-Au 200 GeV (left) and Pb-Pb 2.76 TeV (right) plotted for the two mentioned relaxation times. Data points are labeled by the centrality values. The separation between the two curves is better seen for the un-normalized elliptic flow than for the normalized one shown below.

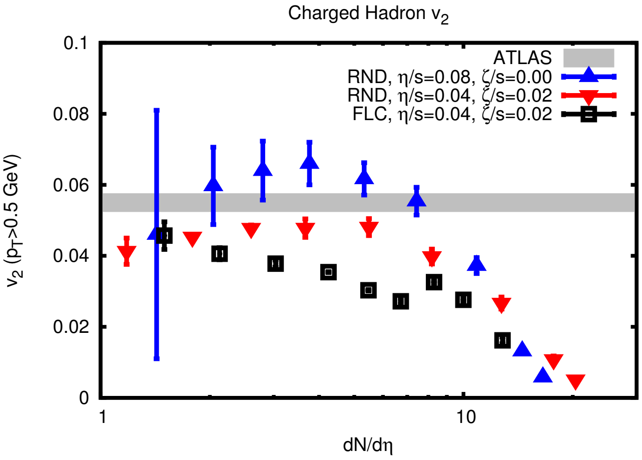

Figure 5.11: p_T integrated elliptic flow in *proton-proton* collision at 7 TeV produced using SONIC model, as a function of multiplicity pseudorapidity spectra for the mentioned values of η/s and ζ/s. For $\eta/s = 0.08$ and $\zeta/s = 0$ (blue), the elliptic flow has an errorbar due to variation in shear relaxation or non-hydro mode decay time, which increases in size for decreasing $dN/d\eta$. Plot taken from [178].

Fig. (5.11) depicts the criteria suggested by Romatschke to check the applicability of hydrodynamics. This figure shows charged particle's elliptic flow as a function of multiplicity pseudorapidity density for proton-proton collision. The error bar depicts the abrupt change in flow due to variations in non-hydrodynamic mode decay time. This abrupt change in elliptic flow is indicative of the breakdown of hydrodynamics, and it is seemingly happening at roughly $dN/d\eta < 2$ in Fig. (5.11). We tried checking this feature in our (IPGlasma+2Dhydro) analysis as shown in Figs. (5.12) and (5.10).

5.3.3 Transverse plane system evolution results

Fig. (5.10) presents the un-normalized p_T integrated elliptic flow as a function of multiplicity rapidity density(dN/dy). The data points from our analysis are labeled by the centrality class in order to track the point at which flow changes abruptly between the relaxation time curves. This is why we selected more centrality points in the peripheral collision side. We notice a steady increase in separation between the two flow curves for both Au-Au and Pb-Pb systems which is in reasonably close agreement with Romatschke's work.

We also notice that the two relaxation time flow curves of the same centrality

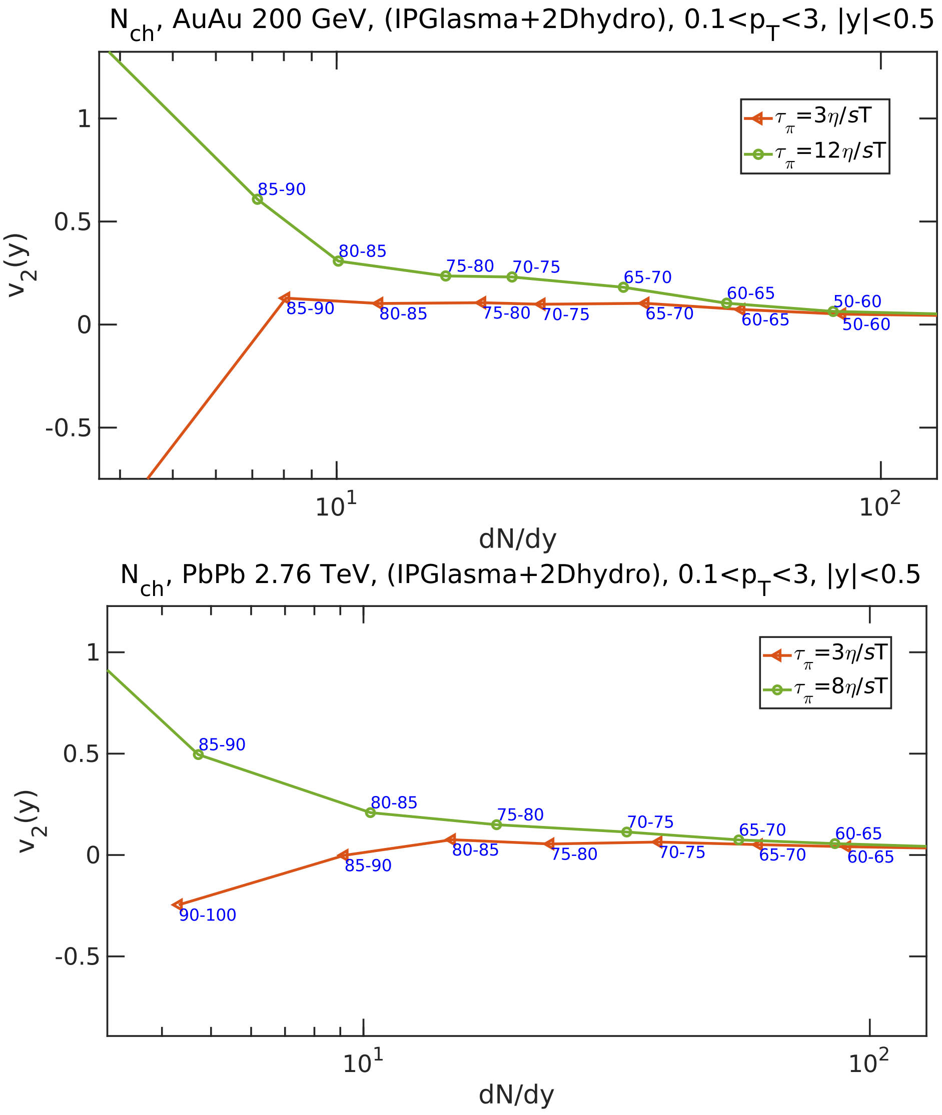

Figure 5.12: p_T integrated elliptic flow of charged particles as a function of N_{ch} rapidity density for Au-Au 200 GeV (left) and Pb-Pb 2.76 TeV (right) plotted for the two mentioned relaxation times. Data points are labeled by the centrality values. See the text for an explanation.

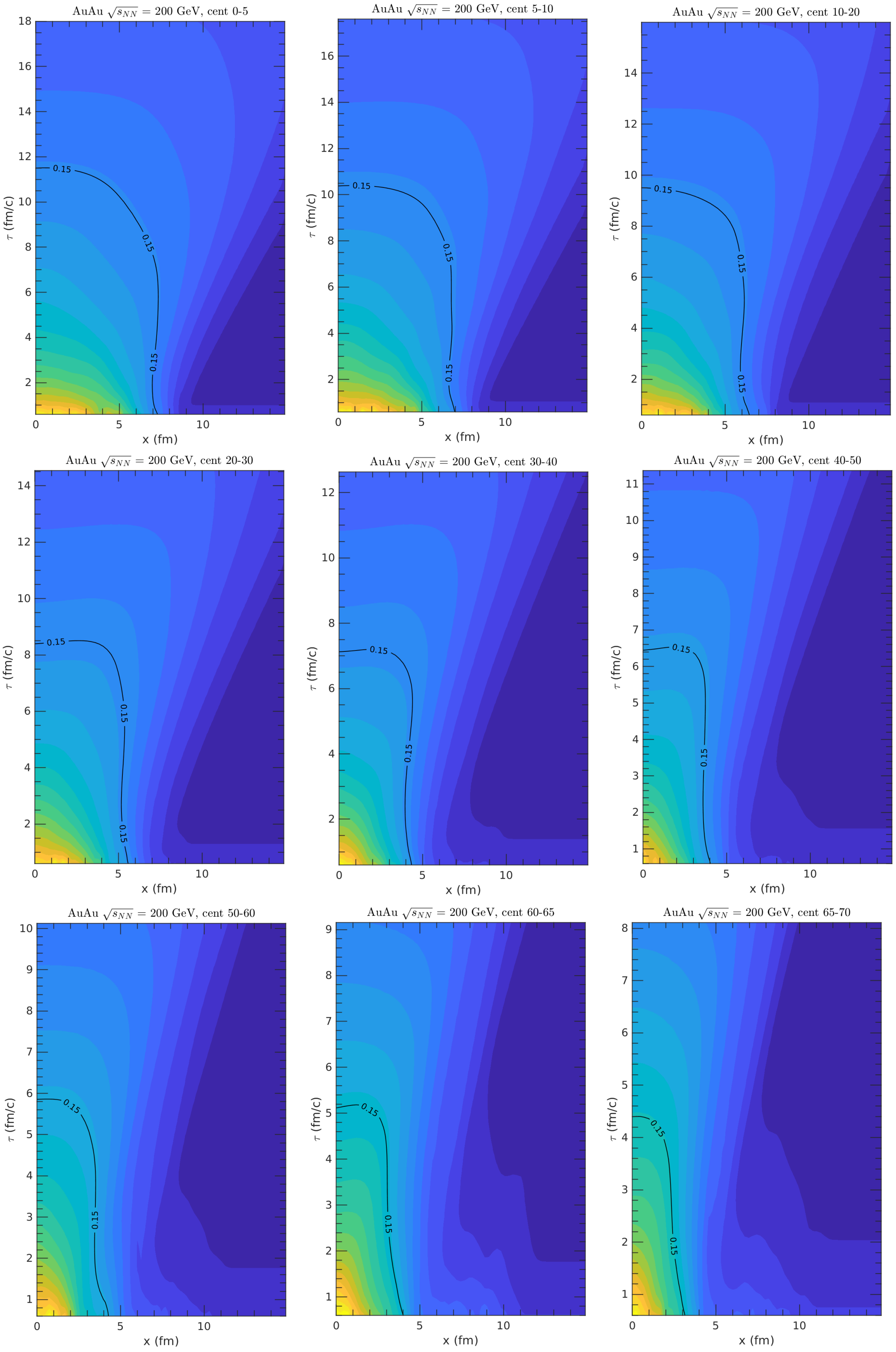

AuAu $\sqrt{s_{NN}}$ = 200 GeV, cent 0-5

AuAu $\sqrt{s_{NN}}$ = 200 GeV, cent 5-10

AuAu $\sqrt{s_{NN}}$ = 200 GeV, cent 10-20

AuAu $\sqrt{s_{NN}}$ = 200 GeV, cent 20-30

AuAu $\sqrt{s_{NN}}$ = 200 GeV, cent 30-40

AuAu $\sqrt{s_{NN}}$ = 200 GeV, cent 40-50

AuAu $\sqrt{s_{NN}}$ = 200 GeV, cent 50-60

AuAu $\sqrt{s_{NN}}$ = 200 GeV, cent 60-65

AuAu $\sqrt{s_{NN}}$ = 200 GeV, cent 65-70

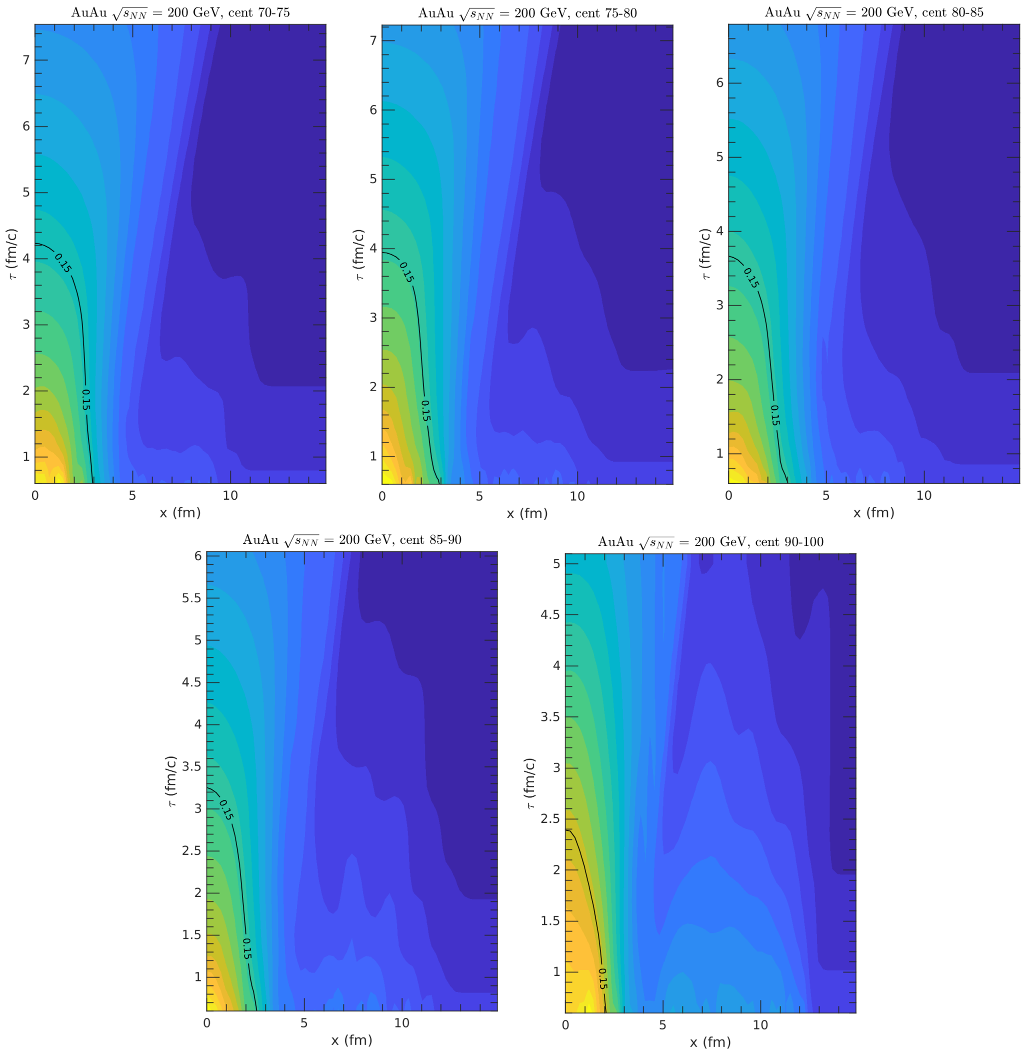

Figure 5.13: Temperature contours as a function of coordinate x and proper time tau for Au-Au collisions at 200 GeV energy for decreasing impact parameter of collision. The temperature contour which roughly marks the pseudo-critical temperature is highlighted. We can notice the decreasing system size and corresponding lifetimes. From Figs. (5.12) and (5.10), the abrupt separation between the two flow curves begins roughly at the centrality bin 80-85%. One can qualitatively associate the actual spacial extension of a system at this centrality bin with the temperature contour of this centrality, and hence the smallest system size that can hydrodynamize.

do not have the same multiplicity rapidity density value (the x coordinate). This would mean, that for an increase in relaxation time, flow shifts to a lower multiplicity value. We also notice that the flow for $\tau_\pi = 3\eta/sT$ for both, Au-Au and Pb-Pb systems, acquire negative values, which is also apparent from the elliptic flow for 90-100% centrality class in Figs. (5.9) and (5.7).

Fig. (5.12) shows normalized p_T integrated elliptic flow as a function of charged particle multiplicity rapidity density(dN/dy) for peripheral collisions. We clearly notice the sudden increase in the separation of flow curves for the two mentioned relaxation times for both collision systems. But we don't have a centrality resolution good enough to decide the onset of hydrodynamization. An approximate limit we can deduce from Fig. (5.12) is $dN/dy \approx 10$ which is quite larger than the prediction of $dN/d\eta < 2$ [179, 189]. However, if the hadron resonance gas to de-confined quarks transition in high temperature regime is a crossover, we expect to find a region where the analysis would be indecisive like what Aleksi Kurkela *et al.* obtained [188, 230]. The problem lies in the absence of experimental reference data to set the scaling parameter of IPGlasma for such high centrality classes.

5.4 Summary

In this study we analyze the non-hydrodynamic mode in an attempt to find the onset of hydrodynamization in peripheral collision system of Au-Au and Pb-Pb at 200 GeV and 2.76 TeV center of mass per energy nucleon, respectively. We use the energy density profile from *color glass condensate* based IPGlasma model as the initial condition in 2D ECHO-QGP which is a 2^{nd} order viscous hydrodynamic code based on MIS theory. p_T spectra and multiplicity rapidity density($dN/dy/(N_{part}/2)$) as a function of N_{part} is used to constrain the centrality scaling parameter of IPGlasma. Mean p_T as a function of centrality, evolution of spatial and momentum eccentricity has also been generated for both the systems. The shear viscosity to entropy density ratio is set as $\eta/s = 0.1$ and bulk viscosity has not been considered in this work. We study the variation in the strength of non-hydrodynamic mode through the shear relaxation time, whose value is set to $(3-12)\eta/sT$ for Au-Au system and $(3-8)\eta/sT$ for Pb-Pb system. Elliptic flow generated as a function of p_T is compared with 2^{nd} anisotropic flow coefficient from experiments for the above respective values of relaxation time, for all of the 14 centrality classes. Normalized and un-normalized p_T integrated elliptic flow has been studied as a function of multiplicity rapidity density in peripheral collisions especially.

Chapter 6

Concluding discussion and outlook

6.1 Study on bottomonium suppression

The problem of explaining bottomonium suppression comprehensively was addressed in Chapter 3. An attempt has been made to explain the nuclear modification factor with centrality (N_{PART}), transverse momentum (p_T), and rapidity (y) dependences at LHC energies of 2.76 TeV and 5.02 TeV. For this, the QGP medium of light quarks was simulated with a $(3+1)$-dimensional hydrodynamics as background for bottomonium. The temperatures at different centralities and rapidities have been extracted from the ECHO-QGP and were used in the suppression formalism. The experimental data on transverse momentum(p_T), rapidity(y) spectra, and elliptic flow of pions have been utilized to fix the input parameters of the hydrodynamics. The equation of state used was from the Wuppertal-Budapest Lattice QCD collaboration interpolated with Hadron Resonance Gas model EoS for low temperatures. We considered the dissociation of bottomonium due to collisional damping, gluonic dissociation, color screening, and shadowing effects. A modified color screening formalism has been used, which eliminates the need to assume a pressure profile for collisions in the transverse plane. The shadowing effect has been updated with the recent gluon PDFs and shadowing factors. Parameters entering the model for quarkonia and hydrodynamics are based on previous studies in a similar context and are not varied freely. The uncertainty in temperature integration from ECHO-QGP has translated into an uncertainty patch in the final suppression results. Using this current framework of quarkonium suppression of $\Upsilon(1S)$ and $\Upsilon(2S)$ based on color screening, gluonic dissociation, and collisional damping with full (3+1)-dimensional hydrodynamics, we are able to explain all three dependencies of measured quarkonium suppression namely, centrality, transverse momentum, and rapidity at 2.76 TeV and 5.02 TeV for Pb-Pb collisions with a reasonable agreement, although with some mismatch for $\Upsilon(1S)$ rapidity dependent suppression.

6.2 Outlook

Looking ahead, it will be interesting to do an open heavy flavor mesons evolution study in the QGP medium with a formalism suited well for such heavy-light mesons. We have also performed a study where we made a crude assumption of using the quarkonia suppression formalism presented in Ref. [100] for open heavy flavor with satisfactory results. A simultaneous study of open and hidden heavy flavor will give a more reliable constraint on the model parameters since it will account for suppression for all heavy quarks bound states produced in the collisions. Along with this, we would like to study the effect to supposedly present large magnetic fields in heavy-ion collisions on quarkonia transport, which we are trying to do in our subsequent study. Considering the question of QGP in small systems, it will be interesting to use this formalism for *proton-nucleus* collision and high multiplicity *proton-proton* collision. Apart from this, it is important to quantify the contribution of CNM and hot matter effects, especially in small systems.

6.3 Study on hydrodynamic applicablity

In the study presented in Chapter (5), we tried to address the pressing question of how small the hot quark medium can get. With so many signatures pointing to the formation of QGP in small systems, it has become crucial to find the onset of QGP in high energy collisions as a function of system size and collisional energy. And the presented study was a small attempt in this direction. From the results obtained, we make the following concluding comments:

- From p_T dependence of elliptic flow across centralities for AuAu (in Fig. 5.7) and for Pb-Pb (in Fig. 5.9), we found that the shear relaxation time does control the non-hydrodynamic mode of the system as predicted by P. Romatschke. This inference was guided by the observation that the point after which the flow for the two relaxation times separate sharply from each other shifts to lower p_T values for increasing centrality classes (or decreasing system size at constant energy of collision).

- We later attempted testing the onset of hydrodynamization from charged particle multiplicity rapidity density dependence of p_T integrated elliptic flow. We did notice an abrupt increase in flow for decreasing system size or the number of participants, indicating increased dominance of non-hydrodynamic mode and simultaneous breakdown of hydrodynamic description. However, we could not resolve the dN/dy below the value of 10 enough to decide the onset point quantitatively. But our analysis does serve as a proof of concept.

- We found a good agreement between the generated p_T dependence of elliptic flow results and the measured flow data from PHENIX and ALICE Collaborations for AuAu and PbPb systems, respectively, except near most centrality of 10-20% class for AuAu collisions and of 0-5% and 5-10% class for PbPb collisions.

6.4 Outlook

There is significant scope for improving this framework further by including an after-burner stage that will incorporate hadron resonance decays and scattering, which could affect the generated flow[231]. A more appropriate way of analyzing flow is in the modern flow vector method, and also one should account for non-flow effects, which become dominant at small multiplicities. It will be interesting to compare the smallest fluid size with other equivalent methods in future work. The initial state involvement could also be improved by using more components of $T^{\mu\nu}$ in hydrodynamics [232, 233]. One can also switch to 3−D IPGlasma initial condition [234]. Bulk viscosity has been kept at zero in this study. However, it does play a significant role in evolution [235]. The relaxation times for bulk viscosity could be independently analyzed. It will be interesting to see if elliptic flows of different particle species diverge for decreasing rapidity spectra at different points. If they do so, it will support the idea of a multiple-fluid scenario in heavy ion collision. This study could be extended to small and lower energy systems where the net-baryon potential is non-zero, for which particle current conservation should be included[236]. In a recent study, Plumberg *et al.* [237], conducted a causality analysis of each fluid cell of hydrodynamics for its complete evolution. They found causality being violated of non-hyperbolic($v^2 < 0$) and superluminal($v^2 > c^2$) types at early times in evolution. This violation is significantly reduced if a pre-equilibrium stage like KøMPøST [238] is used. It will be interesting to see the repercussions of such a study on the onset of hydrodynamization.

Appendix A - Open heavy flavor suppression in Pb-Pb collision at $\sqrt{s_{NN}}$ =2.76 TeV

Quarkonium suppression in relativistic heavy-ion collisions is a prominent signature of the Quark-Gluon Plasma (QGP) formation [72]. There have been many attempts to theoretically reproduce the suppression of quarkonia that has been observed in heavy-ion collisions [239]. At energies greater than twice the rest masses of heavy quarks, pair production happens due to hard scattering at the point of collision. Some of these heavy quarks (anti-quarks) form quarkonia immediately, and the rest drifts apart along with the medium. Most of these drifting heavy quarks (anti-quarks) combine with lighter quarks (anti-quarks) to form heavy-light mesons like D^0, B^0, etc. A suppression model has been developed over some time by our group to explain quarkonia suppression. Here we employ this model to reproduce open flavor suppression data with minor modifications. We usually consider the simplified picture where the complete QGP hadronizes at a single instance. This is not necessarily true. We could have different species of hadrons forming at different times due to the crossover nature of phase transition. So, we make an assumption here that D^0, like heavy-light mesons, can form during the evolution of QGP. Our present formulation is based on a model consisting of suppression due to color screening, gluonic dissociation, along with collisional damping. We estimate here the net D^0 meson suppression in terms of survival probability, which is a theoretically equivalent quantity for experimentally measured Nuclear Modification Factor (R_{AA}). We mainly concentrate here on the centrality and transverse momentum dependence of R_{AA} for D^0 meson's suppression in Pb-Pb collisions at mid-rapidity. We compare the survival probability thus obtained for D^0 suppression with the corresponding experimentally measured R_{AA} at the LHC center of mass energy of 2.76 TeV. In the section below, we have given a very brief overview of the precursor suppression model [100] followed by results.

A.1 (Precursor) Suppression formalism

The model employed here has been modified over the years and has been used to analyze suppression data of quarkonia and its excited states from RHIC to LHC for AA, and pA collision at various energies [100–102, 240]. Considering heavy quark like charm being pair produced at the hard scattering of heavy-ion collision, we model the quarkonia evolution in this system using the following rate equation first proposed by Thews [135]:

$$\frac{N_{D^0}}{d\tau} = \frac{\Gamma_{F,nl} N_c N_{\bar{u}}}{V(\tau)} - \Gamma_{D,nl} N_{D^0}, \tag{1}$$

where N_{D^0} is the number of D^0 at a given time. The first term on the right hand side of the above equation is the formation term for the new meson. $\Gamma_{F,nl}$ is the formation rate calculated in Sec. (A.2) below; N_c and $N_{\bar{u}}$ are the number of charm quark and up anti-quark respectively available at the initial time. $V(\tau)$ is the volume of fireball. The second term on the right hand side is the dissociation term for D^0, and $\Gamma_{D,nl}$ is the corresponding dissociation rate. This differential equation could be solved under the approximation that $N_{D^0} < N_c$,$N_{\bar{u}}$. The solution is expressed as:

$$\begin{aligned} N_{D^0}(\tau_{QGP}, b, p_T) = \epsilon(\tau_{QGP}, b, p_T) \Bigg[N_{D^0}(\tau_0, b) \\ + N_c N_{\bar{u}} \int_{\tau_0}^{\tau_{QGP}} \frac{\Gamma_{F,nl}(\tau, b, p_T)}{V(\tau, b)\epsilon(\tau, b, p_T)} d\tau \Bigg], \end{aligned} \tag{2}$$

where, τ_{QGP} is the lifetime of QGP medium, $N_{D^0}(\tau_{QGP}, b, p_T)$ is the final number of D^0 produced. The initial number of D^0 is calculated as:

$$N_{D^0}(\tau_0, b) = \sigma_{D^0}^{NN} T_{AA}(b), \tag{3}$$

where, σ is the production cross section of D^0 at 2.76 TeV [241]. $T_{AA}(b)$ is the nuclear overlap function whose value is obtained from [242–244]. $\epsilon(\tau_{QGP}, b, p_T)$ and $\epsilon(\tau, b, p_T)$ in Eq. (2) above are the decay factors calculated as:

$$\epsilon(\tau_{QGP}, b, p_T) = exp\left(- \int_{\tau'_{nl}}^{\tau_{QGP}} \Gamma_{D,nl}(\tau, b, p_T) d\tau \right) \tag{4}$$

and

$$\epsilon(\tau, b, p_T) = exp\left(- \int_{\tau'_{nl}}^{\tau} \Gamma_{D,nl}(\tau', b, p_T) d\tau' \right). \tag{5}$$

Following is the temperature cooling equation from the Quasi Particle Model (QPM) EOS that we used in our calculation [111]:

$$T(\tau, b) = T_c \left(\frac{N_\beta}{N_{\beta_0}} \right)^{\frac{1}{3}} \left[\left(\frac{\tau}{\tau_{QGP}} \right)^{\frac{1}{R}-1} \left(1 + \frac{a}{b' T_c^3} \right) - \frac{a}{b' T_c^3} \right]^{\frac{1}{3}} \tag{6}$$

The D^0 dissociation and recombination mechanisms used in our formalism are described briefly below.

Color screening

The screening of color charge, just as in the case of electromagnetic plasma, has been long thought of as a reason for the dissociation of heavy meson [72]. The color screening model used in the present work assumes that the pressure abruptly falls at freeze-out. Within QGP, color charges are free, where screening can happen. So we have a screening region where the effective temperature is greater than the dissociation temperature of the meson of interest (here, D^0). We have the pressure profile for cooling as:

$$p(\tau, r) = -c_1 + c_2 \frac{c_s^2}{\tau^{(c_s^2+1)}} + \frac{4\eta}{3\tau} \left(\frac{c_s^2 + 1}{c_s^2 - 1} \right) + \frac{c_3}{\tau^{c_s^2}} \tag{7}$$

where, c_s is the speed of sound and c_1, c_2, c_3 are the constants determined using following boundary conditions,

$$p(\tau_i, r) = p(\tau_i, 0) h(r) \quad ; \quad p(\tau_s, r) = p_{QGP}, \tag{8}$$

where, τ_i is the initial thermalization time, τ_s is the screening time, p_{QGP} is the QGP pressure inside the screening region and $h(r)$ is the radial distribution function in the transverse direction given by,

$$h(r) = \left(1 - \frac{r^2}{R_T^2}\right)^{\beta} \theta(R_T - r) \tag{9}$$

The $c - \bar{u}$ pair present inside the screening region may escape this region provided they have enough kinetic energy. They are near the boundary of this region, which itself evolves with time. This restricts the allowed values of azimuthal angle $\phi_{max}(r)$ for the survival of D^0. We find the survival probability, $S_c^{D^0}(p_T, b)$ of D^0 by integrating over $\phi_{max}(r)$, whose expression is given by equation (15) of Ref. [102].

Gluonic dissociation

On absorption of a soft gluon, a singlet state of D^0 could excite to an octet state. This is the principle behind the suppression of a meson due to gluonic dissociation. The cross-section for dissociation is given by [124]:

$$\sigma_{diss,nl}(E_g) = \frac{\pi^2 \alpha_{nl} E_g}{N_c N_{\bar{u}}} \sqrt{\frac{m_b}{E_g + E_{nl}}} \frac{(l+1)|J_{nl}^{q,l+1}|^2 + l|J_{nl}^{q,l-1}|^2}{2l+1}, \tag{10}$$

where, $J_{nl}^{q,l'} = \int_0^\infty dr r g_{nl}^*(r) h_{ql'}(r)$ is the probability density. Here, g_{nl}^* and $h_{ql'}(r)$ are the singlet and octet wave functions of D^0, respectively obtained by numerically solving Schrodinger's equation.

We take the thermal average of the above cross-section over a modified Bose-Einstein distribution to get the decay width $\Gamma_{gd,nl}$ corresponding to gluonic dissociation.

Collisional damping

Collisional damping is the dissociation of the bound state of quarks due to collision with medium particles. We hence find the associated decay width given by the expectation value of the imaginary part of effective quark-antiquark potential in QGP [67]:

$$\Gamma_{damp,nl}(\tau, p_T, b) = \int g_{nl}(r)^\dagger Im(V) g_{nl}(r) dr, \tag{11}$$

where $g_{nl}(r)$ is the D^0 singlet wavefunction.

Shadowing

Shadowing is a cold nuclear effect caused by multiple scattering of patrons. We have used *EPS09* parametrization to calculate shadowing for nuclei [245]. We find suppression due to shadowing as:

$$S_{sh}(p_T, b) = \frac{d\sigma_{AA}/dy}{T_{AA} d\sigma_{pp}/dy} \tag{12}$$

Shadowing effect influence the initial production of D^0, hence we replace (3) by shadowing corrected initial number of D^0 given by;

$$N^i_{D^0}(\tau_0, b) = N_{D^0}(\tau_0, b) S_{sh}(p_T, b). \tag{13}$$

A.2 Recombination mechanism

We have considered the possibility of recombination of $c - \bar{u}$ due to the de-excitation of the octet to singlet state by emission of a gluon. We find the recombination cross-section in QGP using detailed balance from the gluonic dissociation cross-section as:

$$\sigma_{f,nl} = \frac{48}{36}\sigma_{d,nl}\frac{(s - M_{nl}^2)^2}{s(s - 4m_b m_{\bar{u}})}, \tag{14}$$

where, s is the Mandelstam variable, M_{nl}, m_c and $m_{\bar{u}}$ are the masses of D^0, charm quark and up anti-quark respectively. We then define the recombination factor, $\Gamma_{F,nl}$ as the thermal average of the product of the above cross-section and relative velocity between $c - \bar{u}$ [100].

A.3 Survival probability

We combine the two decay widths obtained in Sec. A.1 and Sec. A.1 as follows:

$$\Gamma_{D,nl} = \Gamma_{damp,nl} + \Gamma_{gd,nl}. \tag{15}$$

This $\Gamma_{D,nl}$ is used to calculate the decay factors (ϵ) in equation (4) and (5). On numerically solving equation (2), we get the final number of D^0 mesons. Using this, we calculate the survival probability due to shadowing, gluonic dissociation, and collisional damping as:

$$S_{sgc}^{D^0} = \frac{N_{D^0,nl}^{f}(p_T, b)}{N_{D^0,nl}(\tau_0, b)}. \tag{16}$$

We now combine this with the survival probability due to color screening of Sec. A.1, as we have introduced it independently. Therefore, we write the final D^0 survival probability as:

$$S_P(p_T, b) = S_{sgc}^{D^0}(p_T, b) S_c^{D^0}(p_T, b) \tag{17}$$

We have calculated survival probability of D^0 for two values of dissociation temperature, T_D as $1.5\,T_c$ and $2\,T_c$, where T_c is 170 MeV. The experimental value of prompt D^0 nuclear modification factor (R_{AA}) as a function of transverse momentum and centrality at $\sqrt{s_{NN}} = 2.76 TeV$ is obtained from [241]. The model requires cross-section for quark anti-quark pair formation as an input, which we have calculated using the cross-section formula for the process ($gg \to q\bar{q}$) [246]. The formation time of D^0 meson is also an unknown parameter. Therefore, we have plotted the results for some specific values of formation times.

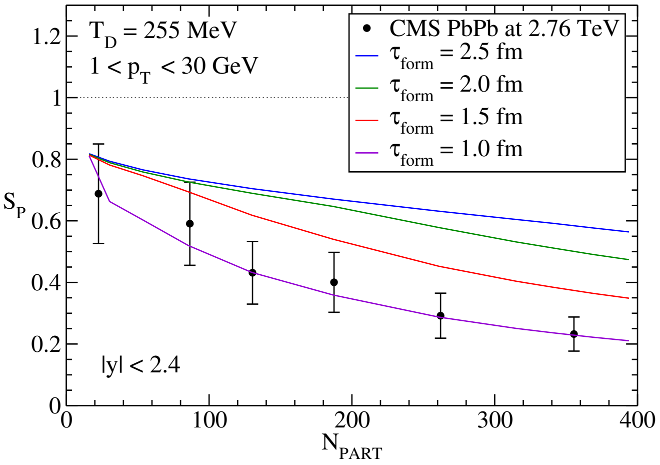

Figure 1: The survival probability (S_P) of D^0 meson is plotted and compared with R_{AA} as a function of centrality at mid-rapidity at $T_D = 1.5T_c$.

In Figs. (1) and (2), we have plotted R_{AA} versus N_{PART} for $T_D = 255$ MeV and $T_D = 340$ MeV respectively. The curve corresponding to $\tau_{form} = 1$ fm shows reasonable agreement with the suppression data. We see that curves with higher values of τ_{form} stay mostly unchanged with an increase in dissociation temperature, T_D. The curves differ with dissociation temperature significantly only for $\tau_{form} =$

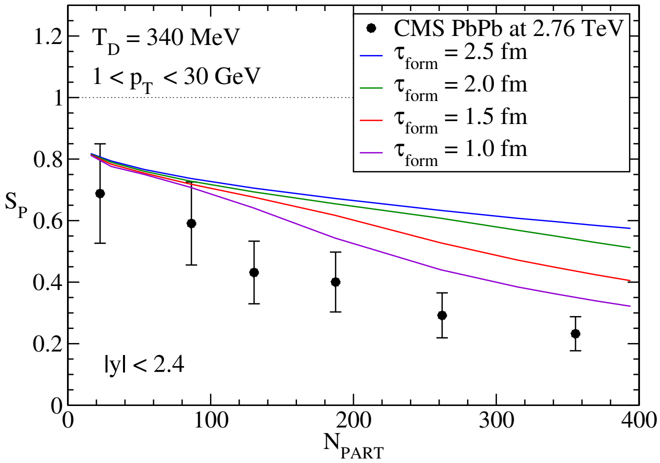

Figure 2: The survival probability (S_P) of D^0 meson is plotted and compared with R_{AA} as a function of centrality at mid-rapidity at $T_D = 2T_c$.

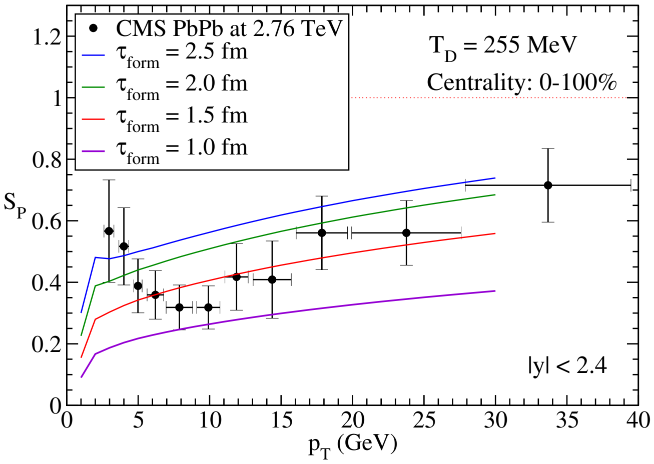

Figure 3: The survival probability (S_P) of D^0 meson R_{AA} as a function of traverse momentum at mid-rapidity at $T_D = 1.5T_c$.

1.5 fm and $\tau_{form} = 1$ fm. It suggests that if the dissociation temperature is lower, then the meson is relatively weakly bound, which results in more D^0 suppression. For R_{AA} versus p_T plots in Figs. (3) and (4), our model predictions are showing close agreement with the data points, but it fails to reproduce the pattern at $p_T < 10 GeV/c$.

A.4 Summary

We found that our predicted values for centrality dependent suppression follow the trend of data points. For R_{AA} versus p_T, our model shows reasonable agreement with the data, but only for transverse momentum greater than 10 GeV. These are

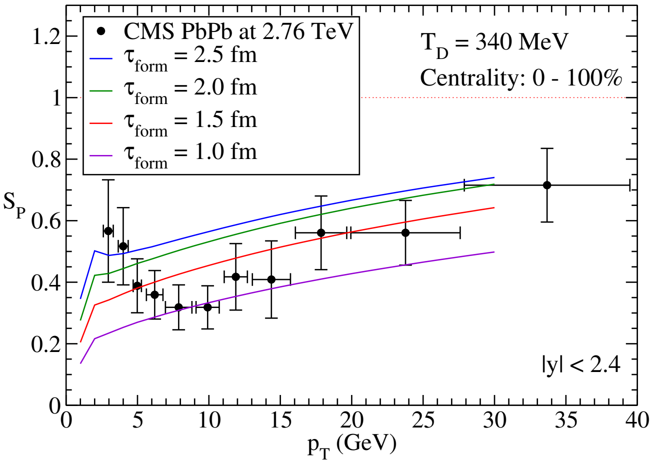

Figure 4: The survival probability (S_P) of D^0 meson R_{AA} as a function of traverse momentum at mid-rapidity at $T_D = 2T_c$.

our preliminary results for open flavor D^0 using the precursor suppression model. There is a need to refine the parameters used and test this model with more open flavor mesons like B^0, D^+, $D_s^{\pm}$, B_s^0 and B_c^+.

References

[1] S.L. Glashow, Nuclear Physics **10**, 107 (1959). URL https://doi.org/10.1016/0029-5582(59)90196-8

[2] A. Salam, J.C. Ward, (1964). URL https://doi.org/10.1016/0031-9163(64)90711-5

[3] A. Salam, J.C. Ward, Il Nuovo Cimento (1955-1965) **11**, 568 (1959). URL https://doi.org/10.1007/BF02726525

[4] S. Weinberg, Phys. Rev. Lett. **19**, 1264 (1967). URL https://doi.org/10.1103/PhysRevLett.19.1264

[5] URL https://commons.wikimedia.org/wiki/File:Elementary_particle_interactions_in_the_Standard_Model.png

[6] C.N. Yang, R.L. Mills, Phys. Rev. **96**, 191 (1954). URL https://doi.org/10.1103/PhysRev.96.191

[7] V. Khachatryan, A.M. Sirunyan, A. Tumasyan, W. Adam, E. Asilar, T. Bergauer, J. Brandstetter, E. Brondolin, M. Dragicevic, J. High Energy Phys. **2017**(3), 1 (2017). URL https://doi.org/10.1007/JHEP03(2017)156

[8] J. Frenkel, Phys. Lett. B **60**(1), 74 (1975). URL https://doi.org/10.1016/0370-2693(75)90531-6

[9] D.J. Gross, Conf.Proc.C **7507281**, 141 (1975). URL https://inspirehep.net/literature/105732

[10] H.D. Politzer, Phys. Rev. Lett. **30**, 1346 (1973). URL https://doi.org/10.1103/PhysRevLett.30.1346

[11] D.J. Gross, F. Wilczek, Phys. Rev. Lett. **30**, 1343 (1973). URL https://doi.org/10.1103/PhysRevLett.30.1343

[12] F. Karsch, PoS **CORFU2018**, 163 (2019). URL https://doi.org/10.22323/1.347.0163

[13] C. Loizides, Nucl. Phys. A **1005**, 121964 (2021). URL https://doi.org/10.1016/j.nuclphysa.2020.121964

[14] E.V. Shuryak, Phys. Rep. **61**(2), 71 (1980). URL https://doi.org/10.1016/0370-1573(80)90105-2

[15] E.V. Shuryak, Sov. Phys. - JETP (Engl. Transl.); (United States) **47:2** (1978). URL https://www.osti.gov/biblio/6583653

[16] B.V. Jacak, B. Müller, Science **337**(6092), 310 (2012). URL https://doi.org/10.1126/science.1215901

[17] M. Stephanov, in Proceedings of XXIVth International Symposium on Lattice Field Theory PoS(LAT2006), vol. 32 (SISSA Medialab, 2006), vol. 32, p. 024. URL https://doi.org/

10.22323/1.032.0024

[18] J. Adams, M. Aggarwal, Z. Ahammed, J. Amonett, B. Anderson, D. Arkhipkin, G. Averichev, S. Badyal, Y. Bai, J. Balewski, et al., Nuclear Physics A **757**(1-2), 102 (2005). URL https://doi.org/10.1016/j.nuclphysa.2005.03.085

[19] M. Krzewicki, A. Collaboration, et al., Journal of Physics G: Nuclear and Particle Physics **38**(12), 124047 (2011). URL http://dx.doi.org/10.1088/0954-3899/38/12/124047

[20] P.K. Kovtun, D.T. Son, A.O. Starinets, Physical review letters **94**(11), 111601 (2005). URL https://doi.org/10.1103/PhysRevLett.94.111601

[21] C. Ratti, Reports on Progress in Physics **81**(8), 084301 (2018). URL https://doi.org/10.1088/1361-6633/aabb97

[22] J.E. Bernhard, J.S. Moreland, S.A. Bass, Nature Physics **15**(11), 1113 (2019). URL https://doi.org/10.1038/s41567-019-0611-8

[23] J.N. Guenther, The European Physical Journal A **57**(4), 1 (2021). URL https://doi.org/10.1140/epja/s10050-021-00354-6

[24] A. Dubla, S. Masciocchi, J. Pawlowski, B. Schenke, C. Shen, J. Stachel, Nuclear Physics A **979**, 251 (2018). URL https://doi.org/10.1016/j.nuclphysa.2018.09.046

[25] U. Heinz, in AIP Conference Proceedings, vol. 739 (American Institute of Physics, 2004), vol. 739, pp. 163–180. URL https://doi.org/10.1063/1.1843595

[26] M. Martinez, M. Strickland, Journal of Physics G: Nuclear and Particle Physics **35**(10), 104162 (2008). URL http://dx.doi.org/10.1088/0954-3899/35/10/104162

[27] Study of the final state particle composition in Pb-Pb collisions at $\sqrt{s_{NN}} = 5.02$ TeV as a function of centrality - CERN Document Server (2023). URL https://cds.cern.ch/record/2687453/files

[28] A. Bazavov, H.T. Ding, P. Hegde, O. Kaczmarek, F. Karsch, N. Karthik, E. Laermann, A. Lahiri, R. Larsen, S.T. Li, et al., Physics Letters B **795**, 15 (2019). URL https://doi.org/10.1016/j.physletb.2019.05.013

[29] P. Steinbrecher, HotQCD-Collaboration, Nuclear Physics A **982**, 847 (2019). URL https://doi.org/10.1016/j.nuclphysa.2018.08.025

[30] M. D'Elia, Nuclear Physics A **982**, 99 (2019). URL https://doi.org/10.1016/j.nuclphysa.2018.10.042

[31] F. Abe, D. Amidei, G. Apollinari, G. Ascoli, M. Atac, P. Auchincloss, A.R. Baden, A. Barbaro-Galtieri, V.E. Barnes, F. Bedeschi, S. Behrends, S. Belforte, G. Bellettini, J. Bellinger, J. Bensinger, et al., Phys. Rev. Lett. **62**, 613 (1989). URL https://doi.org/10.1103/PhysRevLett.62.613

[32] G. Arnison, A. Astbury, B. Aubert, C. Bacci, R. Bernabei, A. Bézaguet, R. Böck, et al., Phys. Lett. B **123**(1), 115 (1983). URL https://doi.org/10.1016/0370-2693(83)90970-X

[33] H1 Collaboration, I. Abt, T. Ahmed, V. Andreev, B. Andrieu, R.D. Appuhn, M. Arpagaus, A. Babaev, H. Bärwolff, J. Bán, Phys. Lett. B **314**(3), 436 (1993). URL https://doi.org/10.1016/0370-2693(93)91263-M

[34] S.B. Libby, G. Sterman, Phys. Rev. D **18**, 3252 (1978). URL https://doi.org/10.1103/PhysRevD.18.3252

[35] S. Bethke, J. Phys. G: Nucl. Part. Phys. **26**(7), R27 (2000). URL https://doi.org/10.1088/0954-3899/26/7/201

[36] S. Chatrchyan, V. Khachatryan, A. Sirunyan, A. Tumasyan, W. Adam, E. Aguilo, T. Bergauer, et al., Phys. Lett. B **716**(1), 30 (2012). URL https://doi.org/10.1016/j.physletb.2012.08.021

[37] M. Gyulassy, M. Plümer, Phys. Lett. B **243**(4), 432 (1990). URL https://doi.org/10.1016/0370-2693(90)91409-5

[38] K.J. Eskola, X.N. Wang, Int. J. Mod. Phys. A **10**(20n21), 3071 (1995). URL https://doi.org/10.1142/S0217751X95001455

[39] R. Baier, Yu.L. Dokshitzer, A.H. Mueller, S. Peigné, D. Schiff, Nucl. Phys. B **484**(1), 265 (1997). URL https://doi.org/10.1016/S0550-3213(96)00581-0

[40] C. Klein-Bösing, CERN Document Server (2020). URL https://cds.cern.ch/record/2729069?ln=en

[41] J.Y. Ollitrault, Phys. Rev. D **46**, 229 (1992). URL https://doi.org/10.1103/PhysRevD.46.229

[42] S. Voloshin, Y. Zhang, Z. Phys. C -. Particles and Fields **70**(4), 665 (1996). URL https://doi.org/10.1007/s002880050141

[43] M. Luzum, J. Phys. G: Nucl. Part. Phys. **38**(12), 124026 (2011). URL https://doi.org/10.1088/0954-3899/38/12/124026

[44] M. Strickland, Nucl. Phys. A **982**, 92 (2019). URL https://doi.org/10.1016/j.nuclphysa.2018.09.071

[45] A. Bilandzic, R. Snellings, S. Voloshin, Phys. Rev. C **83**, 044913 (2011). URL https://doi.org/10.1103/PhysRevC.83.044913

[46] C. Chattopadhyay, R.S. Bhalerao, J.Y. Ollitrault, S. Pal, Phys. Rev. C **97**, 034915 (2018). URL https://doi.org/10.1103/PhysRevC.97.034915

[47] B. Schenke, C. Shen, P. Tribedy, Phys. Rev. C **102**, 044905 (2020). URL https://doi.org/10.1103/PhysRevC.102.044905

[48] C. Escobar, Nuclear Physics B **98**(1), 173 (1975). URL https://doi.org/10.1016/0550-3213(75)90208-4

[49] G.R. Farrar, S.C. Frautschi, Phys. Rev. Lett. **36**, 1017 (1976). URL https://link.aps.org/doi/10.1103/PhysRevLett.36.1017

[50] E. Feinberg, Il Nuovo Cimento A (1965-1970) **34**(3), 391 (1976). URL https://doi.org/10.1007/BF02783618

[51] G. David. Direct real photons in relativistic heavy ion collisions (2020). URL https://doi.org/10.1088/1361-6633/ab6f57

[52] J. Adam, D. Adamova, M.M. Aggarwal, G.A. Rinella, M. Agnello, N. Agrawal, Z. Ahammed, S. Ahmad, S.U. Ahn, S. Aiola, et al., Nature Physics **13**, 535 (2017). URL https://doi.org/10.1038/nphys4111

[53] D.S.D. Albuquerque, Nucl. Phys. A **982**, 823 (2019). URL https://doi.org/10.1016/j.nuclphysa.2018.08.033

[54] J. Rafelski, B. Müller, Phys. Rev. Lett. **48**, 1066 (1982). URL https://doi.org/10.1103/PhysRevLett.48.1066

[55] J. Rafelski, B. Müller, Phys. Rev. Lett. **56**, 2334 (1986). URL https://doi.org/10.1103/PhysRevLett.56.2334

[56] T. Biró, J. Zimányi, Physics Letters B **113**(1), 6 (1982). URL http://real-eod.mtak.hu/7402/1/KFKIreports_81-069.pdf

[57] S. Weinberg, Physica A **96**(1), 327 (1979). URL https://doi.org/10.1016/0378-4371(79)90223-1

[58] N. Brambilla, A. Pineda, J. Soto, A. Vairo, Rev. Mod. Phys. **77**, 1423 (2005). URL https://doi.org/10.1103/RevModPhys.77.1423

[59] T. Mannel, Rep. Prog. Phys. **60**(10), 1113 (1997). URL https://doi.org/10.1088/0034-4885/60/10/003

[60] M. Neubert, in Physics In $D \geq 4$ Tasi 2004 (World Scientific, Singapore, 2006), pp. 149–194. URL https://doi.org/10.1142/9789812773579_0004

[61] N. Isgur, M.B. Wise, Phys. Lett. B **232**(1), 113 (1989). URL https://doi.org/10.1016/0370-2693(89)90566-2

[62] N. Isgur, M.B. Wise, Phys. Lett. B **237**(3), 527 (1990). URL https://doi.org/10.1016/0370-2693(90)91219-2

[63] G.T. Bodwin, E. Braaten, G.P. Lepage, Phys. Rev. D **51**, 1125 (1995). URL https://doi.org/10.1103/PhysRevD.51.1125

[64] G.T. Bodwin, E. Braaten, G.P. Lepage, Phys. Rev. D **55**, 5853 (1997). URL https://doi.org/10.1103/PhysRevD.55.5853

[65] W.E. Caswell, G.P. Lepage, Phys. Lett. B **167**(4), 437 (1986). URL https://doi.org/10.1016/0370-2693(86)91297-9

[66] F. Nendzig, A model for the suppression of Υ mesons in PbPb collisions at LHC energies. Ph.D. thesis (2019). URL https://doi.org/10.11588/heidok.00016266. [Online; accessed 25. Feb. 2023]

[67] M. Laine, O. Philipsen, M. Tassler, P. Romatschke, Journal of High Energy Physics **2007**(03), 054 (2007)

[68] N. Brambilla, M.Á. Escobedo, J. Ghiglieri, A. Vairo, Journal of High Energy Physics **2013**(5), 130 (2013). URL http://dx.doi.org/10.1007/JHEP05(2013)130

[69] M. Strickland, D. Bazow, Nucl. Phys. A **879**, 25 (2012). URL https://doi.org/10.1016/j.nuclphysa.2012.02.003

[70] URL https://en.wikipedia.org/wiki/File:Yukawa_coulomb_compare.svg

[71] A. Bazavov, J.H. Weber, Prog. Part. Nucl. Phys. **116**, 103823 (2021). URL https://doi.org/10.1016/j.ppnp.2020.103823

[72] T. Matsui, H. Satz, Phys. Lett. B **178**(4), 416 (1986). URL https://doi.org/10.1016/0370-2693(86)91404-8

[73] J.L. Albacete, N. Armesto, R. Baier, G.G. Barnaföldi, et al., Int. J. Mod. Phys. E **22**(04), 1330007 (2013). URL https://doi.org/10.1142/S0218301313300075

[74] A. Rothkopf, Phys. Rep. **858**, 1 (2020). URL https://doi.org/10.1016/j.physrep.2020.02.006

[75] J.J.e.a. Aubert, Phys. Lett. B **123**(3), 275 (1983). URL https://doi.org/10.1016/0370-2693(83)90437-9

[76] M. Arneodo, Phys. Rep. **240**(5), 301 (1994). URL https://doi.org/10.1016/0370-1573(94)90048-5

[77] L.L. Frankfurt, M.I. Strikman, S. Liuti, Phys. Rev. Lett. **65**, 1725 (1990). URL https://doi.org/10.1103/PhysRevLett.65.1725

[78] K.J. Eskola, Nucl. Phys. B **400**(1), 240 (1993). URL https://doi.org/10.1016/0550-3213(93)90406-F

[79] G. Altarelli, G. Parisi, Nucl. Phys. B **126**(2), 298 (1977). URL https://doi.org/10.1016/0550-3213(77)90384-4

[80] K.J. Eskola, P. Paakkinen, H. Paukkunen, C.A. Salgado, Eur. Phys. J. C **77**(3), 1 (2017). URL https://doi.org/10.1140/epjc/s10052-017-4725-9

[81] D. McGlinchey, A.D. Frawley, R. Vogt, Phys. Rev. C **87**, 054910 (2013). URL https://doi.org/10.1103/PhysRevC.87.054910

[82] V. Emel'yanov, A. Khodinov, S.R. Klein, R. Vogt, Phys. Rev. Lett. **81**, 1801 (1998). URL https://doi.org/10.1103/PhysRevLett.81.1801

[83] T.J. Hou, S. Dulat, J. Gao, M. Guzzi, J. Huston, P. Nadolsky, C. Schmidt, J. Winter, K. Xie, C.P. Yuan, J. High Energy Phys. **2018**(2), 1 (2018). URL https://doi.org/10.1007/JHEP02(2018)059

[84] R. Aaij, B. Adeva, M. Adinolfi, C. Adrover, A. Affolder, Z. Ajaltouni, J. Albrecht, F. Alessio, M. Alexander, S. Ali, et al., J. High Energy Phys. **2014**(2), 1 (2014). URL https://doi.org/10.1007/JHEP02(2014)072

[85] N. Dutta, N. Borghini, Mod. Phys. Lett. A **30**(37), 1550205 (2015). URL https://doi.org/10.1142/S0217732315502053

[86] N. Brambilla, M.A. Escobedo, A. Vairo, P. Vander Griend, Phys. Rev. D **100**, 054025 (2019). URL https://doi.org/10.1103/PhysRevD.100.054025

[87] X. Yao, T. Mehen, J. High Energy Phys. **2021**(2), 1 (2021). URL https://doi.org/10.1007/JHEP02(2021)062

[88] N. Brambilla, M.Á. Escobedo, M. Strickland, A. Vairo, P.V. Griend, J.H. Weber, J. High Energy Phys. **2021**(5), 1 (2021). URL https://doi.org/10.1007/JHEP05(2021)136

[89] N. Brambilla, M.A. Escobedo, J. Soto, A. Vairo, Phys. Rev. D **96**, 034021 (2017). URL https://doi.org/10.1103/PhysRevD.96.034021

[90] R. Sharma, Eur. Phys. J. Spec. Top. **230**(3), 697 (2021). URL https://doi.org/10.1140/epjs/s11734-021-00025-z

[91] N. Brambilla, M.A. Escobedo, J. Soto, A. Vairo, Phys. Rev. D **97**, 074009 (2018). URL https://doi.org/10.1103/PhysRevD.97.074009

[92] Y. Akamatsu, Prog. Part. Nucl. Phys. **123**, 103932 (2022). URL https://doi.org/10.1016/j.ppnp.2021.103932

[93] J. Schukraft, Nuclear Physics A **967**, 1 (2017). URL https://doi.org/10.1016/j.nuclphysa.2017.05.036

[94] R. Sharma, I. Vitev, Physical Review C **87**(4), 044905 (2013). URL https://doi.org/10.1103/PhysRevC.87.044905

[95] X. Du, M. He, R. Rapp, Physical Review C **96**(5), 054901 (2017). URL https://doi.org/10.1103/PhysRevC.96.054901

[96] S. Cao, Nucl. Phys. A **1005**, 121984 (2021). URL https://doi.org/10.1016/j.nuclphysa.2020.121984

[97] B. Krouppa, A. Rothkopf, M. Strickland, Physical Review D **97**(1), 016017 (2018). URL https://doi.org/10.1103/PhysRevD.97.016017

[98] X. Yao, W. Ke, Y. Xu, S.A. Bass, B. Müller, J. High Energy Phys. **2021**(1), 1 (2021). URL https://doi.org/10.1007/JHEP01(2021)046

[99] S. Digal, P. Petreczky, H. Satz, Physical Review D **64**(9), 094015 (2001). URL https://doi.org/10.1103/PhysRevD.64.094015

[100] C.R. Singh, S. Ganesh, M. Mishra, The European Physical Journal C **79**(2), 147 (2019). URL https://doi.org/10.1140/epjc/s10052-019-6646-2

[101] S. Ganesh, M. Mishra, Phys. Rev. C **88**, 044908 (2013). URL https://doi.org/10.1103/PhysRevC.88.044908

[102] P.K. Srivastava, M. Mishra, C.P. Singh, Phys. Rev. C **87**, 034903 (2013). URL https://doi.org/10.1103/PhysRevC.87.034903

[103] M. Mishra, C.P. Singh, V.J. Menon, R.K. Dubey, Phys. Lett. B **656**(1), 45 (2007). URL https://doi.org/10.1016/j.physletb.2007.09.043

[104] B. Krouppa, A. Rothkopf, M. Strickland, Nuclear Physics A **982**, 727 (2019). URL https://doi.org/10.1016/j.nuclphysa.2018.09.034

[105] S. McDonald, C. Shen, F. Fillion-Gourdeau, S. Jeon, C. Gale, Physical Review C **95**(6), 064913 (2017). URL https://doi.org/10.1103/PhysRevC.93.034912

[106] M. Alqahtani, M. Nopoush, R. Ryblewski, M. Strickland, Physical review letters **119**(4), 042301 (2017). URL https://doi.org/10.1103/PhysRevLett.119.042301

[107] M. Habich, J.L. Nagle, P. Romatschke, Eur. Phys. J. C **75**(1), 1 (2015). URL https://doi.org/10.1140/epjc/s10052-014-3206-7

[108] J.D. Bjorken, Physical review D **27**(1), 140 (1983). URL https://doi.org/10.1103/PhysRevD.27.140

[109] L. Del Zanna, V. Chandra, G. Inghirami, V. Rolando, A. Beraudo, A. De Pace, G. Pagliara, A. Drago, F. Becattini, The European Physical Journal C **73**(8), 2524 (2013). URL https://doi.org/10.1140/epjc/s10052-013-2524-5

[110] S. Borsanyi, G. Endrődi, Z. Fodor, A. Jakovac, S.D. Katz, S. Krieg, C. Ratti, K.K. Szabo, Journal of High Energy Physics **2010**(11), 77 (2010). URL https://doi.org/10.1007/JHEP11(2010)077

[111] P.K. Srivastava, S.K. Tiwari, C.P. Singh, Phys. Rev. D **82**, 014023 (2010). URL https://doi.org/10.1103/PhysRevD.82.014023

[112] S. Chatterjee, R. Godbole, S. Gupta, Physical Review C **81**(4), 044907 (2010). URL https://doi.org/10.1103/PhysRevC.81.044907

[113] H.T. Ding, Nucl. Phys. A **1005**, 121940 (2021). URL https://doi.org/10.1016/j.nuclphysa.2020.121940

[114] C. Loizides, J. Kamin, D. d'Enterria, Physical Review C **97**(5), 054910 (2018). URL https://doi.org/10.1103/PhysRevC.97.054910

[115] E. Abbas, B. Abelev, J. Adam, D. Adamova, A.M. Adare, M.M. Aggarwal, G. Aglieri Rinella, M. Agnello, A.G. Agocs, A. Agostinelli, Z. Ahammed, A. Ahmad Masoodi, et al.,

[116] J. Adam, D. Adamova, M.M. Aggarwal, G. Aglieri Rinella, M. Agnello, N. Agrawal, Z. Ahammed, S. Ahmad, S.U. Ahn, S. Aiola, A. Akindinov, et al.,

[117] W. Busza, K. Rajagopal, W. Van Der Schee, Annual Review of Nuclear and Particle Science **68**, 339 (2018). URL https://doi.org/10.1146/annurev-nucl-101917-020852

[118] H. Song, U. Heinz, Physical Review C **81**(2), 024905 (2010). URL https://doi.org/10.1103/PhysRevC.81.024905

[119] P.P. Bhaduri, N. Borghini, A. Jaiswal, M. Strickland, Physical Review C **100**(5), 051901(R) (2019). URL https://doi.org/10.1103/PhysRevC.100.051901

[120] F. Karsch, Lattice QCD at high temperature and density, in Lectures on Quark Matter,

Lecture Notes in Physics, vol. 583 (Springer, Berlin, Heidelberg, 2002). URL https://doi.org/10.1007/3-540-45792-5_6

[121] S.S. Adler, S. Afanasiev, C. Aidala, N. Ajitanand, Y. Akiba, J. Alexander, R. Amirikas, L. Aphecetche, S. Aronson, R. Averbeck, et al., Physical Review C **71**(3), 034908 (2005). URL https://doi.org/10.1103/PhysRevC.71.034908

[122] S. Acharya, D. Adamova, S.P. Adhya, A. Adler, J. Adolfsson, M.M. Aggarwal, G. Aglieri Rinella, M. Agnello, et al., Phys. Rev. C **101**, 044907 (2020). URL https://doi.org/10.1103/PhysRevC.101.044907

[123] J. Adam, D. Adamova, M.M. Aggarwal, G. Aglieri Rinella, M. Agnello, N. Agrawal, Z. Ahammed, S.U. Ahn, I. Aimo, et al., Phys. Rev. C **93**, 034913 (2016). URL https://doi.org/10.1103/PhysRevC.93.034913

[124] F. Nendzig, G. Wolschin, Phys. Rev. C **87**, 024911 (2013). URL https://doi.org/10.1103/PhysRevC.87.024911

[125] N. Brambilla, M.Á. Escobedo, J. Ghiglieri, A. Vairo, Journal of High Energy Physics **2011**(12), 1 (2011). URL http://dx.doi.org/10.1007/JHEP12(2011)116

[126] C. Loizides, J. Kamin, D. d'Enterria, Physical Review C **99**(1), 019901(E) (2019). URL https://doi.org/10.1103/PhysRevC.99.019901

[127] P. Cheng, Q. Meng, Y. Xia, J. Ping, H. Zong, Phys. Rev. D **98**, 116010 (2018). URL https://doi.org/10.1103/PhysRevD.98.116010

[128] R. Vogt, Physical Review C **81**(4), 044903 (2010). URL https://doi.org/10.1103/PhysRevC.81.044903

[129] K. Eskola, H. Paukkunen, C. Salgado, Journal of High Energy Physics **2009**(04), 065 (2009). URL https://doi:10.1088/1126-6708/2009/04/065

[130] K.J. Eskola, P. Paakkinen, H. Paukkunen, C.A. Salgado, The European Physical Journal C **77**(3), 163 (2017). URL https://doi.org/10.1140/epjc/s10052-017-4725-9

[131] S. Dulat, T.J. Hou, J. Gao, M. Guzzi, J. Huston, P. Nadolsky, J. Pumplin, C. Schmidt, D. Stump, C.P. Yuan, Physical Review D **93**(3), 033006 (2016). URL https://doi.org/10.1103/PhysRevD.93.033006

[132] J. Pumplin, D.R. Stump, J. Huston, H.L. Lai, P. Nadolsky, W.K. Tung, J. High Energy Phys. **2002**(07), 012 (2002). URL https://doi.org/10.1088/1126-6708/2002/07/012

[133] N. Armesto, Journal of Physics G: Nuclear and Particle Physics **32**(11), R367 (2006). URL https://doi.org/10.1088/0954-3899/32/11/R01

[134] R. Thews, M.L. Mangano, Physical Review C **73**(1), 014904 (2006). URL https://doi.org/10.1103/PhysRevC.73.014904

[135] R.L. Thews, M. Schroedter, J. Rafelski, Phys. Rev. C **63**, 054905 (2001). URL https://doi.org/doi/10.1103/PhysRevC.63.054905

[136] M.L. Miller, K. Reygers, S.J. Sanders, P. Steinberg, Annu. Rev. Nucl. Part. Sci. **57**, 205 (2007). URL https://doi.org/10.1146/annurev.nucl.57.090506.123020

[137] V. Khachatryan, A. Sirunyan, A. Tumasyan, W. Adam, E. Asilar, T. Bergauer, J. Brandstetter, E. Brondolin, M. Dragicevic, J. Erö, et al., Physics Letters B **770**, 357 (2017). URL https://doi.org/10.1016/j.physletb.2017.04.031

[138] B. Abelev, J. Adam, D. Adamova, M.M. Aggarwal, M. Agnello, A. Agostinelli, N. Agrawal, Z. Ahammed, et al., Phys. Lett. B **738**, 361 (2014). URL https://doi.org/10.1016/j.physletb.2014.10.001

[139] A.M. Sirunyan, A. Tumasyan, W. Adam, F. Ambrogi, E. Asilar, T. Bergauer, J. Brandstetter, E. Brondolin, M. Dragicevic, J. Erö, et al., Physics Letters B **790**, 270 (2019). URL https://doi.org/10.1016/j.physletb.2019.01.006

[140] S. Acharya, F.T. Acosta, D. Adamova, J. Adolfsson, M.M. Aggarwal, G.A. Rinella, M. Agnello, N. Agrawal, Z. Ahammed, S.U. Ahn, et al., Phys. Lett. B **790**, 89 (2019). URL https://doi.org/10.1016/j.physletb.2018.11.067

[141] P. Kovtun, J. Phys. A: Math. Theor. **45**(47), 473001 (2012). URL https://doi.org/10.1088/1751-8113/45/47/473001

[142] D.T. Son, A.O. Starinets, J. High Energy Phys. **2006**(03), 052 (2006). URL https://doi.org/10.1088/1126-6708/2006/03/052

[143] M.J. Clerk, Philos. Trans. R. Soc. Lond. **157**, 49 (1867). URL https://doi.org/10.1098/rstl.1867.0004

[144] C. Cattaneo, Sulla Conduzione Del Calore (Springer, Berlin, Germany, 2011). URL https://doi.org/10.1007/978-3-642-11051-1_5

[145] I. Müller, Z. Phys. **198**(4), 329 (1967). URL https://doi.org/10.1007/BF01326412

[146] W. Israel, J.M. Stewart, Ann. Phys. **118**(2), 341 (1979). URL https://doi.org/10.1016/0003-4916(79)90130-1

[147] A. Muronga, Phys. Rev. C **69**, 034903 (2004). URL https://doi.org/10.1103/PhysRevC.69.034903

[148] P.K. Kovtun, A.O. Starinets, Phys. Rev. D **72**, 086009 (2005). URL https://doi.org/10.1103/PhysRevD.72.086009

[149] W. Florkowski, M.P. Heller, M. Spaliński, Rep. Prog. Phys. **81**(4), 046001 (2018). URL https://doi.org/10.1088/1361-6633/aaa091

[150] S.A. Hartnoll, S.P. Kumar, J. High Energy Phys. **2005**(12), 036 (2005). URL https://doi.org/10.1088/1126-6708/2005/12/036

[151] R.A. Janik, J. Jankowski, H. Soltanpanahi, J. High Energy Phys. **2016**(6), 1 (2016). URL https://doi.org/10.1007/JHEP06(2016)047

[152] S. Grozdanov, N. Kaplis, A.O. Starinets, J. High Energy Phys. **2016**(7), 1 (2016). URL https://doi.org/10.1007/JHEP07(2016)151

[153] P. Romatschke, Eur. Phys. J. C **76**(6), 1 (2016). URL https://doi.org/10.1140/epjc/s10052-016-4169-7

[154] A. Kurkela, U.A. Wiedemann, B. Wu, Eur. Phys. J. C **79**(11), 1 (2019). URL https://doi.org/10.1140/epjc/s10052-019-7428-6

[155] P. Romatschke, U. Romatschke, Relativistic Fluid Dynamics In and Out of Equilibrium And Applications to Relativistic Nuclear Collisions (Cambridge University Press, Cambridge, England, UK, 2019). URL https://doi.org/10.1017/9781108651998

[156] E.V. Shuryak, Sov. Phys. - JETP (Engl. Transl.); (United States) **47**, 212 (1978). URL https://www.osti.gov/biblio/6583653

[157] E.V. Shuryak, Physics Reports **61**(2), 71 (1980). URL https://doi.org/10.1016/0370-1573(80)90105-2

[158] W. Busza, K. Rajagopal, W. Van Der Schee, Annual Review of Nuclear and Particle Science **68**, 339 (2018). URL https://doi.org/10.1146/annurev-nucl-101917-020852

[159] F. Karsch, E. Laermann, A. Peikert, Nuclear Physics B **605**(1-3), 579 (2001). URL https://doi.org/10.1016/S0550-3213(01)00200-0

[160] J. Berges, M.P. Heller, A. Mazeliauskas, R. Venugopalan, Reviews of Modern Physics **93**(3), 035003 (2021). URL `https://doi.org/10.1103/RevModPhys.93.035003`

[161] J. Casalderrey-Solana, M.P. Heller, D. Mateos, W. van der Schee, Phys. Rev. Lett. **112**, 221602 (2014). URL `https://doi.org/10.1103/PhysRevLett.112.221602`

[162] J. Letessier, J. Rafelski, International Journal of Modern Physics E **9**(02), 107 (2000). URL `https://doi.org/10.1142/S0218301300000076`

[163] K. Ackermann, N. Adams, C. Adler, Z. Ahammed, S. Ahmad, C. Allgower, J. Amsbaugh, M. Anderson, E. Anderssen, H. Arnesen, et al., Physical Review Letters **86**(3), 402 (2001). URL `https://doi.org/10.1103/PhysRevLett.86.402`

[164] K. Adcox, S.S. Adler, N.N. Ajitanand, Y. Akiba, J. Alexander, L. Aphecetche, Y. Arai, S.H. Aronson, R. Averbeck, T.C. Awes, K.N. Barish, et al., Phys. Rev. Lett. **88**, 022301 (2001). URL `https://doi.org/10.1103/PhysRevLett.88.022301`

[165] C. Adler, Z. Ahammed, C. Allgower, J. Amonett, B.D. Anderson, M. Anderson, G.S. Averichev, J. Balewski, O. Barannikova, L.S. Barnby, J. Baudot, et al., Phys. Rev. Lett. **90**, 082302 (2003). URL `https://doi.org/10.1103/PhysRevLett.90.082302`

[166] G. Odyniec, J. Phys. Conf. Ser. **455**(1), 012037 (2013). DOI https://doi.org/10.1088/1742-6596/455/1/012037

[167] J.E. Bernhard, J.S. Moreland, S.A. Bass, Nature Physics **15**(11), 1113 (2019). URL `https://doi.org/10.1038/s41567-019-0611-8`

[168] T.Y. Wu, P.W. Hwang, Relativistic quantum mechanics and quantum fields (World Scientific Publishing Company, 1991)

[169] C. Ratti, Reports on Progress in Physics **81**(8), 084301 (2018). URL `https://doi.org/10.1088/1361-6633/aabb97`

[170] A. Bazavov, T. Bhattacharya, C. DeTar, H.T. Ding, S. Gottlieb, R. Gupta, P. Hegde, U. Heller, F. Karsch, E. Laermann, et al., Physical Review D **90**(9), 094503 (2014). URL `https://doi.org/10.1103/PhysRevD.90.094503`

[171] M. Luzum, P. Romatschke, Physical Review C **78**(3), 034915 (2008). URL `https://doi.org/10.1103/PhysRevC.78.034915`

[172] P. Romatschke. New developments in relativistic viscous hydrodynamics (2010). URL `http://dx.doi.org/10.1142/S0218301310014613`

[173] P. Kovtun. Lectures on hydrodynamic fluctuations in relativistic theories (2012). URL `http://dx.doi.org/10.1088/1751-8113/45/47/473001`

[174] S. Jeon, U. Heinz. Introduction to hydrodynamics (2015). URL `https://doi.org/10.1142/S0218301315300106`

[175] A. Jaiswal, V. Roy. Relativistic hydrodynamics in heavy-ion collisions: general aspects and recent developments (2016). URL `http://dx.doi.org/10.1155/2016/9623034`

[176] W. Florkowski, M.P. Heller, M. Spaliński. New theories of relativistic hydrodynamics in the lhc era (2018). URL `https://doi.org/10.1088/1361-6633/aaa091`

[177] J.P. Blaizot, L. Yan. Emergence of hydrodynamical behavior in expanding ultra-relativistic plasmas (2020). URL `https://doi.org/10.1016/j.aop.2019.167993`

[178] P. Romatschke, The European Physical Journal C **77**(1), 1 (2017). URL `https://doi.org/10.1140/epjc/s10052-016-4567-x`

[179] P. Romatschke, The European Physical Journal C **77**(1), 1 (2017). URL `https://doi.org/10.1140/epjc/s10052-016-4567-x`

[180] M.P. Heller, R.A. Janik, P. Witaszczyk, Phys. Rev. Lett. **110**, 211602 (2013). URL https://doi.org/10.1103/PhysRevLett.110.211602

[181] M.P. Heller, M. Spaliński, Phys. Rev. Lett. **115**, 072501 (2015). URL https://doi.org/10.1103/PhysRevLett.115.072501

[182] P. Romatschke, Journal of High Energy Physics **2017**(12), 1 (2017). URL https://doi.org/10.1007/JHEP12(2017)079

[183] A. Kurkela, W. van der Schee, U.A. Wiedemann, B. Wu, Phys. Rev. Lett. **124**, 102301 (2020). URL https://doi.org/10.1103/PhysRevLett.124.102301

[184] P. Castorina, A. Iorio, D. Lanteri, H. Satz, M. Spousta, Phys. Rev. C **101**, 054902 (2020). URL https://doi.org/10.1103/PhysRevC.101.054902

[185] B. Schenke, C. Shen, P. Tribedy, Physical Review C **102**(4), 044905 (2020). URL https://doi.org/10.1103/PhysRevC.102.044905

[186] M. Habich, G. Miller, P. Romatschke, W. Xiang, The European Physical Journal C **76**(7), 1 (2016). URL https://doi.org/10.1140/epjc/s10052-016-4237-z

[187] J.L. Nagle, W.A. Zajc, Annual Review of Nuclear and Particle Science **68**, 211 (2018). URL https://doi.org/10.1146/annurev-nucl-101916-123209

[188] A. Kurkela, U.A. Wiedemann, B. Wu, The European Physical Journal C **79**(11), 1 (2019). URL https://doi.org/10.1140/epjc/s10052-019-7428-6

[189] U. Heinz, J.S. Moreland, in Journal of Physics: Conference Series, vol. 1271 (IOP Publishing, 2019), vol. 1271, p. 012018. URL https://doi.org/10.1088/1742-6596/1271/1/012018

[190] H. Song, U. Heinz, Phys. Rev. C **78**, 024902 (2008). URL https://doi.org/10.1103/PhysRevC.78.024902

[191] H. Song, U. Heinz, Phys. Rev. C **77**, 064901 (2008). URL https://doi.org/10.1103/PhysRevC.77.064901

[192] H. Song, U. Heinz, Physics Letters B **658**(5), 279 (2008). URL https://doi.org/10.1016/j.physletb.2007.11.019

[193] H. Niemi, G.S. Denicol, P. Huovinen, E. Molnár, D.H. Rischke, Phys. Rev. C **86**, 014909 (2012). URL https://doi.org/10.1103/PhysRevC.86.014909

[194] G. Nijs, W. van der Schee, U. Gürsoy, R. Snellings, Phys. Rev. C **103**, 054909 (2021). URL https://doi.org/10.1103/PhysRevC.103.054909

[195] S.S. Adler, S. Afanasiev, C. Aidala, N.N. Ajitanand, Y. Akiba, J. Alexander, R. Amirikas, L. Aphecetche, S.H. Aronson, R. Averbeck, et al., Phys. Rev. C **69**, 034909 (2004). URL https://doi.org/10.1103/PhysRevC.69.034909

[196] J. Adam, Adagmar, M.M. Aggarwal, G.A. Rinella, M. Agnello, N. Agrawal, Z. Ahammed, S.U. Ahn, I. Aimo, S. Aiola, et al., Physical Review C **93**(3), 034913 (2016). URL http://dx.doi.org/10.1103/PhysRevC.93.034913

[197] B. Abelev, J. Adam, D. Adamová, A.M. Adare, M.M. Aggarwal, G. Aglieri Rinella, M. Agnello, A.G. Agocs, A. Agostinelli, Z. Ahammed, N. Ahmad, et al., Phys. Rev. C **88**, 044910 (2013). URL https://doi.org/10.1103/PhysRevC.88.044910

[198] K. Aamodt, A. Abrahantes Quintana, D. Adamová, A.M. Adare, M.M. Aggarwal, G. Aglieri Rinella, A.G. Agocs, S. Aguilar Salazar, Z. Ahammed, N. Ahmad, A. Ahmad Masoodi, S.U. Ahn, A. Akindinov, D. Aleksandrov, B. Alessandro, et al., Phys. Rev. Lett. **106**, 032301 (2011). URL https://doi.org/10.1103/PhysRevLett.106.032301

[199] C. Eckart, Phys. Rev. **58**, 919 (1940). URL https://link.aps.org/doi/10.1103/PhysRev.58.919

[200] I. Müller, Zeitschrift fur Physik **198**(4), 329 (1967). URL https://doi.org/10.1007/BF01326412

[201] W. Israel, Annals of Physics **100**(1-2), 310 (1976). URL https://doi.org/10.1016/0003-4916(76)90064-6

[202] W. Israel, J.M. Stewart, Annals of Physics **118**(2), 341 (1979). URL https://doi.org/10.1016/0003-4916(79)90130-1

[203] G.S. Denicol, T. Koide, D.H. Rischke, Phys. Rev. Lett. **105**, 162501 (2010). URL https://doi.org/10.1103/PhysRevLett.105.162501

[204] R. Baier, P. Romatschke, D.T. Son, A.O. Starinets, M.A. Stephanov, Journal of High Energy Physics **2008**(04), 100 (2008). URL https://doi.org/10.1088/1126-6708/2008/04/100

[205] A. Jaiswal, Phys. Rev. C **88**, 021903 (2013). URL https://doi.org/10.1103/PhysRevC.88.021903

[206] S.M. Diles, L.A. Mamani, A.S. Miranda, V.T. Zanchin, Journal of High Energy Physics **2020**(5), 1 (2020). URL https://doi.org/10.1007/JHEP05(2020)019

[207] B.I. Abelev, M.M. Aggarwal, Z. Ahammed, B.D. Anderson, D. Arkhipkin, G.S. Averichev, Y. Bai, J. Balewski, O. Barannikova, L.S. Barnby, et al., Phys. Rev. C **79**, 034909 (2009). URL https://doi.org/10.1103/PhysRevC.79.034909

[208] L. Del Zanna, V. Chandra, G. Inghirami, V. Rolando, A. Beraudo, A. De Pace, G. Pagliara, A. Drago, F. Becattini, The European Physical Journal C **73**(8), 1 (2013). URL https://doi.org/10.1140/epjc/s10052-013-2524-5

[209] V. Rolando, G. Inghirami, A. Beraudo, L. Del Zanna, F. Becattini, V. Chandra, A. De Pace, M. Nardi, Nuclear Physics A **931**, 970 (2014). URL http://dx.doi.org/10.1016/j.nuclphysa.2014.08.011

[210] N. Hatwar, C.R. Singh, S. Ganesh, M. Mishra, Phys. Rev. C **104**, 034905 (2021). URL https://doi.org/10.1103/PhysRevC.104.034905

[211] S. Borsanyi, G. Endrődi, Z. Fodor, A. Jakovac, S.D. Katz, S. Krieg, C. Ratti, K.K. Szabo, Journal of High Energy Physics **2010**(11), 1 (2010). URL http://dx.doi.org/10.1007/JHEP11(2010)077

[212] S. Chatterjee, R.M. Godbole, S. Gupta, Phys. Rev. C **81**, 044907 (2010). URL https://doi.org/10.1103/PhysRevC.81.044907

[213] R. Baier, P. Romatschke, U.A. Wiedemann, Phys. Rev. C **73**, 064903 (2006). URL https://doi.org/10.1103/PhysRevC.73.064903

[214] M.A. York, G.D. Moore, Phys. Rev. D **79**, 054011 (2009). URL https://doi.org/10.1103/PhysRevD.79.054011

[215] M.P. Heller, R.A. Janik, Phys. Rev. D **76**, 025027 (2007). URL https://doi.org/10.1103/PhysRevD.76.025027

[216] S. Bhattacharyya, R. Loganayagam, I. Mandal, S. Minwalla, A. Sharma, Journal of High Energy Physics **2008**(12), 116 (2008). URL https://doi.org/10.1088/1126-6708/2008/12/116

[217] P.F. Kolb, U. Heinz, P. Huovinen, K.J. Eskola, K. Tuominen, Nuclear Physics A **696**(1-2), 197 (2001). URL https://doi.org/10.1016/S0375-9474(01)01114-9

[218] M.L. Miller, K. Reygers, S.J. Sanders, P. Steinberg. Glauber modeling in high-energy nuclear collisions (2007). URL https://doi.org/10.1146/annurev.nucl.57.090506.123020

[219] B. Schenke, P. Tribedy, R. Venugopalan, Physical Review Letters **108**(25), 252301 (2012). URL http://dx.doi.org/10.1103/PhysRevLett.108.252301

[220] B. Schenke, P. Tribedy, R. Venugopalan, Phys. Rev. C **86**, 034908 (2012). URL https://doi.org/10.1103/PhysRevC.86.034908

[221] L. McLerran, R. Venugopalan, Phys. Rev. D **49**, 2233 (1994). URL https://doi.org/10.1103/PhysRevD.49.2233

[222] F. Gelis, E. Iancu, J. Jalilian-Marian, R. Venugopalan, Annual Review of Nuclear and Particle Science **60**, 463 (2010). URL https://doi.org/10.1146/annurev.nucl.010909.083629

[223] C. Loizides, J. Kamin, D. d'Enterria, Phys. Rev. C **97**, 054910 (2018). URL https://doi.org/10.1103/PhysRevC.97.054910

[224] P.K. Kovtun, D.T. Son, A.O. Starinets, Phys. Rev. Lett. **94**, 111601 (2005). URL https://doi.org/10.1103/PhysRevLett.94.111601

[225] H.T. Ding, Nuclear Physics A **1005**, 121940 (2021). URL https://doi.org/10.1016/j.nuclphysa.2020.121940

[226] A. Mazeliauskas, V. Vislavicius, Phys. Rev. C **101**, 014910 (2020). URL https://doi.org/10.1103/PhysRevC.101.014910

[227] F. Cooper, G. Frye, Phys. Rev. D **10**, 186 (1974). URL https://doi.org/10.1103/PhysRevD.10.186

[228] S. Afanasiev, C. Aidala, N.N. Ajitanand, Y. Akiba, J. Alexander, A. Al-Jamel, K. Aoki, L.o. Aphecetche, Phys. Rev. C **80**, 024909 (2009). URL https://doi.org/10.1103/PhysRevC.80.024909

[229] B. Chang, D.J. Kim, J. Kral, E. Pohjoisaho, J. Rak, S. Räsänen, M. Slupecki, W. Trzaska, M. Vargyas, J. Viinikainen, et al., Journal of High Energy Physics **2015**(6) (2015). URL https://doi.org/10.1007/JHEP06(2015)190

[230] A. Kurkela, U.A. Wiedemann, B. Wu, The European Physical Journal C **79**(9), 1 (2019). URL https://doi.org/10.1140/epjc/s10052-019-7262-x

[231] S.A. Bass, M. Belkacem, M. Bleicher, M. Brandstetter, L. Bravina, C. Ernst, L. Gerland, M. Hofmann, S. Hofmann, J. Konopka, et al., Progress in Particle and Nuclear Physics **41**, 255 (1998). URL https://doi.org/10.1016/S0146-6410(98)00058-1

[232] C. Chattopadhyay, R.S. Bhalerao, J.Y. Ollitrault, S. Pal, Phys. Rev. C **97**, 034915 (2018). URL https://doi.org/10.1103/PhysRevC.97.034915

[233] B. Schenke, C. Shen, P. Tribedy, Physics Letters B **803**, 135322 (2020). URL https://doi.org/10.1016/j.physletb.2020.135322

[234] B. Schenke, S. Schlichting, Phys. Rev. C **94**, 044907 (2016). URL https://doi.org/10.1103/PhysRevC.94.044907

[235] S. Ryu, J.F. Paquet, C. Shen, G. Denicol, B. Schenke, S. Jeon, C. Gale, Physical review letters **115**(13), 132301 (2015). URL https://doi.org/10.1103/PhysRevLett.115.132301

[236] L. Du, U. Heinz, Computer Physics Communications **251**, 107090 (2020). URL https://doi.org/10.1016/j.cpc.2019.107090

[237] C. Plumberg, D. Almaalol, T. Dore, J. Noronha, J. Noronha-Hostler, Phys. Rev. C **105**,

L061901 (2022). URL https://doi.org/10.1103/PhysRevC.105.L061901

[238] A. Kurkela, A. Mazeliauskas, J.F.m.c. Paquet, S. Schlichting, D. Teaney, Phys. Rev. C **99**, 034910 (2019). URL https://doi.org/10.1103/PhysRevC.99.034910

[239] N. Brambilla, M.A. Escobedo, J. Soto, A. Vairo, Phys. Rev. D **96**, 034021 (2017). URL https://doi.org/10.1103/PhysRevD.96.034021

[240] C.R. Singh, P.K. Srivastava, S. Ganesh, M. Mishra, Physical Review C **92**(3), 034916 (2015). URL https://doi.org/10.1103/PhysRevC.92.034916

[241] Nuclear Modification Factor of prompt D^0 in PbPb Collisions at $\sqrt{s_{\mathrm{NN}}} = 2.76$ TeV (2015). URL https://cds.cern.ch/record/2055466?ln=en

[242] J. Adam, D. Adamová, M.M. Aggarwal, G. Aglieri Rinella, M. Agnello, A. Agostinelli, N. Agrawal, et al., Phys. Rev. C **91**, 064905 (2015). URL https://doi.org/10.1103/PhysRevC.91.064905

[243] G. Aad, B. Abbott, J. Abdallah, S. Abdel Khalek, O. Abdinov, R. Aben, B. Abi, M. Abolins, O.S. AbouZeid, H. Abramowicz, H. Abreu, R. Abreu, Y. Abulaiti, B.S. Acharya, et al., Phys. Rev. Lett. **114**, 072302 (2015). URL https://doi.org/10.1103/PhysRevLett.114.072302

[244] V. Khachatryan, A.M. Sirunyan, A. Tumasyan, W. Adam, E. Asilar, T. Bergauer, J. Brandstetter, E. Brondolin, M. Dragicevic, et al., J. High Energy Phys. **2017**(4), 1 (2017). URL https://doi.org/10.1007/JHEP04(2017)039

[245] R. Vogt, Phys. Rev. C **81**, 044903 (2010). URL https://doi.org/10.1103/PhysRevC.81.044903

[246] M. Tanabashi, K. Hagiwara, K. Hikasa, K. Nakamura, Y. Sumino, F. Takahashi, J. Tanaka, K. Agashe, G. Aielli, C. Amsler, M. Antonelli, D.M. Asner, H. Baer, S. Banerjee, R.M. Barnett, T. Basaglia, C.W. Bauer, et al., Phys. Rev. D **98**, 030001 (2018). URL https://doi.org/10.1103/PhysRevD.98.030001

List of Publications

List of Publications:

- **Nikhil Hatwar**, M. Mishra, Using the nonhydrodynamic mode to study the onset of hydrodynamic behavior in ultraperipheral symmetric nuclear collisions, Phys. Rev. C **106**, 054902 (2022) https://doi.org/10.1103/PhysRevC.106.054902
- **Nikhil Hatwar**, Captain R. Singh, S. Ganesh, and M. Mishra, Bottomonium suppression in PbPb collisions at energies available at the CERN Large Hadron Collider, Phys. Rev. C **104**, 034905 (2021) , https://doi.org/10.1103/PhysRevC.104.034905

Conference proceedings:

- Singh C.R., **Hatwar N.**, Mishra M., "Open Heavy Flavor Production in Hot QCD Matter at CERN LHC", XXIII DAE High Energy Physics Symposium. Springer Proceedings in Physics, vol 261. Springer, Singapore (2021), https://doi.org/10.1007/978-981-33-4408-2˙149

- **Nikhil Hatwar**, M. Mishra, "Bottomonium Suppression and elliptic flow of pions in PbPb collisions at CERN LHC energies", Proceeding for XXIII DAE High Energy Physics Symposium, IISER-Mohali, Chandigarh, India, 12-16 Dec 2022.
  (manuscript under preparation)
- **Nikhil Hatwar**, M. Mishra, "Probing the onset of hydrodynamic behaviour in peripheral heavy-ion collisions", Proceeding for International Conference on Physics and Astrophysics of Quark Gluon Plasma (ICPAQGP-2023), Puri, Odisha, 7-10 Feb 2023.
  (manuscript under preparation)

List of conferences / workshop participated:

- International Conference on Physics and Astrophysics of Quark Gluon Plasma, Puri, Odisha, India, 6-10 Feb **2023**.
- DAE-BRNS High Energy Physics Symposium, IISER-Mohali, Chandigarh, India, 12-16 Dec **2022**.
- 8th International Workshop on Heavy Flavour Production in Nuclear Collisions (attended online), Torino, Italy, 14-16 July **2022**.
- 20th International Conference on Strangeness in Quark Matter (attended online), Busan, South Korea, 13-17 June **2022**.
- Symposium on ”Contemporary and Emerging Topics in High Energy Nuclear Physics”, Variable Energy Cyclotron Centre, Kolkata, India, 25-27 Nov **2019**.
- Workshop on “The myriad Colourful ways of understanding extreme QCD matter”, International Centre for Theoretical Sciences (ICTS) of the Tata Institute of Fundamental Research, Bangalore, India, 1-17 Apr **2019**.
- DAE-BRNS High Energy Physics Symposium, Indian Institute of Technology-Madras, Chennai, India, Dec **2018**.

Brief Biography of the Supervisor

Dr. Madhukar Mishra completed his Ph.D. in 2008 from Banaras Hindu University, Varanasi. He was appointed as an assistant professor at Birla Institute of Technology and Science, Pilani campus, Rajasthan, India in 2009. The broad area of his research is High Energy Physics phenomenology. His primary interest is finding the properties of a state of quark matter at extreme pressure and/or temperature situations governed by quantum chromodynamics called Quark-Gluon Plasma. Sufficiently high temperatures are produced in heavy-ion collisions where such a state of matter could form. The quest is to find the effective description of Quark-Gluon Plasma in high energy collisions through various experimental observables, which would hold across different system and energies of collision. Dr. Madhukar Mishra has carried out studies on theoretical models describing signatures of Quark-Gluon Plasma and his work has been published and referred in several national and international journals. He has delivered talks based on his work in numerous conferences and institutions. He is now exploring possibilities in Beyond Standard Model through axions physics in the contexts of CP violation and its origin from neutron stars as well as axions in condensed matter physics.

Brief Biography of the Student

I graduated with Bachelor of Engineering in Electronics and Telecommunication from G.H Raisoni College of Engineering, Nagpur, India in 2013. My final year project was about improving the performance of an electric bike using a combination of battery and supercapacitors. In 2016, I completed my Master's in Physics with a specialization in Astronomy and Astrophysics from the Department of Physics, Savitribai Phule Pune University, India. For my master's thesis, I studied *fractal nature of quantum mechanical paths* under Prof. Anil Gangal, IISER, Pune, India. I joined the Physics Department, Birla Institute of Technology and Science, Pilani Campus for a DST project and registered for Ph.D. in August 2017. I am interested in finding the dynamics of QGP and isolating and quantifying the non-QGP signatures from QGP signatures in small systems. Apart from this, I am keen to explore problems in astrophysics and cosmology.